ISSN 1580-2949
UDK 669+666+678+53 MTAEC9, 43(6)275–342(2009)

MATER. TEHNOL.	LETNIK VOLUME 43	ŠTEV. NO. 6	STR. P. 275–342	LJUBLJANA SLOVENIJA	NOV.–DEC. 2009

VSEBINA – CONTENTS

UDK 669.1:621.438:620.18
Pregledni članek/Review article

ISSN 1580-2949
MTAEC9, 43(6)277(2009)

OPERATION MIKROSTRUCTURE AND LIFETIME OF GAS TURBINE ENGINE (GTE) COMPONENTS

DELOVNA MIKROSTRUKTURA IN TRAJNOSTNA DOBA SESTAVNIH DELOV PLINSKIH TURBIN (GTE)

Leonid B. Getsov[1], G. P. Okatova[2], A. I. Rybnikov[3], D. G. Fedorchenko[4]

[1]State Polytechnic University, SPb; Zakevskii pr. 43 appt. 89, 195213 Russia, St. Petersburg
[2]Byelorussian Scientific & Research Institute of Powder Metallurgy
[3]NPO CKTI
[4]Energomash Corporation
guetsov@yahoo.com

Prejem rokopisa – received: 2008-11-15; sprejem za objavo – accepted for publication: 2009-06-04

Changes of microstructure and mechanical properties of stels and alloys and protection coatings decreasing the serviceability of components after long time use in gas turbine engines are described. Different examples of damage on turbine blades are shown. Methods for the evaluation of residual life of components are suggested. For a large series of metals and alloys, the high temperature properties after annealing up to 40 000 in temperature range 550 °C to 900 °C and are given, also.

Key words: gas turbine components, steels and alloys, changes of microstructure and properties, method of evaluation of serviceability

Opisane so spremembe mikrostrukture in mehanskih lastnosti jekel in zlitin ter varovalnih prevlek, ki zmanjšajo trajnostno dobo sestavnih delov plinskih turbin. Prikazani so različni primeri poškodb lopatic teh turbin. Predlagane so metode za oceno preostale trajnostne dobe sestavnih delov. Za precejšnje število jekel in zlitin so navedene mehanske lastnosti pri visokih temperaturah do 40 000 h žarjenja v razponu temperatur med 550 °C in 900 °C.

Ključne besede: sestavni deli plinskih turbin, jekla in zlitine, sprememba mikrostrukture in lastnosti, metode za oceno preostale trajnostne dobe

1 INTRODUCTION

For the manufacture of components for gas turbines a great variety of special steels and alloys are used because of the continuously increasing operating temperature. This led to the situation of components and materials in use in various GT units with serviceability not suited sufficiently for the operating temperature and time. Therefore, the acquisition of data on the microstructural state of GTE components from such materials may indicate to operationl damages and highlight the potential of the prolongation of their lifetime.

2 MATERIAL MICROSTRUCTURE AND CONTINUOUS OPERATION BEHAVIOR

The serviceability features related to the operating times at elevated temperatures include [1]:

1. Needle-like topological close-packed phases (σ and μ) appearing in the Ni-based high-temperature alloys microstructures may degrade the ductility and long-term strength causing possibly, also, non expected changes of high-temperature strength and low-cycle fatigue resistance.

2. A des-alloyed layer formed at the surface of high-temperature alloys may lower the long-term strength, low-cycle fatigue and thermal fatigue resistance, while the change of composition and thickness of the coating layer due to the diffusion redistribution of elements with the parent metals may degrade significantly the protective capability of the coating.

3. The decrease of grain size in austenitic steels and Ni-alloys indicates to the progressing of recrystallization, while, grain size coarsening indicates to a significant increase of temperature.

4. Creep pores along the grain boundaries testify for a considerable material degradation, particularly the lowering of ductility.

5. The decrease of the share of γ'–phase and it coarsening at continuous operation is sign of softening of Ni-based high-temperature alloys caused by high temperatures. The increase of the share of finely dispersed γ'-phase indidates either to a long-time exposure of the alloy to low temperatures that may cause embrittlement, or to a considerable overheating with γ'-phase dissolution and precipitation at cooling as fine dispersion (**Figure 1**).

6. With increased presence of a second-phase at grain boundaries, the alloy ductility is diminished.

7. The recrystallization at the surface of single-crystal blades, irrespective of its reason (manufacture, operation, coating application), degrades the long-term strength and thermal fatigue resistance of blades.

A careful metallographic examination may discover microcracks of different origin appeared in the manu-

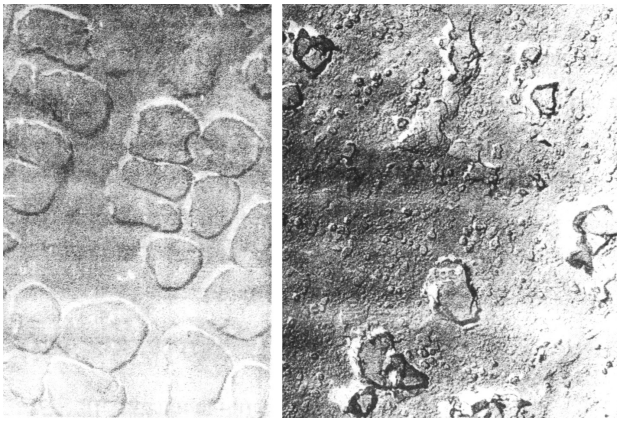

Figure1: Microstructure of a blade overheated in operation
Slika 1: Mikrostruktura lopatice, ki je bila pregreta pri uporabi

facturing of the alloy, the manufacturing of components, GTE testing and GTE operation. Micro-cracks impair the alloy properties, affect its serviceability and can, in certain conditions, grow in size at static and at low-cycle stressing creep and at vibratory stressing.

3 EFFECT OF CONTINUOUS OPERATION ON MATERIAL PROPERTIES

Long-term exposure of a material to elevated temperatures can significantly affect its serviceability. Relationships have been proposed that connect the mechanical properties with the operating conditions[5]. Extending the concept of the creep equation with Rabotnov's structural parameters s_i.

$$p^{\bullet} = F(s_1(\tau,T),\ s_2(\tau,T),\ s_3(\tau,T),\ .....\ T,\sigma) \qquad (1)$$

to other material properties the relationships have been proposed:

$$\sigma_B = F(s_1(\tau,T),\ s_2(\tau,T),\ s_3(\tau,T),\ ....T,v) \qquad (2)$$

$$\sigma_{0,2} = F(s_1(\tau,T),\ s_2(\tau,T),\ s_3(\tau,T),\ ....T,\ v) \qquad (3)$$

$$\sigma_{lts.} = F(s_1(\tau,T),\ s_2(\tau,T),\ s_3(\tau,T),\ ...\ T,t) \qquad (4)$$

$$\delta = F(s_1(\tau,T),\ s_2(\tau,T),\ s_3(\tau,T),\ ...\ T,v) \qquad (5)$$

$$\Delta\varepsilon = F(s_1(\tau,T),\ s_2(\tau,T),\ s_3(\tau,T),\ ...\ T_{max},\ T_{min},\ N,\ \tau_c) \qquad (6)$$

$$S_{0,4} = F(s_1(\tau,T),\ s_2(\tau,T),\ s_3(\tau,T),\ ...\ T,v) \qquad (7)$$

$$dl/d\tau = F(s_1(\tau,T),\ s_2(\tau,T),\ s_3(\tau,T),\ ...\ T,K_1) \qquad (8)$$

With: v – deformation rate, τ_c, T_{max}, T_{min}, N – respectively, cycle period, maximal and minimal cycle temperature, number of cycles to the initiation of thermal fatigue cracks for thermal cyclic loading, K_1 – stress intensity factor. Note that, unlike[1] this article is aimed to define the criteria characterizing the microstructural state, thus, to impart a physical meaning to the microstructural parameters $\boldsymbol{s_1(\tau,T)}$, $\boldsymbol{s_2(\tau,T)}$, $\boldsymbol{s_3(\tau,\ T)}$, ...

To estimate the stress-strain state and safety margins for the components of a definite alloy allowing for changes of microstructure, it is necessary to know the kinetics of change of yield strength $\sigma_{0,2}$, elongation δ, creep rate $\boldsymbol{p^{\bullet}}$, creep cracks growth rate $\mathbf{dl/d}\tau$, cyclic deformation strength $\boldsymbol{S_{0,4}}$, thermal fatigue $\Delta\varepsilon$ and long-term strength σ_{lts}. after long time high temperature exposure of the component.

Tables 1–5 show the mechanical properties and long-term strength tested on a number of steels and alloys applied in GT units in continuous operation[5].

It is possible to derive digitally a discrete form for the equations (2) to (8) applying the data given in the tables.

4 CONCEPT OF LIFETIME PROLONGATION FOR GTE COMPONENTS

To estimate the quality of the microstructure of components after long time operation, which is the basis of a reliable prediction fof lifetime prolongation, different methods may be applied[2,3,4], metallographic examination with the replication method, X-ray inspection

Table 1: Effect of long time exposure on mechanical properties of steels and alloys
Tabela 1: Vpliv dolgotrajnega zadržanja na mehanske lastnosti jekel in zlitin

Material	Anneling Conditions		Test Conditions		Time to Fracture, t_f/h	Elongation
	T/°C	Time, t/h	T_t/°C	σ/MPa		δ/%
EI481 (37Х12Н7Г8МФБ)	650	0	650	270	1000	4.14
		40000			72	30
EP126 (ХН28ВМАБ)	800	0	900	50	242	18
		5000			65	45
EI787 (ХН35ВТЮ)	650	0	650	380*	1350	-
		10000			148	-
		0	650	350	8000	1,6
		50000			442	15
EP99 (ХН50МВКТЮР)	800	0	800	200	374	24
		5000			193	20.4
EP126 (ХН28ВМАБ)	800	0	800	100	684	28.8
		5000			151	10
	800	0	900	50	242	18
		5000			65	45

Table 2: Effect of long time exposure on mechanical properties of Ni-based steels and alloys
Tabela 2: Vpliv dolgotrajnega zadržanja na mehanske lastnosti nikljevih jekel in zlitin

Alloy	Aging Temperature, T_a/°C	Aging Time, t_a/h	Test Temperature, T_t/°C	$\sigma_{0,2}$/ Mpa	σ_b/MPa	δ/%	Ψ/%
EP99	Initial		20	815	1170	50.2	–
	750	5000		610	900	57	–
	800	2000		982	1040	0.5	–
		5000		848	1230	5.0	–
	900	2000		858	990	1.0	–
		10000		502	765	4.7	–
GS6U	Initial	–		760–850	770–900	5.9–27.8	12–28
	800	2000		880	1030	1.2	–
		5000		853	862	12.7	–
	850	2000		710–900	880–910	1.5	7.0
		5000		820	1040	5.9	5.9
	900	2000		678	832	11.1	12.6
EP220	Initial	–	800	771	1008	6.5	10.8
	800	16000		816	892	1?9	6,5
EI929 (XH55BMTKIO)	550	10000	20	777	1170	18	18
	600	10000		780	1160	15	17
	650	10000		810	1130	11.5	11.5
	700	10000		750	1200	17	16
	750	10000		690	1220	23	22
	800	10000		630	1030	15	15
EI893Л	Initial	–		513	734	23.5	22
	700	5000		578	817	13.1	18,2
	750	5000		470	757	16.2	22.7
	800	5000		442	706	16.1	19.1
EP126	Initial	–		468	890	41	–
	750	10000		479	819	3.9	–
	800	10000		446	872	14.2	–
	900	10000		364	814	24.4	–
EI703 (XH38T)	Initial	–		460	808	40.3	–
	750	10000		338	713	19.8	–
	800	10000		313	709	30.2	–
	900	5000		165	550	44	
CNK–7 RS	700	3000	20	864–975	880–1007	0.8–3.9	0.7–7.5
			700	847	1082	7	14.4
	750	3000	20	838	888	1.7	7.9
			750	793–826	931–1021	3.2–5.0	6.2–10
	800	3000	20	718–753	791–867	1.9–4.5	6.2–12.9
			800	690–753	796–862	6.1–10.8	9.7–24.9
	850	3000	20	672–772	779–833	2.3–5.1	2.2–12
			850	584–650	690–760	3.1–13.1	8.4–24.9
ZMI–3	650	5000	20	845–877	909–944	1.8–1.5	8.1
			650	817	976	3.7	
	700	3000	20	842–917	934–972	1.8–4.1	3.6–4.0
			700	891–905	1050	4.0–6.4	4.0–8.2
	750	3000	20	807	874	2.0	4.9
			750	745	947	12.4	18.7
	800	3000	20	701–848	764–948	1.4–5.0	2.7–7.0
			800	649–848	745–948	4.0–12.0	6.2–19.7
	850	3000	20	617–772	724–859	2.9–4.0	4.6–5.0
			850	460–690	626–820	3.7–13.6	5.2–22.0
GS6K	600	10000	20	1000–1100	1070	2.1	4.6–5.6
			600	1000	1080	2.2	5.6
	650	10000	20	1040	1080	2.9	4.3–5.3
			650	990	1060	1.6	3.0
	700	10000	20	1000	1020	1.5–1.7	1.4–1.6
			700	1000	1060	0.8	0.9
	800	10000	20	830	950	1.6	2.0
			800	820	950	2.2	4.3
	850	10000	20	730–780	920–890	2.5–3.5	5.0–5.6
			850	710	810	1.7	2,1
	900	10000	20	680	840–890	3.0–4,3	5.5–6.5
			900	620	670	2.2	2,0
	950	10000	20	630	800–870	3.0–3.5	4.5–8.2
			950	500	560	5.4	7.5
	1000	1000	20	740	860–900	2.3–2.5	2.8–4.8
EI481	Initial	–	20	733–806	1054–1068	17.8–23.7	24.5–43.2
			650	497–506	599–614	14.3–14.7	45.0
	550	10000	20	772–792	103–106	18.4–22.2	28.4–40.7
			650	557–595	620–658	9–10	35.2–35.5
	600	10000	20	613–622	964–955	20.6–24.2	28.9–29.9
			650	422–437	540	15.0–15.5	41–43.2
	650	10000	20	415	813	24.8	29.2
			650	328	453	18.5	39.5

Table 3: Effect of long time exposure on plasto-elastic deformation strength for pearlitic and martensitic steels ($\sigma_{0.2\ aged}/\sigma_{0,2init}$) at 20 °C
Tabela 3: Vpliv dolgotrajnega zadržanja na plasto-elastično deformacijsko trdnost perlitnih in martenzitnih jekel ($\sigma_{0.2\ aged}/\sigma_{0,2init}$) pri 20 °C

Aging Temperature, T_a/°C	Aging Time, t_a/h	15ХМФ	EI802 (15Х12ВНМФ)	EP752	EP291	15Х11МФ	20Х13
500	40000	0.88					
550	5000		0.92				
550	10000						0.86
600	5000		0.89		0.92		
600	10000					0.78	0.75
600	30000	0.78					
620	2500			0.84			
650	2500			0.78			
650	5000				0.86		
650	10000				0.82		

Table 4: Effect of long time exposure on plastoe-elastic deformation strength for austenitic steels ($\sigma_{0.2\ aged}/\sigma_{0,2init}$) at 20 °C
Tabela 4: Vpliv dolgotrajnega zadržanja na plasto-elastično deformacijsko trdnost avstenitnih jekel ($\sigma_{0.2\ aged}/\sigma_{0,2init}$) pri 20 °C

Aging Temperature, T_a/°C	Aging Time, t_a/h	20Х23Н18	EI572	EI481	EI787	EI703
600	5000		1	1	1,2	
650	10000	1.13	-	0.83	0.94	
	20000		1	0.87		
	30000				0.91	
700	5000		0.79	0.7		
	10000	1.1				
750	5000	1	0.75			0.8

Table 5: Effect of long time exposure on plasto-elastic deformation strength for Ni-based alloys ($\sigma_{0.2\ aged}/\sigma_{0,2init}$) at 20 °C.
Tabela 5: Vpliv dolgotrajnega zadržanja na plasto-elastično deformacijsko trdnost nikljevih zlitin ($\sigma_{0.2\ aged}/\sigma_{0,2init}$) pri 20 °C

Aging Temp., T_a/°C	Aging Time, t_a/h	EI868	EP99	EP220	EI607	VG85	EI867	EI437B
700	10000				0.69		0.89	
750	500	1	-	-	-	-	-	1.36
	1000	1	-	-	-	1.03	-	-
	5000	0.9	-	-	-	1.07	-	-
	10000	0.83	-	-	-	-	-	-
800	2000	0.9	1.2	0.9	-	1.03	-	-
	5000	0.87	1.04	0.83	-	0.95	-	-
	16000	0.77	-	0.9	-	-	-	—
900	1000	0.75	-	-	-	1	0.82	-
	2000	0.78	1.05	0.93		0.82		
	5000	0.78	-	0.85	-	0.59	-	-
	10000	0.68	0.62	-	-	-	-	-

with phase analysis, X-ray spectral micro-analysis, etc. and appying interrelation of microstructure and properties. The quality criteria for microstructure and it distribution all over the component body should be established up for each material considering the stressing and stress distribution of the GTE component considered.

Based on the all-inclusive study of the interrelation between residual endurance and some microstructural features emerging in the metal as result of its damage, the blades of engines run at different operating and climatic conditions[1,6,7,8,9] can be examined and the effect of operating rate on damage rate increase estimated. The base for decision is the comparison with the initial microstructure. For the indirect evaluation of the quality of the surface layer, it is advisable to measure its hardness and micro-hardness.

With turbine blades as example, in the scheme of the methodology for predicting the residual capacity of GTE high-temperature components after long time operation is shown in **Figure 2**.

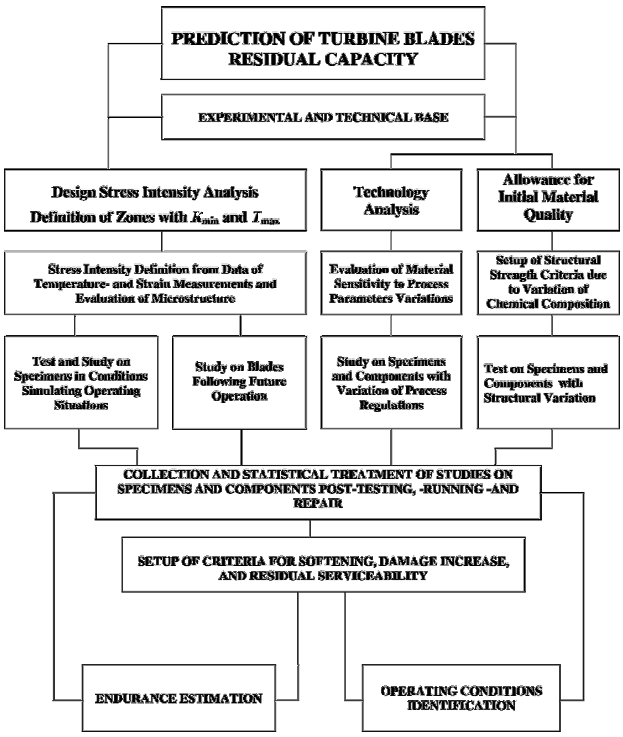

Figure2: Methodology for predicting the residual capacity of turbine blades (K_{min} is the minimal safety margin value all over the blade)

Slika 2: Metodologija za napovedovanje rezidualne uporabnosti turbinskih lopatic (K_{min} je vrednost minimalnega varnostnega razpona na celi lopatici)

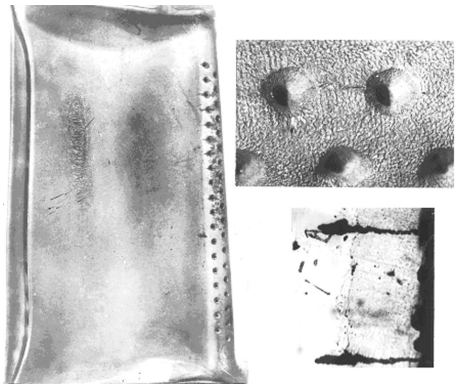

Figure3: Appearance of burning-out thermal fatigue cracks in the basic material of the edge of a turbine blade of ŽS6 alloy with NiCrAlY coating

Slika 3: Videz odžganih termičnih razpok v materialu roba lopatice iz zlitine ŽS6 s pokrivno plastjo NiCrAlY

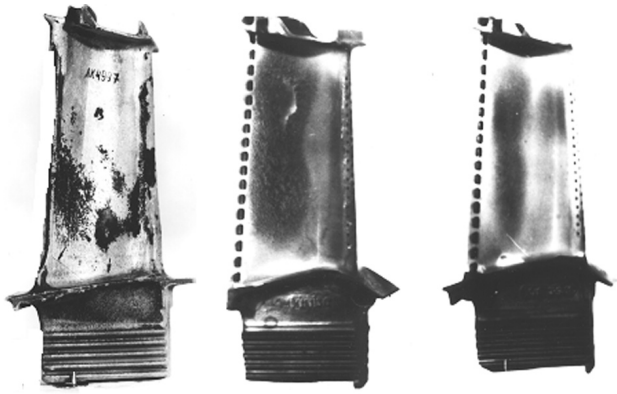

Figure 4: Turbine blades without (a) and with a thermal-barrier ceramic coating (b, c) after comparison tests in an impeller of an aircraft gas-turbine engine: b – view of the blade before carbon deposit removal, c – view of the blade after carbon deposit removal

Slika 4: Turbinske lopatice brez (a) keramične pokrivne plasti in z njo (b, c) po primerjalnih preizkusih v impellerju letalske plinske turbine; b- videz lopatice pred odstranitvijo depozita ogljika, c – vodez lopatice po odstranitvi depozita ogljika

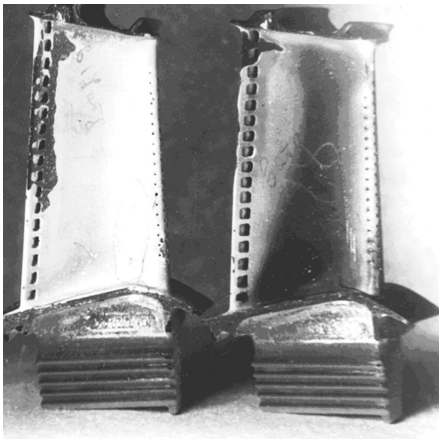

Figure 5: Peeling of the ceramic layer of the thermal protection coating of a turbine blade after the expiration of its operating time in the engine

Slika 5: Luščenje varovalne keramične prevleke po preteku dobe uporabnosti v motorju

5 COATING QUALITY CRITERIA

The reliability of the prediction of the residual service life of coated parts depends largely on the state of the coating[1,10]. After long time the coating quality use depends on its type: diffusion, condensation, metallic, metallic with an outer ceramic layer. As a rule, the quality of the coating after use is evaluated in comparison with its initial quality. In this case, the quality criteria for diffusion and metal condensation coatings after long use are: layer thickness uniformity, absence of chipping and coating layer peeling, absence of cracks, especially thermal fatigue cracks (**Figure 3**), of significant surface oxidation (**Figure 4**) and pit-type corrosion damage, absence of significant redistribution of the basic alloying elements of the coating (Al, Cr) and significant changes in phase composition of the coating.

The impoverishment of a diffusion coating with aluminum and chrome reduces sharply it protective properties and, as with pits formation, leads to the decrease of service life. The methods of calculated prediction of the diffusion redistribution of coating elements were examined in[1]. As criterion of service-ability of diffusion coatings the decrease of surface concentration of the element determining the protection against corrosion by up to one third of the difference between the initial concentration in the coating and in

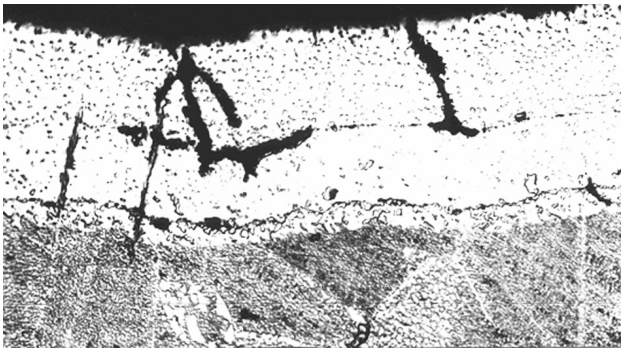

Figure 6: Cracks in and below the ceramic layer. Cracking and peeling of the ceramic layer of the blade in the process of operation
Slika 6: Razpoke v in keramični prevleki in pod njo. Razpokanje in luščenje keramične prevleke med uporabo

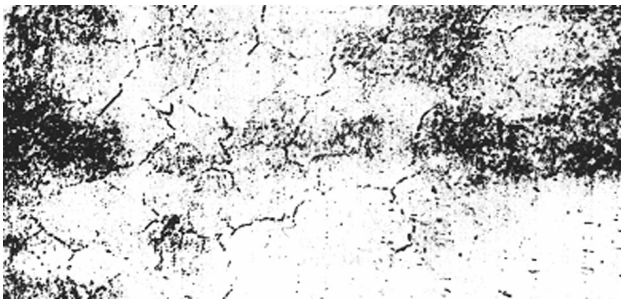

Figure 7: Fragmentation of the thermal protection ceramic coating
Slika 7: Fragmentacija keramične varovalne plasti

the basic metal can be used. Coating corrosion damage with depth up to 2/3 of the layer thickness can be used as second criterion.

For ceramic coating layers, the criteria of quality are: porosity (density), uniformity of layer thickness, thickness of the interlayer Al_2O_3 on the side of the metallic layer and, most importantly, the presence of chipping, cracking and peeling (**Figures 5 and 6**). On the contrary, the fragmentation of the thermal protection coating layer (**Figure 7**) increases the resistance to cracking and peeling and is not a defect.

6 CONCLUSION

The investigations of changes of microstructure and mechanical characteristics of materials and coatings after long use enable to solve, on scientifical base, questions connected with the possibility of increasing the service life of parts. Knowing the dependence of properties and microstructure of materials, it is possible to evaluate the change of initial properties with examination of the microstructure and predict the residual service life. The data for a number of materials cited in this report can serve as the basis for such predictions.

7 REFERENCES

[1] Getsov L. B. Materials and strength of gas turbine parts. M: Nedra, 1996, 590 p

[2] Artamonov V. V., Artamonov V. P. Improvement of metal prediction methods for heat-power engineering equipment. Energetika (**2000**) 7, 34–39

[3] Express control method for metal microstructure of power equipment (method of replicas). Report of the Scientific and Production Association attached to the Central Boiler-and-Turbine Research Institute (NPO TsKTI), 1987

[4] V. P. Goltsev, T. T. Dedekaev, A. M. Dergay, A. I. Rybnikov, A. I. Rytvinski. X-ray spectral and electron-microscopic methods of examining the structure and properties of materials/ Minsk. Nauka I Tekhnika. 1980, 190 p

[5] Getsov L. B., Rybnikov A. I., Pigrova G. D. Changes in the structure and properties of steels and alloys during long operation at high temperature. /EUROMECH-MECAMAT 98, 3rd European Mechanics of Materials Conference on mechanics and multi-physics processes in solids: experiment, modeling, applications, Oxford-U. K., 23–25 November, 1998, Ed. E.Busso, G.Cailletaud, Pr.9-105-115

[6] Zakharova T. P., Pimenova G. P. Calculated experimental determination of the residual durability of turbine blades. Intercollegiate Collection of Articles "Vibration Strength and Reliability of Engines and Aircraft Systems", Issue 8, Kuibyshev, 1981, 47–57

[7] Gordeyeva T. A., Gerchikova N. S., Kozlova M. N., Samoilov A. I. et al. Methods of investigating the state of the materials of gas-turbine rocket engine parts and its change during operation. Instruction № 1050-75. M., All-Russian Research Institute for Aircraft Materials (VIAM), 1975, 39 p

[8] Pimenova G. P. Investigation of blades made of ZhS6KP alloy and ways of extending their service life. Thesis for a Scientific Degree (Candidate of Engineering Science) Kazan, 1973

[9] Pimenova G. P. Metallurgical criteria of serviceability and substantiation of the service life of turbine blades of engines in NK series. Theses of the Scientific and Technical Conference "High-Temperature Deformable Alloys for Gas-Turbine Engines". M., VIAM, 1977

[10] Pimenova G. P. Investigation of the calorized layer and damageability of the turbine blades of NK engines. Theses of Reports at the 5th All-Union Conference "Structural Strength of Engines", Kuibyshev, 1978

UDK 622.362:519.2
Original scientific article/Izvirni znanstveni članek

ISSN 1580-2949
MTAEC9, 43(6)283(2009)

MODELING OF THE PIEZOELECTRIC EFFECT USING THE FINITE-ELEMENT METHOD (FEM)

MODELIRANJE PIEZOELEKTRIČNIH POJAVOV Z METODO KONČNIH ELEMENTOV

Sefer Avdiaj[1], Janez Šetina[2], Naim Syla[3]

[1]Lotrić, d.o.o. Selca 163, 4227 Selca, Slovenia
[2]Institute of Metals and Technology, Lepi pot 11, 1000 Ljubljana, Slovenia
[3]University of Prishtina, Faculty of Natural Science and Mathematics, Mother Teresa av. 3, 10000, Prishtina, Kosovo
sefer.avdiaj@imt.si

Prejem rokopisa – received: 2009-06-08; sprejem za objavo – accepted for publication: 2009-07-16

Some solid, crystalline materials exhibit the piezoelectric effect, which is very interesting for a variety of technological applications. Piezoelectric materials are widely used in electromechanical sensors and actuators, such as robotics' sensors, actuators, ultrasonic transducers for medical imaging and non-destructive testing. The paper presents the modeling of the piezoelectric effect in quartz, which is the most widely used material. The basic ideas of the finite-element method (FEM) for solving the problem of piezoelectric media are presented. All the results are based on linear piezoelectricity, in which the elastic, piezoelectric, and dielectric coefficients are treated as constants, independent of the magnitude and frequency of the applied mechanical stresses and electric fields. Starting with the tri-dimensional finite-element method, we have developed a numerical computational method for a determination of the electrical voltage (the direct piezoelectric effect) and the eigenmodes of vibration (the inverse piezoelectric effect).

The finite-element method is normally used for solving problems related to macrostructures. The aim of this work is to show that the finite-element method (FEM) is also a useful and convenient method for solving problems in relation to microstructures. Here we present the solution to the problem of the piezoelectric effect using the FEM, approaching the problem from the microstructural point of view.

Key-words: Finite-Element Method, Piezoelectricity, Modeling, Ansys, Quartz, Voltage, Eigenfrequencies

Nekatere kristalinične trdne snovi izkazujejo piezoelektrični pojav, kar je zelo zanimivo za številne tehnološke aplikacije. Piezoelektrični materiali se večinoma rabijo za elektromehanske senzorje in aktuatorje, na primer v robotiki, za ultrazvočne pretvornike pri raznih slikanjih v medicini in neporušnih preskušanjih. V prispevku obravnavamo modeliranje piezoelektričnega pojava v kremenu, ki se najpogosteje uporablja v piezoelektričnih napravah. Predstavljene so osnove metode končnih elementov (MKE) za numerično reševanje problemov piezoelektričnih struktur. Vsi prikazani rezultati so bili dobljeni za primer linearnega piezoelektričnega pojava, kjer smo obravnavali elastične, piezoelektrične in dielektrične koeficiente kot konstante, neodvisne od velikosti in frekvence mehanskih napetosti in električnih polj. Za obravnavo praktičnih primerov smo MKE aplicirali v treh dimenzijah in razvili numerične računske postopke za določitev električne napetosti v odvisnosti od mehanskih napetosti (neposredni piezoelektrični pojav) ter določitev lastnih nihajnih načinov in frekvenc v primeru inverznega piezoelektričnega pojava.

Ključne besede: metoda končnih elementov, piezoelektrični pojav, modeliranje, Ansys, kremen, lastne frekvence

1 INTRODUCTION

The Curie brothers, Jacques and Pierre, were two of the first people to experiment with common crystals such as quartz, topaz and sugar cane in the field of piezoelectricity in 1880 to 1882. The next 25 years (1882–1917) brought a substantial amount of information to be supported by mathematical calculations. Woldermar Voigt published a book that dealt with the physics of crystals, and research work was done in support of the book in reference to the effects of piezoelectricity such as, the changing of electrical into mechanical energy and vice versa. These French workers, along with P. Langevin, put together a submarine detector made of steel sheets and quartz.

In this paper we treat the piezoelectric effect in quartz in a theoretical way; in Section 2 we treat a mathematical formalization that describes the piezoelectric effect; and in Section 3 we present the modeling of the piezoelectric effect with the FEM.

The equations of piezoelectricity are sufficiently complex to preclude a closed form solution for all but the simplest cases. This is unfortunate since the piezoelectric effect plays an important role in the field of crystal physics and transducer technology (sensors and actuators). Previously, in the past 70 years, variational principles have been derived that serve as the basis of approximate solution techniques, such as the powerful Rayleight-Ritz method. Noteworthy contributions along these lines were made in the papers of Henno Allik and Thomas J. R. Hughes.[1,2,4,8,16]

Although these important developments have opened the way to wider class problems, they are not sufficiently general in themselves to be considered a universal method of piezoelectric analysis. For instance, a significant deficiency of the Rayleigh-Ritz technique is the necessity to select a trial function, which often becomes intractable for complex geometries.

This paper concerns the development of a general method of electrostatic analysis by incorporating the

piezoelectric effect in a finite-element method (FEM). The theory presented is, essentially, an expansion of the variational principle, which was used before by Holland and EerNisse[1], presented here in a matrix fashion. The dynamical matrix derived for linear piezoelectricity is found to be reducible, in form, to the ordinary matrix equation encountered in structural dynamics.

The electrostatic matrices for a simplex 'displacement-potential' for three-dimensional analysis are presented, thereby illustrating the method.[1,2,3,8,16].

The FEM is normally used for solving problems related to macrostructures. The aim of this work is to show that the FEM is also a useful and convenient method for solving problems in relation to microstructures. Here we present the solution of the problem of the piezoelectric effect using the FEM, approaching the problem from the microstructural point of view.

2 FINITE ELEMENT APPROACH

The study of physical systems frequently results in partial differential equations, which either cannot be solved analytically or lack an exact analytic solution due to the complexity of the boundary condition or domain. For a realistic and detailed study, a numerical method must be used to solve the problem. The finite-element method is often found to be the most appropriate.

The FEM has successfully penetrated many areas, such as heat transfer, fluid mechanics, electromagnetism, acoustics and fracture mechanics. Basically, the finite element method consists of a piecewise application of classical variational methods to smaller and simpler sub-domains called finite elements connected to each other at a finite number of points called nodes.[6,15]

The fundamental principles of the finite-element method are:

- The continuum is divided into a finite number of elements of a geometrically simple shape.
- These elements are connected in a finite number of nodes.
- The unknowns are the displacements of these nodes.
- Polynomial interpolation functions are chosen to prescribe the unknown displacement field at each point of the element related to the corresponding field values at the nodes.
- The forces applied to the structure are replaced by an equivalent system of forces applied to the nodes.[2]

A finite-element formulation accounting for the coupling between the equations of electrostatics and elastodynamics becomes necessary when the piezoelectric material represents a non-negligible fraction of the entire structure.

Piezoelectric Finite Elements

The constitutive equations of a linear piezoelectric material[3] are:

$$\{T\}=[c^E]\{S\}-[e]^T\{E\} \tag{1}$$

$$\{D\}=[e]\{S\}-[\varepsilon^S]\{E\} \tag{2}$$

where $\{T\}=\{T_{11}\,T_{22}\,T_{33}\,T_{23}\,T_{13}\,T_{12}\}$ is the vector of the mechanical stress, $\{S\}=\{S_{11}\,S_{22}\,S_{33}\,S_{23}\,S_{13}\,2S_{12}\}$ is the vector of mechanical strains, $\{E\}=\{E_1\,E_2\,E_3\}$ is the vector of electric field, $\{D\}=\{D_1\,D_2\,D_3\}$ is the vector of dielectric displacement, $[c]^E$ is the mechanical stiffness matrix for a constant electric field E, $[\varepsilon]^S$ is the dielectric constant matrix for constant mechanical strain S, $[e]$ is the piezoelectric coupling coefficients matrix, $[e]^T$ is transposed.

The dynamic equations of a piezoelectric continuum can be derived from the Hamilton principle, in which the Lagrangian and the virtual work are properly adapted to include the electrical contribution as well as the mechanical ones. The potential energy density of a piezoelectric material includes a contribution from the strain energy and from the electrostatic energy[2].

The electric field $\boldsymbol{E}$ is related to electrical potential ϕ by

$$\boldsymbol{E} = -\text{grad}\,\phi \tag{3}$$

and the mechanical strain $\boldsymbol{S}$ to the mechanical displacement u in the Cartesian coordinates by

$$S=\begin{bmatrix}\partial/\partial x & 0 & 0 & \partial/\partial y & 0 & \partial/\partial z\\ 0 & \partial/\partial y & 0 & \partial/\partial x & \partial/\partial z & 0\\ 0 & 0 & \partial/\partial z & 0 & \partial/\partial y & \partial/\partial x\end{bmatrix}^T\{u\}=[B]\{u\} \tag{4}$$

The elastic behavior of piezoelectric media is governed by Newton's law:

$$\text{div}\{T\}=\rho\frac{\partial^2\{u\}}{\partial t^2} \tag{5}$$

where ρ is the density of the piezoelectric medium, whereas the electrical behavior is described by Maxwell's equation, taking into account the fact that the piezoelectric media are insulating (no free volume charge):

$$\text{div}\{D\}=0 \tag{6}$$

Equations (1) to (6) constitute a complete set of differential equations, which can be solved with the appropriate mechanical (displacement and forces) and electrical (potential and charge) boundary conditions. An equivalent description of above boundary-wave problem is Hamilton's variational principle as extended to piezoelectric media,

$$\delta\int_{t_1}^{t_2}(L+W)\mathrm{d}t=0 \tag{7}$$

where the operator δ denotes the first-order variation, t_1 and t_2 define the time interval (all variations must vanish at $t = t_1$ and $t = t_2$) and the Lagrangian term L is determined by the energies available in the piezoelectric

medium and W is the virtual work of the external mechanical and electrical forces[1,2,4].

In the finite-element method the body to be computed is subdivided into small, discrete elements, the so-called finite elements. The mechanical displacement u and the forces f as well as the electrical potential ϕ and the charge q are determined at the nodes of these elements. The values of these mechanical and electrical quantities at an arbitrary position on the element are given by a linear combination of the polynomial interpolation function $N(x,y,z)$ and the nodal point values of these quantities as a coefficient. For an element with n nodes (nodal coordinates: (x_i, y_i, z_i), $(i=1,2,\ldots,n)$ the continuous displacement function $u(x, y, z)$ (vector of order three), for example, can be evaluated from its discrete nodal point vectors as follows (the quantities with "0" are the nodal point values of one element):

$$\{u(x,y,z)\} = [N_u(x,y,z)]\left\{{}^0u(x_i,y_i,z_i)\right\} \quad (8)$$

$$\phi = [N_\phi(x,y,z)]\left\{{}^0u(x_i,y_i,z_i)\right\} \quad (9)$$

where $\left\{{}^0u\right\}$ is the vector of the nodal point displacement and $[N_u]$ is the interpolation function for the displacement.

Therefore, the strain field $\{S\}$ and the electric field $\{E\}$ are related to the nodal displacement and potential by the shape-function derivatives $[B_u]$ and $[B_\phi]$ defined by,[12]

$$\{S\} = [B_u]\left\{{}^0u_i\right\} \quad (10)$$

$$\{E\} = -[B_\phi]\left\{{}^0\phi_i\right\} \quad (11)$$

The substitution of the polynomial interpolation function into (8) yields a set of linear differential equations that describe a single piezoelectric finite element.

$$\{M\}\left\{{}^0\ddot{u}\right\} + [K_{uu}]\left\{{}^0u_i\right\} + [K_{u\phi}]\left\{{}^0\phi_i\right\} = \left\{{}^0f_i\right\} \quad (12)$$

$$[K_{\phi u}]\left\{{}^0u_i\right\} + [K_{\phi\phi}]\left\{{}^0\phi_i\right\} = \left\{{}^0q_i\right\} \quad (13)$$

Each element k of the mesh is connected to its neighboring elements at the global nodes and the displacement is continuous from one element to the next. The element degrees of freedom (dof) $\left(\left\{{}^0u_i\right\}, \left\{{}^0\phi_i\right\}\right)$ are related to the global dof $(\{u\}, \{\Phi\})$ by the mean of the localization matrices $\left[{}^0L_u\right]$ and $\left[{}^0L_\phi\right]$:

Hamilton's principle (7) must be verified for the whole structure, which results in (by summation of the contribution from each finite element).[1,2,3,4,8]

$$\{M\}\{\ddot{U}\} + [K_{UU}]\{U\} + [K_{U\Phi}]\{\Phi\} = \{F\} \quad (14)$$

$$[K_{\Phi U}]\{U\} + [K_{\Phi\Phi}]\{\Phi\} = \{Q\} \quad (15)$$

where the assembled matrices are given by:

$[M] = \sum_i [L_{ui}]^T [M^{(i)}][L_{ui}]$ – kinematically consistent mass matrix

$[K_{uu}] = \sum_i [L_{ui}]^T [K_{uu}^{(i)}][L_{ui}]$ – stiffness matrix

$[K_{U\Phi}] = \sum_i [L_{ui}]^T [K_{u\phi}^{(i)}][L_{\phi i}]$ – piezoelectric "stiffness" matrix

$[K_{\Phi U}] = \sum_i [L_{\phi i}]^T [K_{\phi u}^{(i)}][L_{ui}]$ – transponse piezoelectric "stiffness" matrix

$[K_{\Phi\Phi}] = \sum_i [L_{\phi i}]^T [K_{\phi\phi}^{(i)}][L_{\phi i}]$ – dielectric "stiffness" matrix

$\{F\} = \sum_i [L_{ui}]^T [f_i]$ – external forces applied to the structure

$\{Q\} = \sum_i [L_{\phi i}]^T [q_i]$ – electrical charges brought to the electrodes

Equations (14) and (15) couple the mechanical variables $\{U\}$ and the electrical potentials $\{\Phi\}$.

Based on this formulation, a piezoelectric finite element of the type multilayered Mindlin shell and volume has been derived.[2,3]

For shell elements, it is assumed that the electric field and the displacement are uniform across the thickness and aligned on the normal to the mid-plane. The electrical degrees of freedom are the voltages ϕ_k across the piezoelectric layers; it is assumed that the voltage is constant over each element (this implies that the finite element mesh follows the shape of the electrodes). One electrical degree of freedom of the type voltage per piezoelectric layer is defined. The assembly takes into account the equipotentiality condition of the electrodes; this reduces the number of electric variables to the number of electrodes.

For volume elements, one additional degree of freedom of the type electric potential is **introduced** in each node of the piezoelectric volume element.

3 MODELING AND RESULTS

As for selecting the element types, the decision is based on the characteristics of the element type to the best model that applies to the problem, geometrically and physically. The material properties are required for most element types. Depending on the element types, the material properties may be linear or non linear; isotropic or anisotropic; and constant temperature-independent or temperature-dependent.

The starting points of the modeling of the effect of quartz are the differential equations (14) and (15). These equations are solved according to the FEM, supported by the ANSYS software, whereas the program was ADPL (ANSYS PARAMETRIC DESIGN LANGUAGE).

In this paper, ANSYS was used as a computational tool for modeling the piezoelectric effect [6,7]. For this purpose, a quartz sample is taken, with a density of 2695 kg/m^3 and these dimensions: 90 mm × 120 mm × 27 mm [5], (**Figure 2**). We know that the crystal quartz is

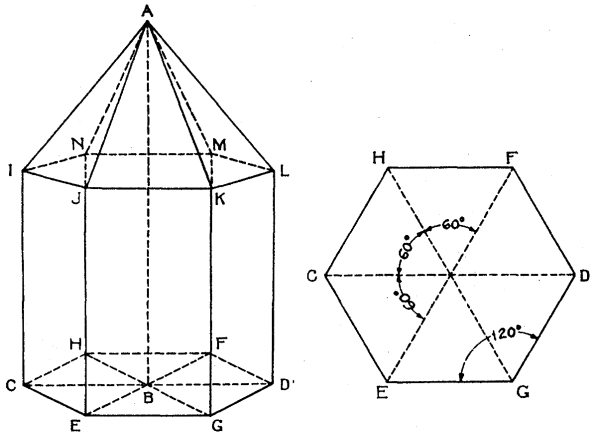

Figure1: A section of a quartz crystal showing the direction of the optical axes (AB) and the electrical axes (CD, EF, GH)[9]
Slika 1: Prerez kremenovega kristala in prikaz smeri optičnih osi (AB) in električnih osi (CD, EF, GH)

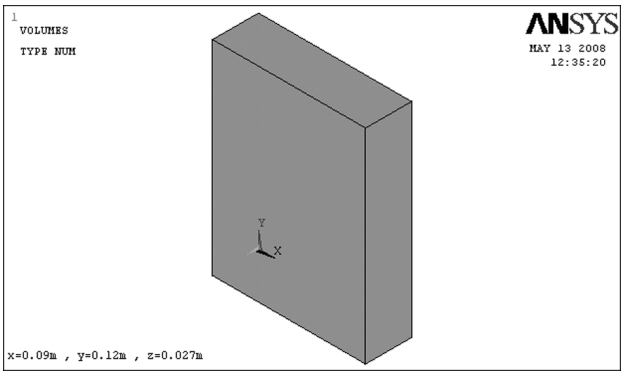

Figure 2: The quartz sample in the ANSYS window[7]
Slika 2: Kremenov vzorec v prikaznem oknu programa ANSYS

in the form of a hexagonal cylinder surmounted by a hexagonal pyramid; the faces of the crystal, which may vary in length and breadth, lie at definite angles with each other (**Figure 1**) [9,13]. Also, we know that pressure

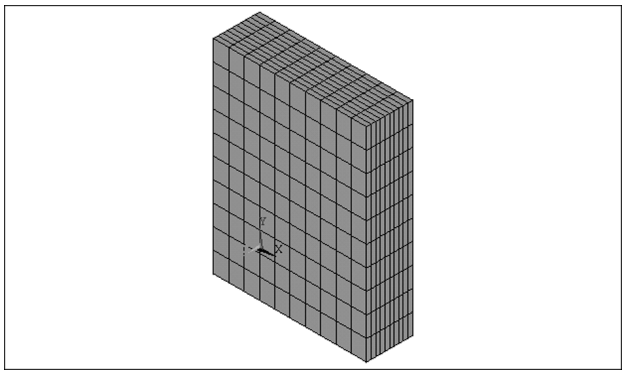

Figure 3: Meshing of the integral zone for the quartz sample[7]
Slika 3: Razdelitev integracijskega območja kremenovega vzorca v končne elemente

applied to the crystal parallel to electric axes produces a piezoelectric polarization in the same direction.

Then, according to the FEM, the meshing is carried out (the division of the domain of integration into the finite integrating elements) into 1000 elements with 1331 nodes, **Figure 3**, and **Table 1**.

As a finite element, from the library of ANSYS, the element SOLID 5 is taken, (**Figure 4**)[6,7]. The nodes of this element have degrees of freedom (dof): displacements along the axes *x, y, z*, the intensity of the electric potential, the intensity of the magnetic field and temperature, so this is a multi-field element. Since we are discussing the linear piezoelectricity, the displacements (mechanical quantities) and electric potential (electrical quantities) are of interest to us.

Coupled-fields in the ANSYS software can be treated on two ways to create a finite-element model: automatic meshing (also called the direct modeling in ANSYS terminology) and manual meshing (also called the direct generation in ANSY terminology). In automatic meshing the users are required to have a solid model available prior to the creation of a finite-element model. When such a solid model becomes available, the users can then

Table 1: Element and nodes of the sample[7]
Tabela 1: Matematični opis končnih elementov in vozlišč vzorca

Elements											Nodes			
LIST ALL SELECTED ELEMENTS. (LIST NODES)											LIST ALL SELECTED NODES. DSYS = 0 SORT TABLE ON NODE NODE NODE			
ELEM	MAT	TYP	REL	ESY	SEC	NODES					NODE	X	Y	Z
1	1	1	1	0	1	2	32	41	11	251 333 603 449	1	0.00000000000	0.120000000000	0.00000000000
2	1	1	1	0	1	32	33	42	41	333 334 684 603	2	0.00000000000	0.00000000000	0.00000000000
3	1	1	1	0	1	33	34	43	42	334 335 765 684	3	0.00000000000	0.108000000000	0.00000000000
4	1	1	1	0	1	34	35	44	43	335 336 846 765	4	0.00000000000	0.960000000000E-01	0.00000000000
5	1	1	1	0	1	35	36	45	44	336 337 927 846	5	0.00000000000	0.840000000000E-01	0.00000000000
6	1	1	1	0	1	36	37	46	45	337 338 1008 927	6	0.00000000000	0.720000000000E-01	0.00000000000
995	1	1	1	0	1	926	1007	396	387	197 206 148 149	1326	0.810000000000E-01	0.108000000000	0.108000000000E-01
996	1	1	1	0	1	1007	1088	405	396	206 215 147 148	1327	0.810000000000E-01	0.108000000000	0.135000000000E-01
997	1	1	1	0	1	1088	1169	414	405	215 224 146 147	1328	0.810000000000E-01	0.108000000000	0.162000000000E-01
998	1	1	1	0	1	1169	1250	423	414	224 233 145 146	1329	0.810000000000E-01	0.108000000000	0.189000000000E-01
999	1	1	1	0	1	1250	1331	432	423	233 242 144 145	1330	0.810000000000E-01	0.108000000000	0.216000000000E-01
1000	1	1	1	0	1	1331	530	350	432	242 142 133 144	1331	0.810000000000E-01	0.108000000000	0.243000000000E-01

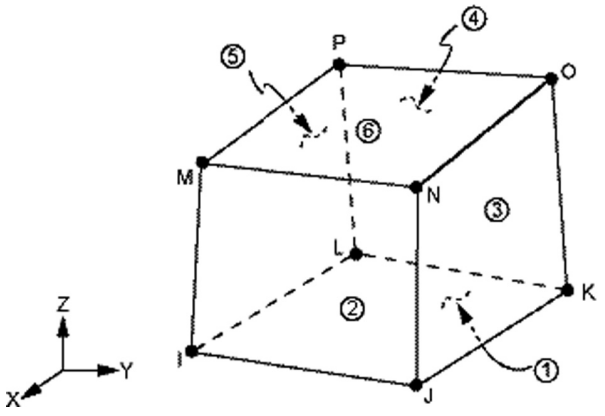

Figure 4: Geometry of the SOLID 5 [6,7]
Slika 4: Geometrija elementa SOLID 5 v programu ANSYS

instruct ANSYS to automatically develop a finite-element model (nodes and elements). The purpose of using automatic meshing is to relieve the user of the time-consuming task of building a complicated finite-element model. In manual meshing, the users need to define the nodes and elements directly (the development of a solid model is not required). The manual meshing method offers complete control over the geometry and connectivity of every node and every element, as well as the ease of keeping track of the identities of the nodes and elements. However, this method may not be as convenient as the automatic meshing method when dealing with a complicated finite-element model. It is, however, possible to combine both methods. In this paper we used the automatic meshing method. This is provided by the element SOLID 5, because it has a degree of freedom of different physical fields. SOLID 5 is a type of element that occupies three-dimensional space. In addition, it has eight nodes. Each of these nodes has three displacements along the *x, y* and *z* axes, respectively. The SOLID 5 element is capable of modeling seven different types of disciplines. When this particular type of discipline is chosen, ANSYS will only compute the behaviors of SOLID 5 in the UX, UY, UZ and VOLT degrees of freedom. It should be noted that UX, UY and UZ are to indicate the displacements in the *X, Y* and *Z* directions (the *X, Y* and *Z* axes are based on the global coordinate system), while VOLT is to indicate the difference in the potential energy of the electrical particles between two locations [6]. More precisely, when we have the action of the mechanical field, we can automatically obtain the output quantities of the electric field from the element SOLID 5, and vice versa (the case of the inverse piezoelectric effect).

Besides the geometry of the sample, the density of the quartz and the meshing, and introducing the element SOLID 5, we also have to take into account the other physical characteristics of quartz, in order to establish the initial condition for solving the differential equation. The physical characteristics that determine the solution of the differential equation are: the stiffness matrix c^E, the dielectric constant matrix ε^S, and the piezoelectric constant matrix e. The values for the above matrices at a temperature of 25 °C are: [8]

$$[c^E]=\begin{pmatrix} 86.74 & 6.99 & 11.91 & -17.91 & 0 & 0 \\ 6.99 & 86.74 & 11.91 & 17.91 & 0 & 0 \\ 11.91 & 11.91 & 107.2 & 0 & 0 & 0 \\ -17.91 & 17.91 & 0 & 57.94 & 0 & 0 \\ 0 & 0 & 0 & 0 & 57.94 & -17.91 \\ 0 & 0 & 0 & 0 & -17.91 & 39.88 \end{pmatrix} \cdot 10^9 \frac{\mathrm{N}}{\mathrm{m}^2} \quad (16)$$

$$[\varepsilon^S]=\begin{pmatrix} 39.21 & 0 & 0 \\ 0 & 39.21 & 0 \\ 0 & 0 & 41.03 \end{pmatrix} \cdot 10^{-12} \frac{\mathrm{C}}{\mathrm{V}\cdot\mathrm{m}} \quad (17)$$

$$[e]=\begin{pmatrix} 0.171 & -0.171 & 0 & -0.0406 & 0 & 0 \\ 0 & 0 & 0 & 0 & 0.0406 & -0.171 \\ 0 & 0 & 0 & 0 & 0 & 0 \end{pmatrix} \frac{\mathrm{C}}{\mathrm{m}^2} \quad (18)$$

Depending on the geometry of the sample, the physical characteristics of quartz, we have built a program to calculate the potential differences as a function of mechanical force, as well as the intensity of the deformation of the sample as a function of the electric voltage. In both cases, the calculations are carried out along the *x* axis (the electrical axis of the quartz). Below, we present the result of modeling for all cases: when the external mechanical forces compress the sample, when this force stretches the sample, and when an electric voltage is applied on the lateral faces of the sample (the inverse piezoelectric effect).

3.1.1 The direct piezoelectric effect (longitudinal)

The external mechanical forces compress sample

Assume that a mechanical force with intensity F is acting in the direction of the *x*-axis, i.e., in the direction of the normals of the lateral faces of the sample, in the positions $x = 0$ and $x = 90$ mm (in the opposite directions with the normal's vector)[9]. Then, as a result of the action of this force, the sample will be stressed. The intensity of this stress is the force on the unit of the surface *yz*, **Figure 5**. As a result of the action of a mechanical force, we will have the accumulation of a positive and negative

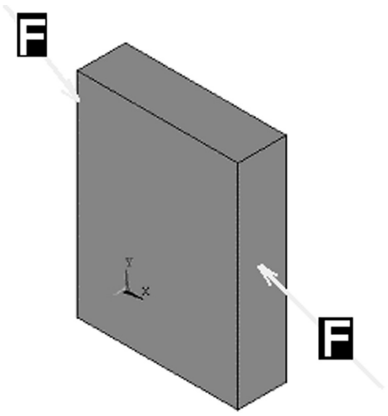

Figure 5: The force acting in the direction of the *x* axis
Slika 5: Mehanska sila pri stiskanju vzorca v smeri osi *x*

electrical charge on the opposite lateral faces of the sample along the *x*-axis. In other words, we will have the transformation of mechanical energy into electric energy. This phenomenon is called the direct piezoelectric effect.

Calculations are carried out for the cases when the force has the following intensities: 0.1 N, 0.08 N, 0.06 N, 0.04 N and 0.02 N. For these values of the intensities, we have calculated the potential difference as a function of depth. But, for practical reasons, we have not taken into account the fact that the opposite sides of the electrical poles in the interior of the sample are neutralized, and as a result the electric charges appear only on the surface. We made this approximation in order to prove the dependence of the intensity of the electrical potential on the depth. In **Figure 6** we have presented the modeling result for two cases.

The main results are the potential difference as a function of depth and the mechanical force, **Figure 7**.

According to **Figures 6 and 7** we can conclude the following:

- The intensity of the electrical potential depends on the external mechanical force. For equal depths the intensity of the potential increases with the increase of the force. This dependence is shown in **Table 2**.

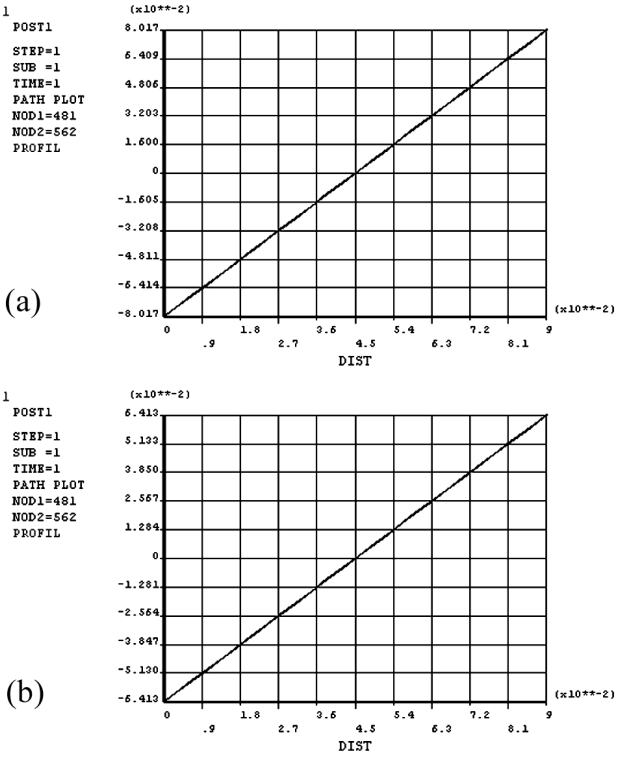

Figure 6: Potential difference as a function of depth and mechanical force – compression case: (a) F = 0.1 N, (b) F = 0.08 N

Slika 6: Prikaz izračuna razlike električnega potenciala v odvisnosti od razdalje s programom ANSYS – primer tlačne sile: (a) F = 0.1 N, (b) F = 0.08 N

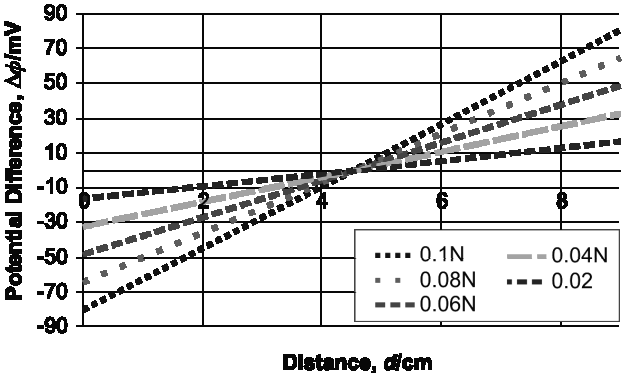

Figure 7: Potential difference [mV] as a function of depth [cm] and mechanical force F/N – compression case

Slika 7: Razlika električnega potenciala v odvisnosti od razdalje pri različnih silah stiskanja

Table 2: Potential difference [mV] as a function of depth [cm] and mechanical force F(N) – compression case

Tabela 2: Razlika električnega potenciala pri različnih silah stiskanja na robovih in v sredini vzorca

Force F/N	Depth, *d*/cm / Potential difference, $\Delta\phi$/mV		
	0	4.5	9
0.1	-80.17	0	80.17
0.08	-64.13	0	64.13
0.06	-48.10	0	48.10
0.04	-32.06	0	32.06
0.02	-16.03	0	16.03

- From **Table 2** and **Figures 6 and 7** we see that during the compression of the sample, in the interval from *x=0m* to *x=0.045m*, the electrical potential is negative, whereas on the other side, i.e., from *x=0.045m* to *x=0.09m* the potential is positive. It is known that the electrical potential is proportional to the intensity of the electric charge; therefore, we can conclude that on the upper part of the sample we have the accumulation of the negative charge and then, from the half-depth on, there is an accumulation of the positive charge.
- The accumulated electrical charge depends on the intensity of the external force and the depth. For a given force, the electrical charge decreases with an increase of the depth decrease of the thickness of the sample along the *x* axis, whereas for a certain depth, it increases with the increase of the force.

External mechanical forces stretches the sample

In **Figures 8 and 9** are the results of modeling for the case of stretching. From these figures we can draw the same conclusions as in the case of the stress of the sample. The only difference is that by changing the direction of the mechanical force, the sign of the electrical potential changes. More precisely, by changing the direction of the force, the side of the accumulation of the electric charges will switch. In the case of stretching, on the upper part of the sample the positive charge will be accumulated. In the other part of the sample (depth

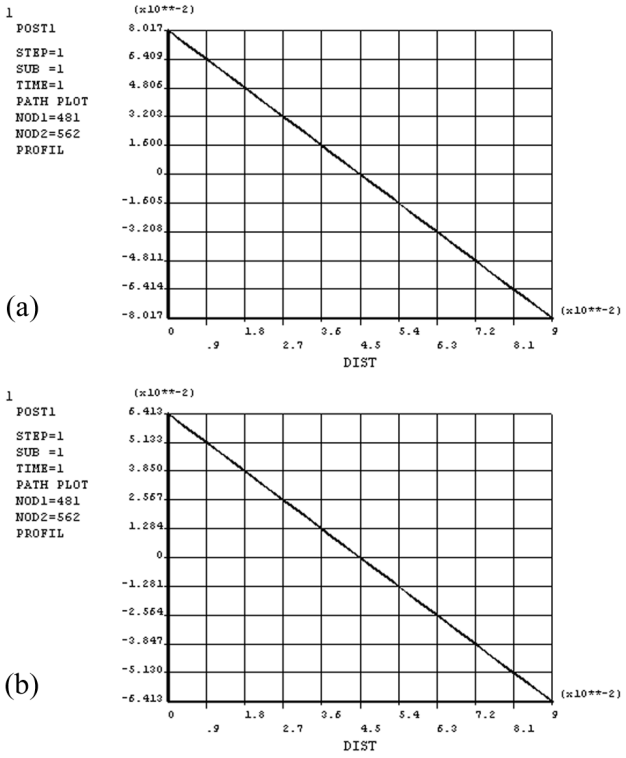

Figure 8: Potential difference as a function of depth and mechanical force – stretch case: (a) F = 0.1 N, (b) F = 0.08N

Slika 8: Prikaz izračuna razlike električnega potenciala v odvisnosti od razdalje za primer raztezne sile: (a) F = 0.1 N, (b) F = 0.08N

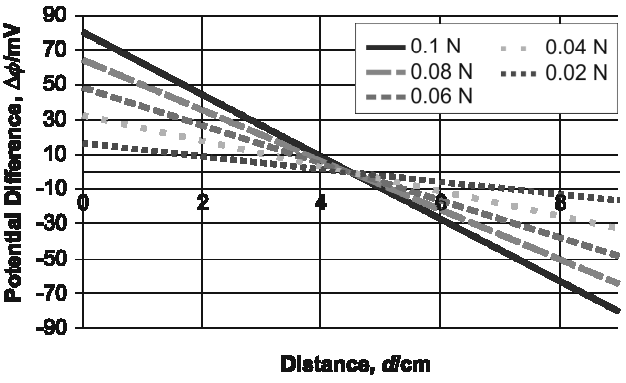

Figure 9: Potential difference [V] as a function of depth and mechanical force [F] – stretch case

Slika 9: Razlika električnega potenciala v odvisnosti od razdalje pri različnih razteznih silah

from *x=0.045m* to *x=0.090m*) the negative charge will be accumulated. In both cases at a depth of *x=0.045m* the electrical potential is zero, which means in the mid-depth of the sample the centers of positive electrical charges will coincide with the centers of the negative electrical charges and the net charge is zero. As a consequence, the electrical potential will also be zero.

3.1.2 The direct piezoelectric effect (transversal)

The same phenomena occur in the case when compression (stress) or stretch is applied along the *Y*-axis perpendicular to *X*. The only difference is that in the case of stress (compression) along the *Y*-axis, negative electrical charges are accumulated on the opposite side compared to the first case (when the sample was compressed or stretched in the direction of the *X*-axis. In **Figure 10**, the case for the force 0.1 N is shown, for the case when the sample is stressed or stretched along the *Y*-axis (the so-called transversal piezoelectric effect). The results presented in **Figure 10** show that the net accumulated electrical charge is not the same (for the same force in the case of transversal piezoelectricity, the net accumulated electric charge is greater). This occurs because in the case of longitudinal piezoelectricity, the net accumulated electrical charge depends only on the intensity of the applied force and the thickness of the sample, whereas in the case of the transversal piezoelectric effect, this net charge depends on the ratio between the surface area where the electrical charge is accumulated and the surface area upon which the force is exerted, $\frac{y \cdot z}{x \cdot z}$.

3.2 Converse piezoelectric effect

In this section we present the results of the inverse piezoelectric effect. The question is, what happens if an

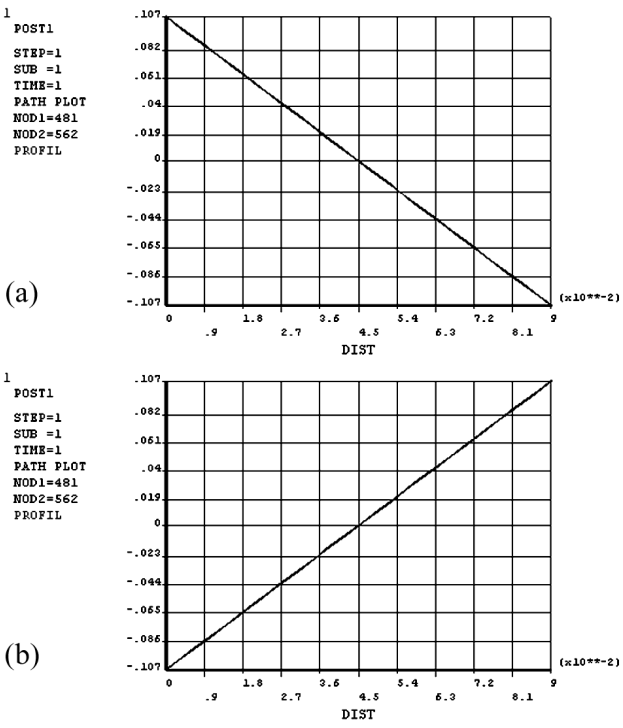

Figure 10: Transversal piezoelectric effect: (a) Case of specimen compression, (b) Case of specimen stretch

Slika 10: Transverzalni piezoelektrični pojav: (a) primer stiskanja in (b) primer raztezanja

external AC voltage is applied to the sample? From practice we know that piezoelectric materials (in our case the crystal is quartz) can change their physical dimensions with the application of an electric field. Again, we have taken a sample with the same geometry. The element for meshing is the same, whereas as the initial condition we take the voltage applied on the ends of the *x*-axis. We have analyzed what happens to a sample when an electrical voltage applied on it. This analysis belongs to the so-called modal analysis. With this analysis we can determine the process of oscillations

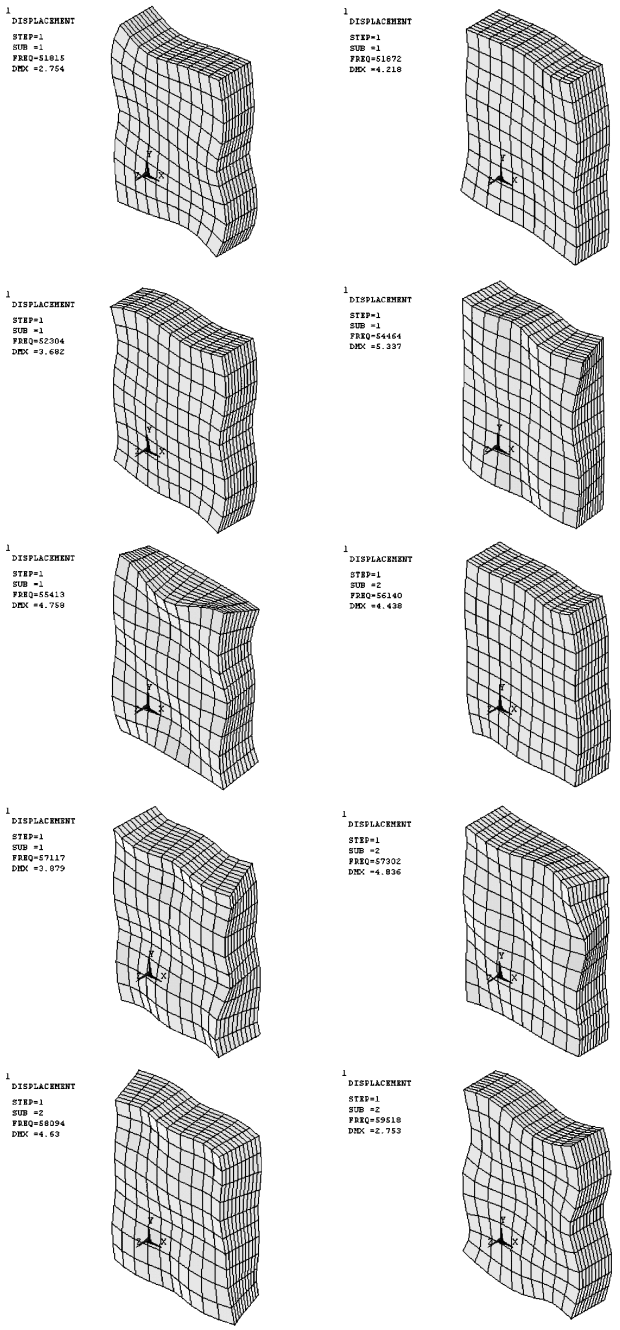

Figure 11: The first 10 modes of vibration and their shapes
Slika 11: Prvih 10 lastnih nihajnih načinov kremenovega vzorca

of a system[10]. More precisely, if the system performs oscillations under the action of an external factor, then with this analysis we find the proper frequencies of these oscillations and the shape of the oscillations (deformations of the system related to the initial undeformed shape). This part of the analysis is supported by the ANSYS software, with the condition that during the solution of the equation, it must be indicated that we are dealing with the modal type. The degrees of freedom of the element SOLID 5 provide the transfer from the quantities of one physical field to another.

In our case, the applied voltage is given as $U = 220$ V. Then the element SOLID 5 provides the transfer from this electrical quantity to the mechanical quantity – the displacement of the nodes or the deformation of the sample. The software (ANSYS) automatically calculates the frequency of the deformation – the oscillations of the nodes as well as its shape. With this program we can also find the frequencies of all modes of oscillations and their shapes for any applied voltage. In **Figure 11**, the 10 first modes of oscillations and their shapes are shown. According to[11], the frequencies of the oscillations along the electric axis *x* for the quartz take values from 50 Hz to 200 kHz. From the last presentation we see that the frequency of oscillations for the 10 first modes take the values 51 815 Hz to 59 518 Hz. We have proved that the other modes, for example, the 40th mode, has a frequency of 93 000 Hz, whereas the 100th mode has the frequency 120 819 Hz. The results also prove that under the voltage applied, the geometry of the sample is deformed and that this deformation is caused by oscillations with different frequencies.

It appears that an improvement in the computational accuracy of highly ordered modes depends, above all, on the number of finite elements used, and is not limited by the use of the finite-element method.

4 CONCLUSIONS

From the results obtained, presented in **Figures 5, 6, 7, 8, 9, 10** we can conclude as follows:

- In principle, the differential equation of the coupled-field (mechanical and electrical) is solvable with the finite-element method (FEM)
- The commodity of the solution provides the application ANSYS.
- Both types of piezoelectric effect can be modeled with the aid of the FEM package, whereas simulations in ANSYS prove the corrections of the theoretical model.
- For the direct piezoelectric effect, we proved that depending on the intensity of the force and its direction (stress or stretch), we have the accumulation of the electrical charges along the electric axis *x*, which can be seen in **Figures 7 and 9**.
- Modal analyses provide an elegant presentation of the different shapes of oscillations of the sample when an

electric voltage is applied to it. With this analysis we have proved the inverse piezoelectric effect.

- With the same procedure the piezoelectric effect can be modeled for other materials, when only the three characteristic matrices of the material are known.

5 REFERENCES

[1] H. Allik, T. J. R. Hughes, Finite element method for piezoelectric vibration, International Journal for Numerical Methods in Engineering, 2 (**1970**), 151–157

[2] V. Piefort, Finite Element Modeling of Piezoelectric Active Structures (doctoral thesis), University of Brussels, 2001, 51–69

[3] IEEE standard of piezoelectricity, Standards Committee of the IEEE Ultrasonics, Ferroelectrics, and Frequency Control Society, USA, 1988, 176

[4] G. L. C. M. de Abreu, J. F. Ribeiro, V. Steffen, Finite element modelin gof a plate with localized piezoelectric sensors and actauators, J. Of the Braz. Soc. Of Mech. Sci. & Eng, 26 (2004)2, 117–128

[5] www.korth.de/

[6] R. C. Tjiptoprojo, On a finite element approach to modeling of piezoelectric element driven compliant mechanisms (doctoral thesis), Saskatchevan, Canada, April 2005, 22–45

[7] ANSYS 2004

[8] Jiashi Yang, An introduction to the theory of piezoelectricity, Springer, Lincoln, 2005

[9] L. H. Dawson, Piezoelectricity of crystal quartz, Physical Review, April 1927, 532–541

[10] G. Mueller, C. Groth, FEM fuer Praktiker- Band I, Expert Verlag, 2002 Renningen, Germany

[11] www.axtal.de

[12] D. Boucher, M. Lagier, C. Maerfeld, Computation of the vibration modes for piezoelectric array transducers using a Mixed Finite Element-perturbation method, IEEE Transactions on Sonds and Ultrasonic, SU 28 (1981) 5, 318–330

[13] C. Z. Rosen, V. Basvaraj, V. Hiremath, R. Newnham, Piezoelectricity, Key Papers in Physics, (**1992**) 5, 227–248

[14] V. Kochin, J. Davaausambuu, U. Pietch, K. Schwarz, P. Blaha, The atomistic origin of the piezoelectric effect in α quartz, Journal of Physics and Chemistry of Solids, 65, (**2004**), 1967–1972

[15] J. N. Reddy, The finite element method, Department of Mechanical Engineering, Texas University, New York, 2005

[16] A. Benjeddou, Advances in piezoelectric finite element modeling of adaptive structural elements: a survey, Elsevier, Computers and Structures, 76 (**2000**), 347-363

[17] S. Avdiaj. Modelling of the piezoelectric effect (Master thesis), Tirana, Albania, July 2008

UDK 546.78:620.17:539.377
Original scientific article/Izvirni znanstveni članek

ISSN 1580-2949
MTAEC9, 43(6)293(2009)

VARIABLE THERMAL LOADING ANALYSIS OF (110) SINGLE CRYSTAL TUNGSTEN

ANALIZA SPREMENLJIVE TERMIČNE OBREMENITVE VOLFRAMOVEGA (100) MONOKRISTALA

Rathinam Murugavel

Paavai Institutions, Paavai Nagar, NH-7, Namakkal-637018, Tamilnadu, India
mrgvel@yahoo.com

Prejem rokopisa – received: 2009-05-21; sprejem za objavo – accepted for publication: 2009-07-13

The temperature response of properties of single crystal tungsten (110) is still not well understood. Tungsten was chosen to illustrate the temperature dependence behaviour because of its isotropic elastic behaviour at low loads. All the mechanical properties are temperature dependent. The experiments were performed with tailor made Berkovich tip of radius 100 nm at 265 K, 373 K, 473 K and 623 K to study the behavior of tungsten single crystal at various temperatures. The phenomenon of material under the indenter, bouncing back at the end of unloading due to the accumulation of energy was observed. It was noted that the elastic recovery was lower at higher temperature. The experiments showed the onset of the first strain burst, the onset of plastic deformation in connection with periodic bursts, and the softening effects. Pile up, significant drop in hardness, change of elastic modulus and increase in displacement with increasing temperature were observed. Because of softening, the indentation depth is increased for the same loading conditions. Clear bursts were seen showing the nucleation of dislocations. At higher peak loads, the indentation contact in tungsten was not just elastic. This work attempted to explore the complete behaviour of metals at various temperatures, including the initial burst, the complete elastic recovery, the softening effect, the modulus and hardness.

Keywords: Nanoindentation, Mechanical Properties, Tungsten, Effect of Temperature

Vpliv temperature na lastnosti monokristala volframa (100) še ni popolnoma razjasnjen. Volfram je bil izbran za prikaz temperaturne odvisnosti zaradi elastičnega izotropnega vedenja pri majhnih obremenitvah. Vse mehanske lastnosti so odvisne od temperature. Preizkusi so bili opravljeni s prirejeno Berkovichovo konico s polmerom 100 nm pri temperaturah 265 K, 373 K, 473 K in 623 K, da bi ugotovili vedenje monokristala volframa pri različnih temperaturah. Opažen je bil pojav v materialu, da se vtis po razbremenitvi s konico sprosti zaradi velike nakopičene energije. Elastična poprava je bila manjša pri visokih temperaturah. Poskusi prikazujejo začetek vtisa in plastično deformacijo, ki je povezana s periodičnimi vtisi in učinke mehčanja. Kopičenje materiala, zmanjšanje trdote in elastičnega modula ter povečanje razmika pri povišanju temperature je bilo tudi opaženo. Zaradi mehčanja se povečuje globina vtisa pri enaki obremenitvi. Deformacije je spremljal nastanek dislokacij. Pri velikih obremenitvah kontakt pri vtisu ni bil popolnoma elastičen.

Ključne besede: nanovtis, mehanske lastnosti, volfram, vpliv temperature

1 INTRODUCTION

The ability to perform nanotest measurements at elevated temperatures opens up significant new possibilities. The behavior of the material is different when subjected to temperatures deviating from the room temperature and the temperature response of tungsten is still not clearly understood. Thorough study of the behaviour of the materials in different temperatures is very important for the design and applications of materials for different operating conditions.

Experiments were already performed on (100) tungsten [1]. It was found that the yielding under contacts can produce a 250 nm displacement extrusion. Nano-indentation experiments on tungsten revealed that the load displacement was not linear and an analytic technique was proposed for determining the contact area at peak load [2].

Experiments were performed on single crystal ionic materials with ultra sharp tips with $R < 10$ nm and special attention was given to the elastic response before the onset of plastic yield [3]. The load displacement curves exhibit periodic bursts in indenter penetration depth that was interpreted chiefly as consequence of the nucleation of dislocations. Plastic deformation in polycrystalline copper films clearly revealed the existence of a significantly higher density of dislocations around the nanoindentation. The characterisation of mechanical properties of thin films using spherical tipped indenters were investigated, also [4] and it was shown that the use of very small spherical tipped indenters provided a better solution of the contact problem. The role of substrate and interface adhesion on the force-displacement behavior of thin films indented with spherical tipped indenters was discussed, also [4].

The analytical formulation of the elastic limit predicting the location and slip character of a homogeneously nucleated defect in crystalline metals extends this formulation to the atomic scale in form of an energy-based local elastic stability criterion was investigated [5]. A fundamental framework for describing incipient plasticity that combines results of atomistic and finite-element modeling, theoretical concepts of structural stability at finite strain and experimental

analysis were discussed, also [5]. Detailed interpretation of the experimentally observed sequence of displacement bursts was proposed to elucidate the role of secondary defect sources operating locally at stress levels considerably lower than the ideal strength required for homogeneous nucleation [6]. The advancements in making low dimensional structures from inorganic and organic compounds, determining the resulting, and necessarily local properties and assembling complex structures were explained[7].

The homogenous nucleation of dislocations was found in dislocation-free single crystals to be related to a sudden jump in the force-displacement curve. Experimental results of dislocation loop nucleation show good agreement with the continuum theory of dislocations[8]. It is found that the dislocations with a screw component are shown to glide across {111} planes and by a cross-slip mechanism giving rise to revolving terraces in the neighborhood of the nanoindentation trace with their edges parallel to compact n directions [9]. Molecular dynamics simulation showed that the burst and arrest of stacking faults were the key factors for the plastic deformation of nanocrystalline copper under nanoindentation [10]. High temperature nanotesting with micro materials measuring technology introduced the technique of high temperature nanoindentation [11]. The experiments were carried out on gold, soda-lime glass, fused silica and a polyimide. Results from fused silica show that its mechanical properties exhibit completely different temperature dependence from those of soda-lime glass, as expected since fused silica is an anomalous glass [12]. The small scale hardness and elastic modulus measurements on glass, gold, and single crystal silicon at room temperature and 473 K, show that the hardness and elastic modulus of soda lime glass and gold are lower at 473 K than at room temperature. In contrast, indentation testing of Si (100) at 473 K produced a similar hardness value to that obtained at room temperature, although the modulus was again reduced, from 140.3 GPa to 66.0 GPa. The 'pop out' event observed during unloading of a silicon indentation at room temperature, disappeared at 473 K [13].

The temperature response of properties of tungsten at high temperature is still not well understood, as relatively little research was focused on its high temperature behaviour [14] and the effect of temperature on dislocation nucleation process is not well understood. The behaviour of the material during loading and unloading was analyzed to understand the temperature effects on the reconstruction of the material during the removal of load. Emphases were placed on defects generation mechanisms during the elastic plastic contact of crystals and special attention was given to the elastic response before the onset of plastic yield. This work attempted to explore the complete behavior of tungsten at increased temperatures, including the initial burst, the complete elastic recovery, the softening effect, the modulus and the hardness.

2 EXPERIMENTAL METHODOLOGY

In the present investigation, the effects of temperature on properties of single crystal tungsten (110) were studied. The experiments were performed with tailor made Berkovich tip of radius 100 nm at temperatures of 265 K, 373 K, 473 K and 623 K. To perform the experiment at high temperature, insulating material was used to protect the piezoelectric setup of the indenter. A small heater capable of maintaining a constant temperature was added to the stage. The hot stage itself consisted of a thermally insulating ceramic block attached to the nanotest sample holder. The sample surface was brought to a constant temperature before the indentation for each experiment. A new attachment was made to circulate dry nitrogen gas to avoid ice formation during the low temperature experiments. The loading rate was kept constant for different temperatures experiments. The size of the sample was 2 mm thick and 9 mm in diameter. It took about 15 min. to reach the required temperature. The force on the sample during the imaging was of 2 mN. The topography and gradient images were captured to show the surface morphology after the indentation. In-situ imaging provides the capability to observe and quantify material damage while minimizing the time for material recovery. In the case of thin hard films on soft substrates, for instance, the indentation depth should generally not exceed 10 % of the film thickness in order to preclude any influence of the substrate. The sample was prepared with an advanced technique using the ultra precision machining technique producing a very fine surface. This method does not affect the orientation. But in case of other polishing methods, there is possibility of changing the orientation of the sample. Compared to other methods, this method also avoids the surface oxide formation.

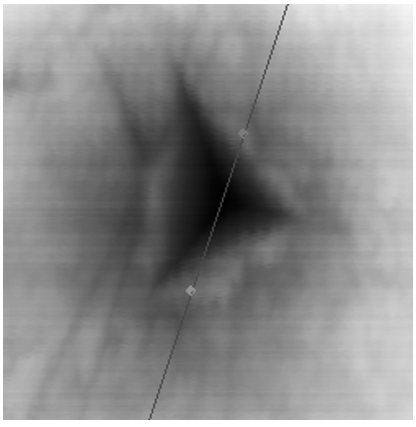

Figure 1: Image of the sample after indentation (6 μm)
Slika 1: Posnetek preizkušanca po vtisu (6 μm)

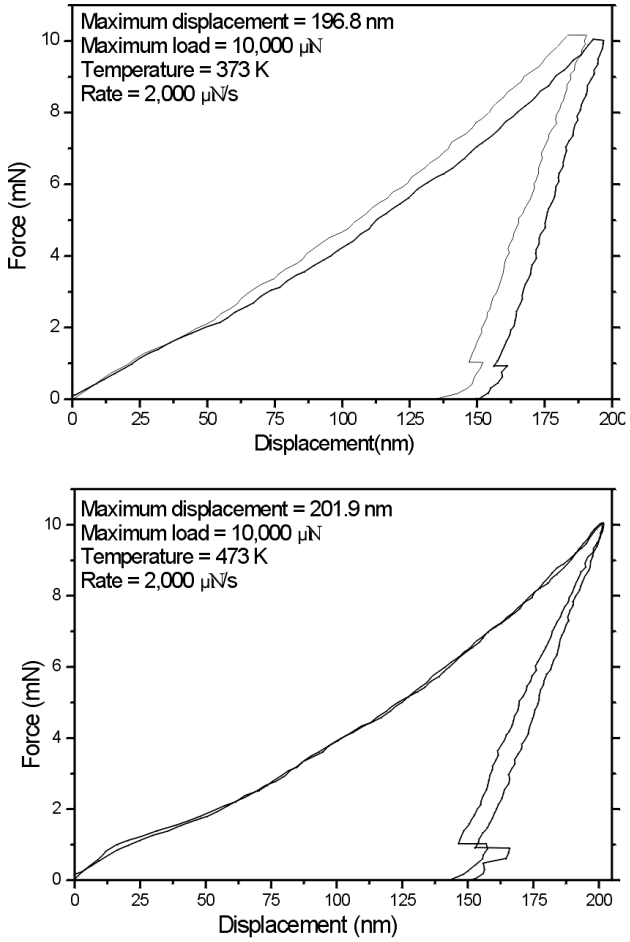

Figure 2: Loading and unloading pattern at 373 K (a) and 473 K (b) for 10,000 μN and loading rate of 2000 μN/s. Multiple curves indicate the experiments at different locations on the sample. The curves starting from the origin till the maximum point indicate the loading.

Slika 2: Značilnosti obremenitve in razbremenitve pri 373 K (a) in 473 K(b) pri 10 000 μN in hitrosti obremenitve 2000 μN/s. Krivulje pomenijo vtise na različnih mestih na preizkušancu. Krivulji z začetkom v koordinatnem središču pomenita obremenitev.

3 RESULTS AND DISCUSSION

Figure 1 shows the AFM image of the sample after the indentation. The tip imprint is very clear. The displacement of the material on the surface indicates the dislocation pile-ups of the material during the indentation.

Figure 2 shows the loading and recovery process during loading and unloading at different temperatures and at the maximum load of 10 000 μN and loading rate of 2000 μN/s. These curves were obtained for the purpose of comparison during the loading and unloading process and to observe the maximal penetration depth and elastic rebound. The end of unloading curve in **figure 2** shows the sudden bump in the unloading curve for a short distance. Also, we observed a small increase in the penetration depth indicating the softening effects at higher temperatures. The softening effects were due to increase in temperature and plasticity. At high temperatures, the material was subjected to great plastic global deformation, instead of periodic local burst of dislocations at low temperature. The pile up was clearly visible an explained with the rotation of the axis of the atoms to conserve the volume during the penetration of the indenter. We could also note the elastic rebound at the end of loading.

Figure 3 shows the loading and recovery process during loading and unloading at higher temperature. The

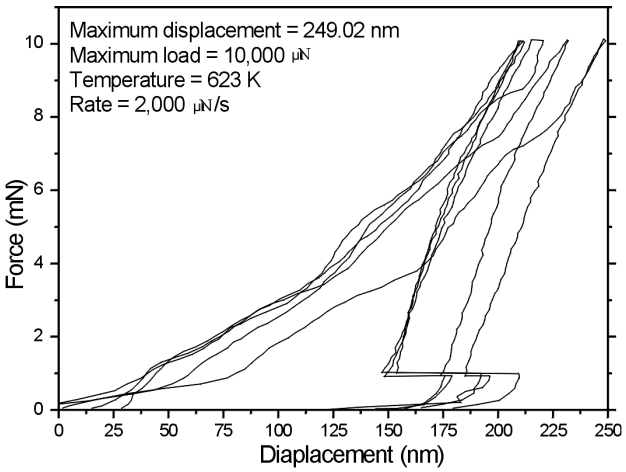

Figure 3: Loading and unloading pattern at 623 K for 10,000 μN and loading rate of 2000 μN/s. Multiple curves indicate the experiments at different locations on the sample. The curves starting from the origin till the maximum point indicate the loading.

Slika 3: Značilnosti obremenitve in razbremenitve pri 623 K pri 10 000 μN in hitrosti obremenitve 2 000 μN/s. Krivulje pomenijo vtise na različnih mestih na preizkušancu. Krivulji z začetkom v koordinatnem središču pomenita obremenitev.

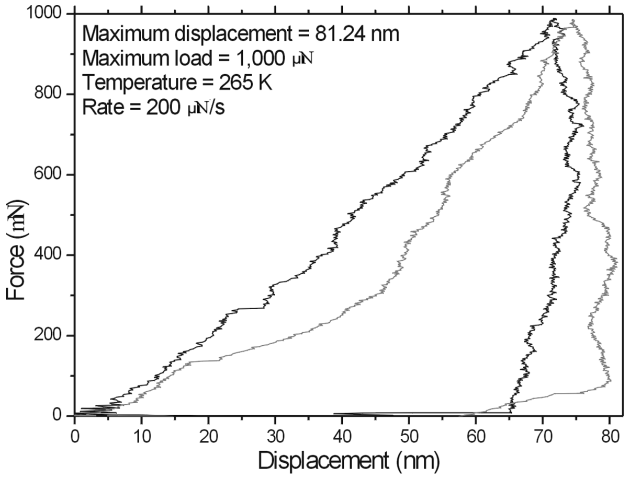

Figure 4: Loading and unloading pattern at 265 K for 1,000 μN and loading rate of 200 μN/s. Multiple curves indicate the experiments at different locations on the sample. The curves starting from the origin till the maximum point indicate the loading.

Slika 4: Značilnosti obremenitve in razbremenitve pri 265 K pri 1 000 μN in hitrosti obremenitve 200 μN/s. Krivulje pomenijo odtise na različnih mestih na preizkušancu. Krivulji z začetkom v koordinatnem središču pomenita obremenitev.

displacement of the material under the indenter was large compared to the displacement at 373 K and 473 K, indicating the softening of the metal at higher temperature. Also, **Figure 3** exhibits a similar kind of unloading curve. The exact data on the amount of softening will enable the proper selection of materials for different thermal loading conditions. The softening effects observed at higher temperatures below the recrystallization temperature are useful for the proper selection of materials for variable thermal loading conditions as the softening effects increase the plasticity. As global, the deformation is understood, which involves the entire body, in contrast to poking and squeezing, which involve relatively small regions of the deformable object. It was also noted that the elastic recovery was smaller at higher temperatures.

Figure 4 was obtained to study the initial burst and the periodic bursts clearly visible at low loading rate and load when the initial burst was clearly observed, while, it was not visible at greater load. During loading and unloading at low temperature, the curves exhibit large vibration. The unloading curve was not linear and was similar to that for copper. The material recovery rate was less and rebounding sharp at the end of the recovery process by low temperatures and loading conditions. The curve shoved, also, that the elastic recovery was minimal as the displacement smaller. Also the curves at 265 K showed a brittle behavior, because the material withstanded higher load before first yield. As evident from the curves, the initial burst occurred very early, while, the metal accommodated in itself without significant pile up. Displacement bursts were due to nucleation of dislocations. At low temperarute, the material exhibited brittle behavior and at 265 K, the recovery rate was less and, at the end of the recovery process, the rebounding was sharp.

In **Tables 1 and 2**, it can be noted that the difference between $h_{plastic}$ and h_{max} varied with the tests temperature showing that the plasticity range increased with the temperature and the displacement. Also, the recovery range increased comparatively and it was proportional to the displacement. The overall plastic region increased as the displacement was large at higher temperatures. In other words, the elastic recovery was lower at higher temperature, while the displacement was greater. As shown in **Tables 1 and 2**, the loading rate and load also affected the hardness value as seen in **Tables 1 and 2**. The elastic modulus (E) was high by great difference $h_{plastic}$ and h_{max} and h_{eff} was high, also. The elastic modulus decreases with the temperature, while, the penetration depth increases.

The difference $h_{plastic}$ and h_{max} was less at smaller loading rate and indicated that the loading rate affects the range of plasticity. Also, it was noted that the elastic modulus (E) was high when the difference between plastic displacement ($h_{plastic}$) and maximum displacement (h_{max}) was large. The hardness (H) value does not depend on the difference $h_{plastic}$ and h_{max}. The maximum displacements (h_{max}) in **Tables 1 and 2** shows the softening effects at different temperature and can be used for the proper materials selection for different thermal loading conditions.

Table 1: Data for a load of 1000 μN and loading rate of 200 μN/s
Tabela 1: Podatki za obremenitev 1 000 μN in hitrost obremenitve 200 μN/s

Temp/ Data	h_{max}/nm	$h_{plastic}$ /nm	H/GPa	E/GPa
265 K	76.16	72.31	4.02	576.64
	81.24	77.83	3.55	6297.58
	52.48	49.38	7.53	9190.52

Table 2: Data for a load of 10,000 μN and loading rate of 2,000 μN/s.
Tabela 2: Podatki za obremenitev 10 000 μN in hitrost obremenitve 2 000 μN/s

Temp/ Data	h_{max} / nm	$h_{plastic}$ / nm	H/GPa	E/GPa
373 K	190.62	154.24	12.22	202.16
	196.79	163.75	10.9	209.17
473 K	201.9	163.98	10.91	182.65
	201.29	149.86	12.69	144.8
623 K	249.02	191.92	8.28	105.82
	231.93	172.25	10.01	111.22
	211.49	141.71	14.09	112.84
	212.03	148.37	13.01	118.86
	231.93	172.25	10.01	111.22

4 CONCLUSIONS

The tests on tungsten showed that different events occur in the metal during the penetration of the indenter and the unloading at different temperature. Clear bursts showed the nucleation of dislocations and pile up was observed. It was found that the load displacement was not linear during unloading and that at higher peak load the indentation contact in tungsten was not purely elastic. At high temperature, the material showed higher dislocation mobility and a greater plastic deformation. It was concluded that the stored dislocations and the thermal recovery were responsible for maintaining a high mobile dislocation density that was temperature-dependent and sustained a large uniform elongation. At higher temperature the deformation was global, unlike the multi-bursts (brittleness) due to local dislocation motion at low temperatures. Changes of force and rate indicate to strain bursts due to the breakout of dislocations. The maximual displacements (h_{max}) at higher temperatures indicate that significant softening may occur at sufficiently high stress. Tungsten (111) planes showed lower hardness values than (110) planes as also evident from the results from investigations on aluminum.

The noise in the loading and unloading curves at low temperature can be improved by cooling to a lower level and then heating to the required temperature. The small

variations in the penetration depths in the *p-h* curves for same testing conditions must be avoided in case of single crystal. Our experiments clearly showed the onset of the first strain burst, the onset of plastic deformation in connection with the periodic bursts, and the strain hardening/softening/ recovery effects. The elastic modulus was lower at higher temperaturesand the softening increased with the increase of indentation depth for the same loading conditions. The elastic recovery was smaller at higher temperatures. The pop-ins shown on *p-h* curves correspond to the formation of dislocations. The contact pressure (nanohardness) increased with decreasing indentation depth. We attribute the temperature effect to the increased dislocation mobility and the reduced dislocation density. Dislocation pile up around the indentation was clearly visible.

The onset of plastic deformation was identified from the periodic bursts. The difference in pile up was observed for different temperature and the new phenomenon of material under the indenter bouncing back at the end of unloading was established, also. Because of dynamic softening the penetration depth and plastic deformation were greater at higher temperature. The indentation rate affected the modulus and the hardness.

5 REFERENCES

[1] William W. Gerberich, Natalia I. Tymiak, Donald E. Kramer, Fundamental aspects of friction and wear contacts in <100> surfaces, Mater. Res. Soc. Proc., 649 (2000)

[2] W.C. Oliver, G. M. Pharr, An improved technique for determining hardness and elastic modulus using load and displacement sensing indentation experiments, J. Mater. Res., 7 (**1992**), 1569

[3] J. Fraxedas, S. Garcia Manyes, P. Gorostiza, F. Sanz, Nanoindentation: Toward the sensing of atomic interactions, PNAS, 99 (**2002**), 5228–5232

[4] M. V. Swain, J. Mencik, Mechanical property characterization of thin films using spherical tipped indenters, Thin Solid Films, 253 (**1994**), 1–2, 204–211

[5] Krystyn J. Van Vliet, Ju Li, Ting Zhu, Sidney Yip, Subra Suresh, Quantifying the early stages of plasticity through nanoscale experiments and simulation, Phys. Rev. B, 67 (**2003**), 104–105

[6] Ju Li, Krystyn J. Van Vliet, Ting Zhu, Sidney Yip, Subra Suresh, Atomistic mechanisms governing elastic limit and incipient plasticity in crystals, Nature, 418 (**2002**), 307–310

[7] Dawn A. Bonnell, Materials in Nanotechnology: New structures, new properties, new complexity, J. Vac. Sci. Technol. A, 21 (**2003**), S194–S206

[8] D. Lorenz, A. Zeckzer, U. Hilpert, P. Grau, H. Johansen, H. S. Leipner, Pop-in effect as homogeneous nucleation of dislocations during nanoindentation, Physical Review B, 67 (**2003**), 172101

[9] E. Carrasco, O. Rodriguez de la Fuente, M. A. Gonzalez, J. M. Rojo, Dislocation cross slip and formation of terraces around nanoindentations in Au(001), Phys. Rev. B, 68 (**2003**), 180102

[10] Xin-Ling Ma, Wei Yang, Molecular dynamics simulation on burst and arrest of stacking faults in nanocrystalline Cu under nanoindentation, Nanotechnology, 14 (**2003**), 1208–1215

[11] High temperature NanoTesting, MICRO MATERIALS measuring nanotechnology-http://freespace.virgin.net/micro.materials/

[12] Ben, D. Beake, James, F. Smith, High-temperature nanoindentation testing of fused silica and other materials, Philosophical Magazine A, 82 (**2002**), 2179–2186

[13] J. F. Smith, S. Zhang, High temperature nanoscale mechanical property measurements, Surface Engineering, 16 (**2000**), 143–146

[14] J. A. Zimmerman, C. L. Kelchner, P. A. Klein, J. C. Hamilton, S. M. Foiles, Surface step effects on nanoindentation, Phys. Rev. Lett., 87 (**2001**), 165507-1

UDK 669.715:669.793:539.3
Original scientific article/Izvirni znanstveni članek

ISSN 1580-2949
MTAEC9, 43(6)299(2009)

SUPERPLASTICITY OF THE 5083 ALUMINIUM ALLOY WITH THE ADDITION OF SCANDIUM

SUPERPLASTIČNOST ALUMINIJEVE ZLITINE 5083 Z DODATKOM SKANDIJA

Anton Smolej[1], Brane Skaza[1], Edvard Slaček[2]

[1]University of Ljubljana, Faculty of Natural Science and Engineering, Aškerčeva 12, 1000 Ljubljana, Slovenia
[2]Impol, Aluminium Industry, 2310 Slovenska Bistrica, Slovenia
anton.smolej@ntf.uni-lj.si

Prejem rokopisa – received: 2009-07-14; sprejem za objavo – accepted for publication: 2009-08-24

This paper deals with the superplastic properties of an Al-4Mg-0.6Mn alloy (AA5083) with the mass fraction of scandium 0.3 %. The investigated alloy was produced by ingot casting and thermomechanically treated with hot and cold rolling into sheet with a thickness of 1.4 mm. The superplastic properties of the alloy were investigated with tensile tests at strain rates in the range 3×10^{-4} s^{-1} to 1×10^{-2} s^{-1} and at temperatures from 470 °C to 570 °C. The true-stress, true-strain characteristics, the elongation to failure, the strain-rate sensitivity index and the microstructure of the alloy were determined. The elongation to failure increased with the test temperature and was over 1400 % at an initial strain rate of 7.5×10^{-4} s^{-1} and a temperature of 550 °C.

Key words: 5083 aluminium alloy, scandium, superplasticity

Članek obravnava superplastične lastnosti zlitine Al-4Mg-0.6Mn (AA5083) z dodatkom masnega deleža skandija 0,3 %. Zlitina je bila izdelana pri laboratorijskih pogojih z ulivanjem v jekleno kokilo in termomehansko obdelana z vročim in hladnim valjanjem v pločevino z debelino 1,4 mm. Superplastične lastnosti zlitine so bile preiskane z nateznim preizkusom pri preoblikovalnih hitrostih 3×10^{-4} s^{-1} do 1×10^{-2} s^{-1} in temperaturah od 470 °C do 570 °C. Določene so bile odvisnosti dejanska napetost-dejanska deformacija, razteznosti, indeksi občutljivosti za preoblikovalno hitrost in mikrostruktura preizkusne zlitine. Največja razteznost več kot 1400 % je bila dosežena pri začetni preoblikovalni hitrosti $7{,}5 \times 10^{-4}$ s^{-1} in temperaturi 550 °C.

Ključne besede: aluminijeva zlitina 5083, skandij, superplastičnost

1 INTRODUCTION

Superplasticity is the ability of polycrystalline materials to exhibit high tensile elongations prior to failure under special forming conditions. These elongations are up to 1000 % and sometimes higher. Superplastic sheet metals enable the fabrication of complex-shaped products with a single working operation using relatively inexpensive tools. From among the numerous materials with superplastic properties, aluminium alloys like AA2004 (Al-Cu-Zr), AA7075, AA7475 (Al-Zn-Mg-Cu) and AA5083 (Al-Mg-Mn) are of commercial interest.[1–3] The requirements for the superplastic behaviour of alloys are well known.[4,5] In general, the following conditions need to be satisfied to achieve superplasticity: (1) a very small grain size (<10 μm); (2) a deformation temperature above $0.5T_m$; (3) a strain-rate interval in the tensile test within the range 1×10^{-5} s^{-1} to 1×10^{-1} s^{-1}; and (5) a low flow stress (<10 N mm^{-2}) during the superplastic forming (SPF).

The strain rates at which superplasticity normally occurs in aluminium alloys (<1×10^{-3} s^{-1}) are often too slow for industrial applications. In recent years, there have been numerous attempts to produce aluminium-based materials that would exhibit a high-strain-rate (>1×10^{-2} s^{-1}) superplasticity combined with a low-temperature (<400 °C) superplasticity.[6–8] This can generally be achieved by further refining the grain size using a complex thermomechanical treatment that involves large reductions during cold rolling, by new processes such as equal-angular channel pressing[7, 9] or by adding small amounts of Cu, Cr, Zr or Sc to the base alloy.[10–12]

AA5083 is one of the principal aluminium alloys used for SPF and its superplastic characteristics have been extensively investigated.[3,6,13–15] Generally, with this alloy, maximum elongations to failure of about 400 % and, rarely, up to 600 %[3] were achieved at slow or intermediate strain rates of 1×10^{-4} s^{-1} to 5×10^{-3} s^{-1}. It is now well established that small quantities of scandium added to the Al-Mg-[16,17] and Al-Mg-Mn-[18,19] type alloys lead to an increase in the superplasticity. Elongations without failure of 1020 % and 1130 % were reported for Al-4Mg-0.5Sc[16] and for Al-6Mg-0.3Sc[17], whereas an elongation of 680 % has been achieved for a conventionally manufactured Al-Mg-Mn alloy with mass fractions 0.25 % Sc and 0.12 % Zr at 1.67×10^{-3} s^{-1} and at 490 °C.[19]

The present paper describes the effect of a 0.33 % addition of scandium on the superplastic behaviour of a standard 5083 alloy. The examined alloy sheet was prepared by a simple thermomechanical treatment similar to conventional industrial processing. The aim of the investigation was to determine the superplastic properties of the sheet, which are characterised by the flow stresses,

the elongations to failure, the strain-rate sensitivity indexes and the microstructure.

2 EXPERIMENTAL

The Al-4Mg-0.6Mn-0.3Sc alloy was prepared by induction melting using Al99.9, Mg99.8, the master alloys Al-2.1Sc, Al-80Mn and Al-5Ti-1B. The melt was cast into a steel mould with dimensions of (175 × 80 × 27) mm. The chemical composition of the alloy is shown in **Table 1**.

Table 1: The chemical composition of the investigated alloy (in mass fractions *w*/%)
Tabela 1: Kemična sestava preiskovane zlitine (v masnih deležih w/%)

Si	Fe	Mn	Mg	Ti	B	Sc	Al
0.0064	0.0151	0.6400	4.054	0.0189	0.0024	0.329	Bal.

The ingots in the as-cast condition were homogenized for 4 h at 440 °C and for 4 h at 460 °C, and then air cooled. The scalped ingots with a thickness of 25 mm were hot rolled at 400 °C to a thickness of 8.8 mm, annealed for 4 h at 475 °C, and then subsequently cold rolled to a final sheet thickness of 1.4 mm with a reduction of 84 %. The samples for the tensile tests were machined from cold-rolled sheet along the rolling direction with a gauge section of 10 mm of length and 5.4 mm of width. The samples were annealed for 2 h at 500 °C to obtain a recrystallized microstructure. The average size of the recrystallized grains in the rolling direction was about 14 μm, and in the traverse section the size was about 8 μm.

The tensile tests of the investigated alloy were conducted on a Zwick Z250 testing machine with a 500 N load cell. The machine was equipped with a three-zone electrical resistance furnace. The testing chamber with a controlled temperature was over 300 mm in length. The testing procedure was conducted with the TestXpert II software system.

The measurements included determinations of the flow stresses, the maximum elongations to failure and the strain-rate sensitivity index *m*. The testing temperatures and strain rates ranged from 470 °C to 570 °C and from 3×10^{-4} s^{-1} to 1×10^{-2} s^{-1}. The tensile tests were conducted at constant strain rates (CSRs) and at constant cross-head speeds (CCHSs). The strain-rate sensitivity indexes were determined with the multi-strain-rate jump test. The microstructures of the tested samples were examined with light microscopy.

3 RESULTS AND DISCUSSION

The superplastic properties of the material were characterised by the flow behaviour during the tensile test. The flow stresses and the shapes of the flow curves are dependent on the temperature and the initial strain rate during the CCHS test. **Figure 1** shows a series of true- stress, true-strain curves for the investigated alloy at various temperatures in the range from 470 °C to 550 °C at an initial strain rate of 1×10^{-3} s^{-1}. The stress exhibits a sharp peak after loading, followed by a softening at lower temperatures (<490 °C), and then by a continuous hardening to failure at higher temperatures. The stresses were lower than 12 Nmm^{-2} for all the tested conditions and no steady state occurred. A similar course of stress-strain curves was observed for various initial strain rates at a temperature of 550 °C (**Figure 2**). After a rapid increase of the stresses to approximately 5 % strain, the tests performed at faster initial strain rates show no, or very little, increase of the flow stresses, whereas there is an indication of material hardening at lower initial strain rates (<1×10^{-3} s^{-1}).

The reason for the strain hardening of this alloy at higher temperatures and lower strain rates is the dynamic grain growth during the pulling of the samples.[17,18] Generally, the shapes of the true-stress, true-strain curves

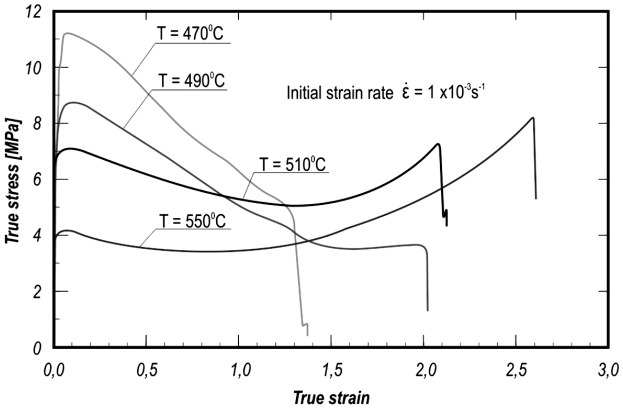

Figure 1: True-stress, true-strain curves for various tested temperatures at an initial strain rate of 1×10^{-3} s^{-1} (CCHS test)
Slika 1: Odvisnosti dejanska napetost – dejanska deformacija pri različnih preizkusnih temperaturah in začetni preoblikovalni hitrosti 1×10^{-3} s^{-1} (CCHS preizkus)

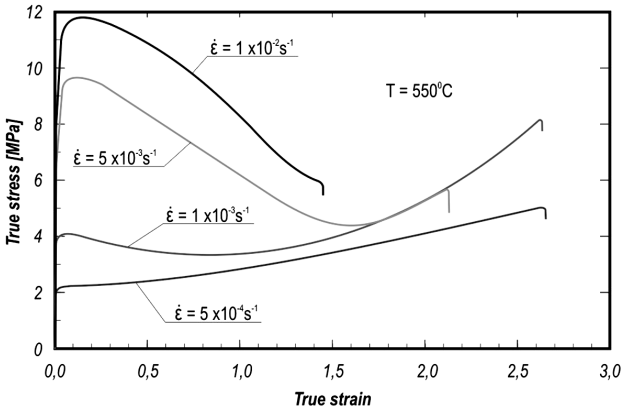

Figure 2: True-stress, true-strain curves for various initial strain rates at 550 °C
Slika 2: Odvisnosti dejanska napetost – dejanska deformacija pri različnih preoblikovalnih hitrostih in temperaturi 550 °C

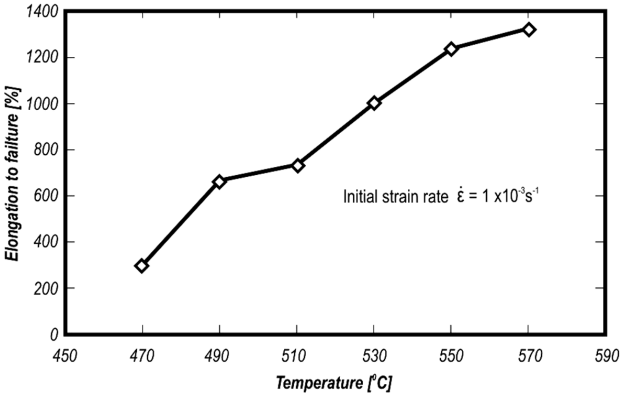

Figure 3: Elongation to failure as a function of the tested temperature at an initial strain rate of 1 x 10^{-3} s^{-1}

Slika 3: Raztežnost pri različnih preizkusnih temperaturah in začetni preoblikovalni hitrosti 1 x 10^{-3} s^{-1}

of the investigated Al-4Mg-0.6Mn-0.3Sc alloy are comparable with the curves of alloys with similar compositions, like Al-Mg-Mn,[3,14,15] Al-Mg-Sc[17,18] and Al-Mg-Mn-Sc.[6]

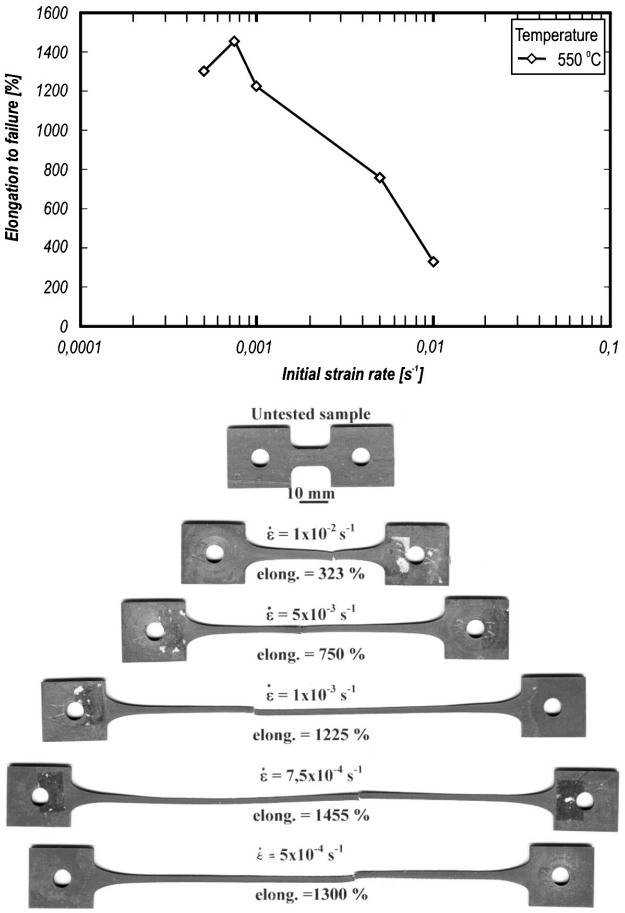

Figure 4: Elongation to failure as a function of initial strain rate and the samples after tensile testing at 550 °C

Slika 4: Raztežnost pri različnih začetnih preoblikovalnih hitrostih in preizkušanci po nateznem preizkusu pri 550 °C

The elongations to failure were measured with a tensile test under constant cross-head speed (CCHS) at temperatures in the range from 470 °C to 570 °C and at initial strain rates from 5 × 10^{-4} s^{-1} to 1 × 10^{-2} s^{-1}. The elongation to failure depended strongly on the test temperatures (**Figure 3**) and on the strain rate (**Figure 4**).

An elongation of over 1000 % was achieved at initial strain rates up to 1 × 10^{-3} s^{-1} and 550 °C (maximum elongation of 1455 % at 7.5 × 10^{-4} s^{-1}). Since a 200 % elongation can be considered as an initial indicator of superplasticity,[8,20] elongations at higher strain rates up to 1 × 10^{-2} s^{-1} at 550 °C and lower temperatures in the range from 470 °C to 510 °C are still in the superplastic regime.

The strain-rate sensitivity index m is one of the most important parameters that characterize the superplastic behaviour of a material. In this work the m values as a function of the strain rate at a temperature of 550 °C were estimated with the multi-strain-rate jump test. These tests were conducted by increasing and decreasing the strain rate by 20 % for every 100 % increment of elongation. The indexes m are plotted as a function of the strain rate for strains in the range from 1.1 (200 %) to 2.1 (700 %) in **Figure 5**. The index m changes at all strains with the strain rate. The m plots show peaks that occur within a narrow range of strain rates from 3 × 10^{-4} s^{-1} to 5 × 10^{-4} s^{-1}. A maximum value of m = 0.67 was obtained in this range at a true strain of 1.1 and m = 0.46 at ε = 2.1 and at strain rate 5 × 10^{-4} s^{-1}. The peaks of the m-plots are shifted to a lower strain rate at higher strains.

The microstructure of the alloy was examined with regard to the crystal grains after pulling the samples at an initial strain rate of 7.5 × 10^{-4} s^{-1} and a temperature of 550 °C to various elongations in the range from 200 % to 1200 % (**Figure 6**). The initial microstructure consisted of recrystallized grains grown during the two hours of annealing prior to the tensile test. The static and dynamic grain growth in the grip and in the gauge sections of the samples as a function of annealing or of pulling time during the tensile test are shown in **Figure 7**. The

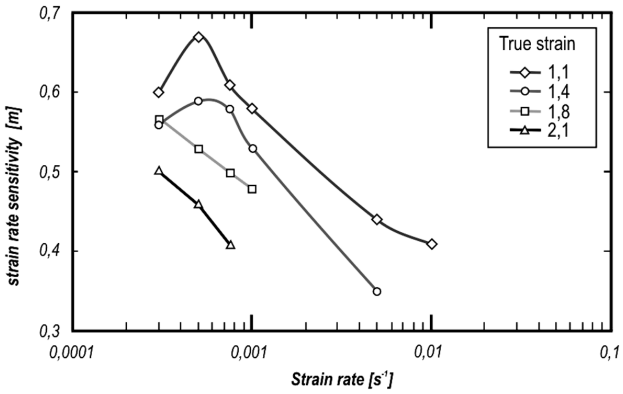

Figure 5: Strain-rate sensitivity index m as a function of the strain rate for various strains at 550 °C

Slika 5: Indeks občutljivosti za preoblikovalno hitrost m pri različnih preoblikovalnih hitrostih in temperaturi 550 °C

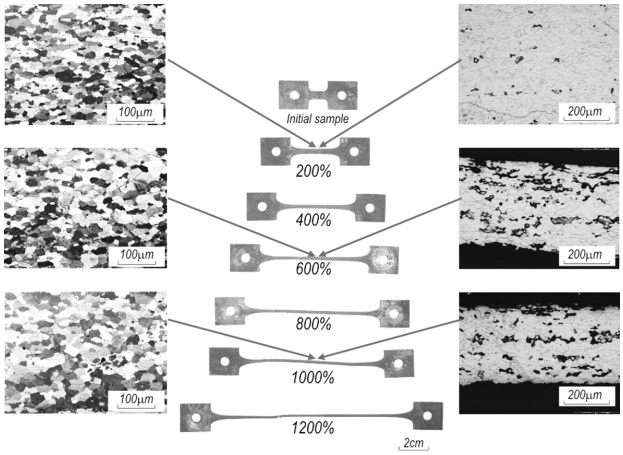

Figure 6: Samples after tensile testing at various elongations with microstructures and cavitations in the gauge length at 550 °C and 7.5 x 10^{-4} s^{-1}

Slika 6: Preizkušanci po nateznem preizkusu pri različnih raztezkih in posnetki mikrostruktur ter kavitacij v vzdolžnih prerezih merilnih dolžin pri 550 °C in 7,5 x 10^{-4} s^{-1}

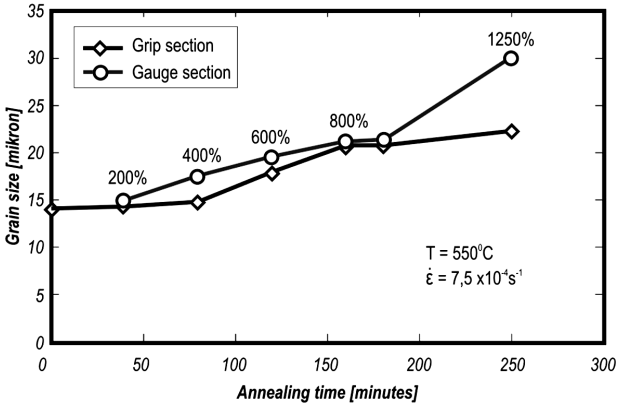

Figure 7: Static and dynamic grain growth in the longitudinal grip and gauge sections of the samples at an initial strain rate of 7.5 ×1 0^{-4} s^{-1} and at 550 °C

Slika 7: Statična in dinamična rast kristalnih zrn v vzdolžnih prerezih glav in merilnih dolžin preizkušancev pri začetni preoblikovalni hitrosti 7,5 × 10^{-4} s^{-1} in 550 °C

dynamic grain growth is, especially at longer pulling times (at elongations over 900 %), greater than the static one. The grains in the gauge section were slightly elongated with a grain aspect ratio of about 1.4, which remained nearly constant for all the elongations.

The cavitation that occurred during the superplastic forming in the gauge section was examined with the same samples and under the same testing conditions as shown in **Figure 6**. The fraction of cavitation increased with the increasing strain. However, the volume share of the cavitation did not exceed a value of 20 % at larger elongations up to 1200 %.

4 CONCLUSIONS

An Al-4Mg-0.6Mn-0.3Sc alloy sheet with a thickness of 1.4 mm produced with a simple thermomechanical treatment including hot and cold rolling, exhibited good superplastic properties, reflected in large elongations to failure, high strain-rate sensitivity indexes and low flow stresses. Elongations over 1000 % were achieved at initial strain rates up to 1 × 10^{-3} s^{-1} and temperatures higher than 530 °C (maximum elongation of 1455 % at 7.5 × 10^{-4} s^{-1} and 550 °C). The strain-rate sensitivity indexes varied with the strain rate and have the highest values within a narrow range of strain rates from 3 × 10^{-4} s^{-1} to 5 × 10^{-4} s^{-1}. The dynamic grain growth and the fraction of cavitation increase with the increasing strain. The Al-4.0Mg-0.6Mn-0.3Sc alloy sheet with a thickness of 1.4 mm, produced with a conventional rolling process, makes it possible to obtain a good, low-strain-rate superplasticity characterised by an elongation of over 1000 % at a temperature higher than 530 °C and a strain rate up to 1 × 10^{-3} s^{-1}.

This work was supported by Slovenian Research Agency (ARRS) of the Government of the Republic of Slovenia.

5 REFERENCES

[1] R. Grimes, M. J. Stowell, B. M. Watts, Metals Technology, 3 (**1976**), 154–160
[2] J. A. Wert, N. E. Paton, C. H. Hamilton, M. W. Mahoney, Metallurgical Transactions A, 12A (**1981**), 1267–1276
[3] R. Verma, P. A. Friedman, A. K. Ghosh, S. Kim, C. Kim, Metallurgical and Materials Transactions A, 27A (**1996**), 1889–1898
[4] T. G. Langdon, Metallurgical Transactions A, 13A (**1982**), 689–701
[5] K. A. Padmanabhan, R. A. Vasin, F. U. Enikeev, Superplastic flow: phenomenology and mechanics, Springer Verlag, Berlin, Heidelberg, New York, **2001**, 5–26
[6] I. C. Hsiao, J. C. Huang, Scripta Materialia, 40 (**1999**), 697–703
[7] T. G. Langdon, Materials Transactions, JIM, 40 (**1999**), 716–722
[8] K. Higashi, Materials Science and Technology, 16 (**2000**), 1320–1329
[9] T. G. Langdon, Journal of Materials Science, 42 (**2007**) 10, 3388–3397
[10] P. B. Berbon, S. Komura, A. Utsunomiya, Z. Horita, M. Furukawa, M. Nemoto, T. G. Langdon, Materials Transactions, JIM, 40 (**1999**)8, 772–778
[11] M. Furukawa, A. Utsunomiya, K. Matsubara, Z. Horita, T. G. Langdon, Acta Materialia, 49 (**2001**), 3829–3838
[12] R. Verma, S. Kim, Journal of Materials Engineering and Performance, 16 (**2007**)2, 185–191
[13] J. S. Vetrano, C. A. Lavender, C. H. Hamilton, M. T. Smith, S. M. Bruemmer, Scripta Metallugica et Materiala, 30 (**1994**), 565–575
[14] R. Verma, A. K. Ghosh, S. Kim, C. Kim, Materials Science and Engineering, A 191 (**1995**), 143–150
[15] P. A. Friedman, W. B. Copple, Journal of Materials Engineering and Performance, 13 (**2004**)3, 335–347
[16] R. R. Sawtell, G. L. Jensen, Metallurgical Transactions A, 21A (**1990**), 421–430
[17] T. G. Nieh, L. M. Hsiung, J. Wadsworth, R. Kaibyshev, Acta Materialia, 46 (**1998**), 2789–2800
[18] F. Musin, R. Kaibyshev, Y. Motohashi, G. Itoh, Metallurgical and Materials Transactions A, 35A (**2004**), 2383–2392
[19] Y. Peng, Z. Yin, B. Nie, L. Zhong, Transactions of Nonferrous Metals Society of China, 17 (**2007**), 744–750
[20] T. Sakuma K. Higashy, Materials Transactions JIM, 40 (**1999**), 702–715

UDK 621.762.5:620.18
Original scientific article/Izvirni znanstveni članek

ISSN 1580-2949
MTAEC9, 43(6)303(2009)

WEAR RESISTANCE OF CHROMIUM PRE-ALLOYED SINTERED STEELS

OBRABNA OBSTOJNOST KROMOVIH SINTRANIH JEKEL

Róbert Bidulský[1], Marco Actis Grande[1], Jana Bidulská[2], Tibor Kvačkaj[2]

[1]Politecnico di Torino – Alessandria Campus, Viale T. Michel 5, 15100 Alessandria, Italy
[2]Department of Metal Forming, Faculty of Metallurgy, Technical University of Košice, Vysokoškolská 4, 042 00 Košice, Slovakia
tibor.kvackaj@tuke.sk

Prejem rokopisa – received: 2009-05-04; sprejem za objavo – accepted for publication: 2009-06-19

This paper deals with the influence of the processing conditions on the material properties and wear characteristics of chromium pre-alloyed sintered steels. Three different processing conditions were used, involving different cooling rates from the sintering temperatures of 1180 °C and 1240 °C. A conventional (slow) cooling condition and a new progressive condition, sinter hardening, were examined. The results showed that the typical microstructure characteristics of sintered steels represent an important parameter affecting their wear behaviour.

Key words: pre-alloyed sintered steel, sinter hardening, sliding wear, porosity, microstructure

V članku je predstavljen vpliv pogojev procesiranja na mehanske lastnosti in obrabne značilnosti kromovih sintranih jekel. Uporabljeni so bili trije različni pogoji procesiranja z različno hitrostjo ohlajanja s temperatur 1180 °C in 1240 °C. Opredeljena sta vpliv počasnega (konvencionalnega) ohlajanja in naprednega kaljenja sintra. Rezultati so pokazali, da so za vedenje pri obrabi pomembne značilnosti mikrostrukture sintranih jekel.

Ključne besede: sintrano jeklo, kaljenje sintra, drsna obraba, poroznost, mikrostruktura

1 INTRODUCTION

Powder metallurgy (PM) is a well-established processing route for the production of near-net-shape components of complex geometry. The traditional uniaxial powder consolidation process is still widely employed for the production of ferrous parts, especially for the automotive industry. In this field the typical components (i.e., gears, cams) face working conditions giving rise to sliding, rolling or abrasion. Therefore, an understanding of the wear phenomena and characteristics is very important.

The dry sliding behaviours of sintered ferrous alloys have been investigated in several previous studies [1,2,3,4,5,6], which indicated that the wear mechanisms are similar to wrought materials under the same conditions. Nevertheless, sintered materials contain a variable quantity of pores, as well as (eventually) heterogeneous microstructures, which create peculiar wear characteristics for PM products. As a matter of fact, pores represent the first sites for microplastic deformation and they are potential sites for the formation of the first microcracks[7,8,9].

The use of chromium in PM may create some difficulties in reducing the oxides present at the surface and acting as a barrier to interparticle diffusion; nevertheless, chromium is a widely used hardening element in ferrous sintered products[10,11,12,13]. Molybdenum is also commonly used in low-alloy PM steels because of the easily reducible oxides. Chromium and molybdenum are very effective in promoting increased strength and toughness.

Sinter hardening requires controlled cooling after sintering in the austenite range (1120–1240 °C). A new approach to sinter hardening has been proposed using vacuum furnaces[14,15,16]. They show enhanced cooling capabilities, with several advantages related to cost effectiveness, reducing the problems of oil entrapment and distortion, determining the improved dimensional stability and consequently higher yield and quality of the production lots. Moreover, vacuum furnaces may reduce the decarburation typical of continuous furnaces and can be programmed to perform quenching and tempering integrated in the same cycle, thus reducing the internal stresses that cause excessive notch sensitivity and brittleness[17,18].

The main aim of this paper is to show the influence of various sintering conditions on the wear resistance of chromium pre-alloyed sintered steels.

2 MATERIAL AND EXPERIMENTAL PROCEDURE

The investigated chromium pre-alloyed system was Fe + 1.5 % Cr + 0.65 % C + 0.6 % AW. The powders were homogenised in a Turbula mixer. Specimens with a green density of ≈ 7.0 g cm^{-3} were obtained using a 2000 kN hydraulic press, in a disc-shaped mould (= 40 mm) applying a pressure of 600 MPa. The sintering was carried out in a TAV vacuum furnace with argon back-filling at 1180 °C and 1240 °C for 1 h. The cooling rate was 0.05 °C/s, while the rapid cooling rate (sinter

hardening) was 6 °C/s (**Table 1**). The densities were evaluated using the water-displacement method.

Table 1: Sintering conditions of the chromium pre-alloyed sintered steels
Tabela 1: Pogoji sintranja jekel

Alloy No	Sintering conditions
A	Temperature: 1180 °C; time: 1 h; cooling condition: 0.05 °C/s
B	Temperature: 1180 °C; time: 1 h; cooling condition: 6 °C/s (sinter hardening)
C	Temperature: 1240 °C; time: 1 h; cooling condition: 6 °C/s (sinter hardening)

The wear tests were carried out using a pin-on-disc apparatus. The disc was made of the investigated material. As a counter face, a WC-Co pin was used, having a rounded shape on top with a diameter of 3 mm. The counter-pin was changed after the end of each test, in order to preserve the roundness of its top. All the wear tests were performed in air and without any lubricant. The applied loads were 25 N, and the rotation speed of the disc was 140 r/min. The distances of the pin position from the disc centre were 34 mm. Prior to testing, the surface was polished with abrasive papers in order to determine a medium surface roughness equal to (or less than) 0.8 μm, as specified in the ASTM G99–95a. Each test was interrupted after (300, 600, 900, 1200 and 2000) m of sliding distance and the discs were weighed using a precision balance with a sensitivity of 10^{-5} to determine the evolution of the wear during each test.

The wear characterization of the chromium pre-alloyed sintered steels was carried out with optical microscopy, also determining the volume mass and the interconnected (open) porosity (according to UNI 7825). Wear-track observations were carried out using an SEM JEOL 7000F. Vickers hardness measurements were performed on cross-sections of the samples and the impact-testing procedure using Charpy tests was carried out on un-notched samples.

3 EXPERIMENTAL RESULTS AND DISCUSSION

3.1 Microstructures

The microstructure of the chromium pre-alloyed sintered specimens (A in **Table 1**) consisted predominantly of a pearlite microstructure ($HV_{0.010} \approx 240$) with small areas of ferrite ($HV_{0.010}$ = 125–140), **Figure 1**. The system B determines the dominant bainite (formed by a mixture of upper ($HV_{0.010}$ = 330–370) and lower ($HV_{0.010}$ = 260–285 bainite), with some martensite ($HV_{0.010}$ = 580–648), **Figure 2**. Increasing the sintering temperature to 1240 °C (system C) resulted in the formation of a dominant martensitic microstructure ($HV_{0.010}$ = 580–692) with small, upper bainite networks ($HV_{0.010} \approx 415$), **Figure 3**. Different cooling rates did not result, in terms of hardness, in a large difference between systems sintered at 1180 °C. On the contrary, using a higher sintering temperature (1240 °C/s) resulted in harder microstructure constituents with a dominant martensitic microstructure.

3.2 Friction coefficient

Figure 4 shows a plot of the values of the steady-state friction coefficient measured for the chromium pre-alloyed sintered steels tested under different conditions. The values ranged from about 0.90 to 0.82, gradually decreasing as the sliding distance was increased. Higher values of the coefficient of friction were generally measured for samples with higher porosity lev-

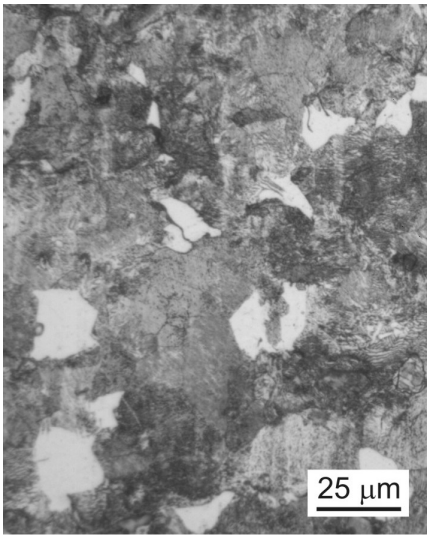

Figure 1: Microstructure of A steel, 1180 °C / 1 h; cooling rate 0.05 °C/s
Slika 1: Mikrostruktura jekla A, 1180 °C/1h, hitrost ohlajanja 0,05 °C/s

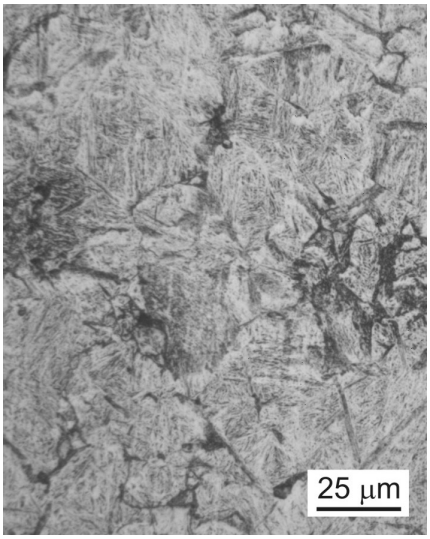

Figure 2: Microstructure of B steel, 1180 °C / 1 h; sinter hardening, cooling rate 6 °C/s
Slika 2: Mikrostruktura jekla A, 1180 °C/1h, kaljeno, hitrost ohlajanja 6 °C/s

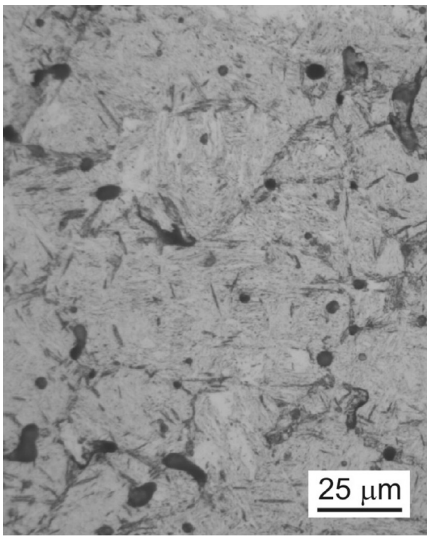

Figure 3: Microstructure of C steel, 1240 °C / 1 h; sinter hardening, cooling rate 6 °C/s
Slika 3: Mikrostruktura jekla A, 1240 °C/1h, kaljeno, hitrost ohlajanja 6 °C/s

els (specimens sintered at 1180 °C), as a cumulative effect of a higher resistance to plastic flow and a slightly greater contact area. The present results of the friction coefficient ranged from 0.7 to 0.9, in accordance with the literature data for sintered materials in the untreated condition[19].

3.3 Wear characteristics

The mass losses were expressed as material removal during the test and were recorded as a function of the sliding distance. The wear of PM materials is more complicated than that of wrought steels and depends on different factors related to the sintered microstructures (such as plasticity and strength) of the different phases, as well as the porosity. Hence, the evaluation of the wear resistance (as the reciprocal value of the amount of wear)

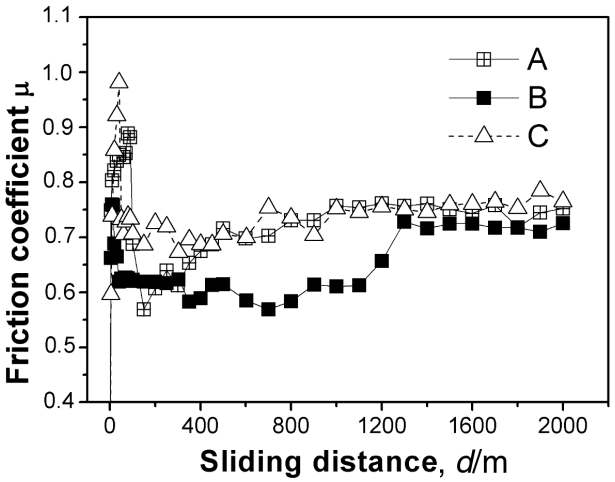

Figure 4: Friction coefficient of investigated materials
Slika 4: Koeficienti trenja za preiskane materiale

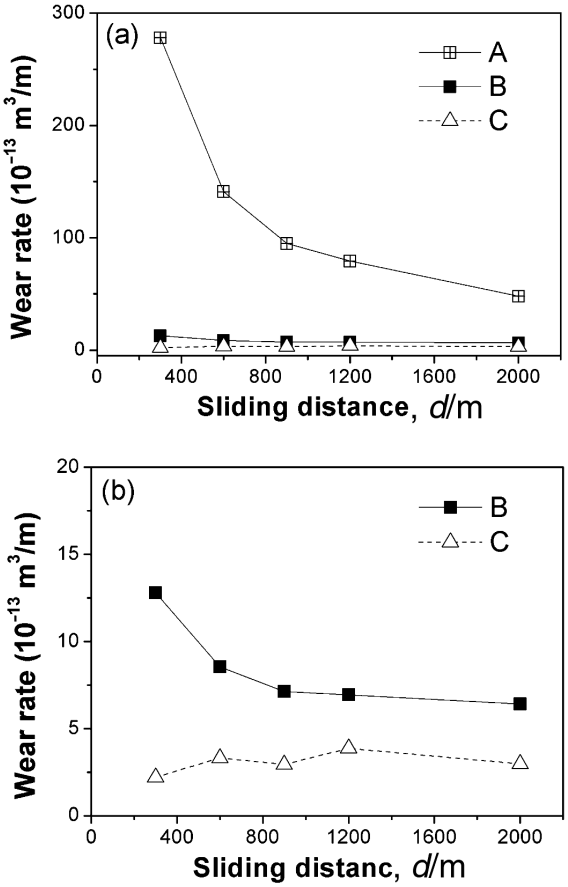

Figure 5: (a) Wear rates for investigated specimens. (b) Wear rates for specimens cooled with greater cooling rate
Slika 5: (a) Hitrosti obrabe za preizkušance, (b) hitrosti obrabe za preizkušance, ohlajene z večjo hitrostjo

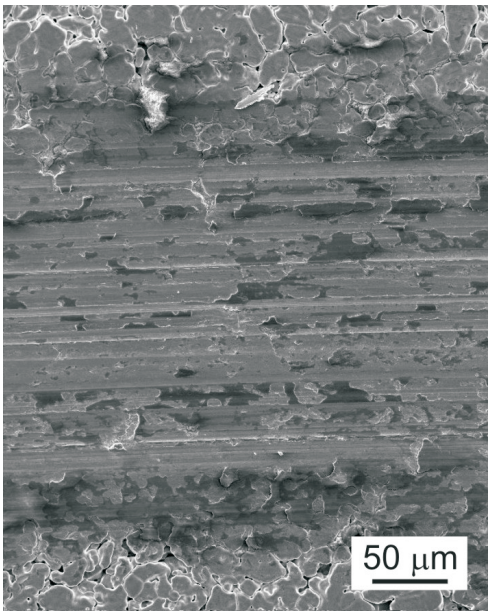

Figure 6: Typical, mild oxidative wear regime, which was observed for all tested specimens, specimen C; 1240 °C / 1 h; sinter hardening, cooling rate 6 °C/s
Slika 6: Rahlo oksidativen režim obrabe značilen za vse preizkušance, preizkušanec C, 1240 °C/ 1h, kaljeno, hitrost ohlajanja 6 °C/s

Table 2: Material properties of the tested alloys
Tabela 2: Materialne lastnosti raziskanih zlitin

Alloy No	ρ_P*	ρ_S*	P_{Total}	*TRS*	*UTS*	*IE*	Hardness *HRA*	Microhardness range; average $HV_{0.010}$
	g/cm^3	g/cm^3	%	MPa	MPa	MPa		
A	6.987	7.002	8.64	893	447	22.86	46.45 ± 0.15	(125–240); 189
B	6.983	6.973	9.01	1335	1035	13.29	63.70 ± 3.60	(260–648); 520
C	7.002	7.113	7.19	1421	1217	10.60	65.55 ± 0.65	(414–692); 589

*P-Pressing, *S-Sintering

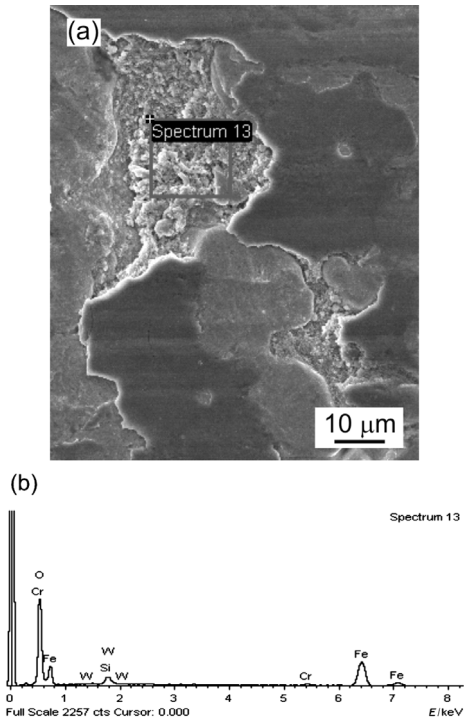

Figure 7: (a) Oxide layers on the chromium pre-alloyed sintered steels (scanning microscopy) and (b) EDX spectra of oxide layers
Slika 7: (a) Oksidna plast na sintranem kromovem jeklu (vrstični mikroskop) in (b) EDX-spektri oksidne plasti

is better expressed in terms of wear rate. The wear rate was calculated using the equation:

$$W_s = \frac{\Delta m}{\rho \cdot L \cdot F_N} \quad (1)$$

where:
W_s is the wear rate [m^3/(N m)],
Δm is the mass loss of the test samples during the wear test [g],
ρ is the density of the test materials [g/cm^3],
L is the total sliding distance [m],
F_N is the normal force on the pin [N].

The wear rates for the investigated specimens are shown in **Figure 5**. The results show that the wear resistances of chromium pre-alloyed sintered steels using higher temperatures and cooling rates (sinter hardening) were improved due to the shift of the ferrite-bainite to the dominant martensitic microstructure.

Useful information on the wear mechanisms of the sintered steels was obtained by SEM observations. The investigation demonstrated the mechanism of delamination: deformed layers and tracks along the direction of sliding during the wear. Plastic deformation took place on the wear surfaces during the wear tests. The contact

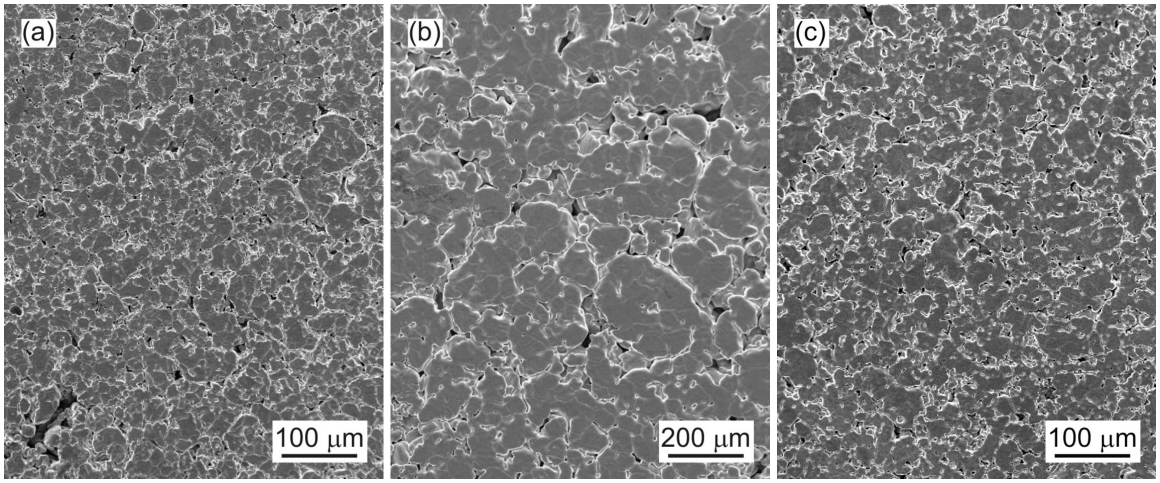

Figure 8: (a) Microstructural discontinuities as pore agglomerates with sharp edges, A specimens. (b) Microstructural discontinuities as pore agglomerates with slightly sharp edges, B specimens. (c) Rounded pores, C specimens.
Slika 8: (a) Diskontinuitete mikrostrukture kot aglomerati por z ostrimi oblikami, preizkušanci A, (b) diskontinuitete mikrostrukture kot aglomerati por z rahlo izostreno obliko, preiskušanci B, (c) zaobljene pore, preizkušanci C

pressure of the wear surfaces increased with the increasing amount of porosity in accordance with [20].

The sliding tests carried out on samples sintered at 1180 °C and cooled at 0.05 °C/s were, in any case, typical of a mild oxidative wear regime, **Figure 6**. Detailed analyses revealed (**Figure 7 (a)** and (**b**)) oxide layers on the chromium pre-alloyed sintered steels in accordance with the literature data[14,15,16]. Therefore, delamination and oxidation wear seems to be the main wear mechanisms.

3.4 Material properties

The sintered material characteristics of a given alloy (i.e., its porosity content and microstructure) also influence the charpy impact energy, as shown by the values reported in **Table 2**. The important parameters that specify the role of porosity are the amount of porosity and the pore size. Earlier studies[1,4,6] have suggested that an amount of porosity higher than 10 % and a pore size that is larger than 12 μm constitute a dominant interconnected porosity. These pores are filled with debris particles during wear. This may enhance the wear resistance of the samples by increasing the real contact area and decreasing the contact pressure. A dominant role can be played by isolated pores and their shapes. Sharp-edged pores can give rise to considerable stress-concentration effects that favour the nucleation and propagation of microcracks, leading to the easier formation of wear fragments. This interpretation is underlined by the lower Charpy impact values measured for the specimens with a higher porosity content, along with the results at the higher sintering temperature of 1240 °C that reduced the negative effects of the porosity by means of roundness, so promoting an increase of the wear resistance. Specimens sintered at a sintering temperature of 1240 °C (HS) present more rounded pores than those sintered at a lower temperature, **Figure 8 (a)-(c)**, along with higher impact energies. The lowest impact values were shown by the specimens sintered at the lower temperature and then slow cooled. The increase in the sintering temperature and cooling rates strongly influenced the microstructure and hardness to the shifting of the microstructures from pearlite to dominant martensite microstructures. Sinter hardening increases the martensite content in the microstructure and this results in a further increase in the strength with a decrease of the ductility and toughness (the plasticity properties represent the impact-energy values). The results suggested that sinter hardening can have a practical interest in view of components where wear resistance can play a decisive role.

4 CONCLUSIONS

The main results obtained in this paper may be summarised as follows:

- A higher cooling rate (sinter hardening), supporting a bainite-martensitic microstructure, and a higher sintering temperature increase both the strength and ductility,
- delamination and oxidation are the main wear mechanisms,
- microstructure and hardness represent the dominant effect influencing the mechanical properties as well as the wear resistance,
- higher temperature sintering (1240 °C) reduces the negative effects of porosity due to the evident effect of pore roundness, if compared to a lower sintering temperature and cooling rates.

Acknowledgment

R. Bidulský thanks the Politecnico di Torino and the Regione Piemonte for co-funding of a fellowship. This work was supported by the VEGA No. 1/4136/07.

5 REFERENCES

[1] Dubrujeaud B., Vardavoulias M., Jeandin M.: Wear, 174 (**1994**), 155–161
[2] Wang J., Danninger H.: Wear, 222 (**1998**), 49–56
[3] Molinari A., Straffelini G.: Wear, 181–183 (**1995**), 334–341
[4] Straffelini G., Molinari A.: Powder Metall., 44 (**2001**), 248–252
[5] Khorsand H., Habibi S. M., Yoozbashizadea H., Janghorban K., Reihani S. M. S., Rahmani Seraji H.: Mater. Design, 23 (**2002**), 667–670
[6] Simchi A., Danninger H.: Powder Metall., 47 (**2004**), 73–80
[7] Hadrboletz A., Weiss B.: Int. Mater. Reviews, 42 (**1997**), 1–44
[8] Dudrová E., Kabátová M., Bidulský R.: Fractography of Sintered Iron and Steels: A Review. RoPM 2005. Cluj-Napoca, Romania, 1 (**2005**), 101–113
[9] Dudrová E., Kabátová M.: Fractography of Sintered Steels: A Review. Proc. PM World Congress, Vienna, Austria, EPMA, Shrewsbury, 3 (**2004**), 193–198
[10] Bidulský R., Actis Grande M.: High Temp. Mater. Process., 27 (**2008**), 249–256)
[11] Karlsson H., Nyborg L., Bergman O.: Surface Interactions during Sintering of Water atomised Pre-alloyed Steel Powder. Proc. PM World Congress, Vienna, Austria, EPMA, Shrewsbury, 3 (**2004**), 24–29
[12] Karlsson H., Nyborg L., Berg S.: Powder Metall., 48 (**2005**), 51–58
[13] Hryha E., Cajková L., Dudrová E.: Powder Metall. Prog., 7 (**2007**), 181–197
[14] Blais C., Serafini R.E., L'Esperance G.: Int. J. Powder Metall., 41 (**2005**), 33–41
[15] Actis Grande M., Bidulský R., Dudrová E., Kabátová M., Rosso M.: Powder Metal. Prog., 8 (**2008**), 101–108
[16] Zendron M., Girardini L., Molinari A.: Powder Metall., 51 (**2008**), 237–244
[17] Ceniga L.: J. Therm. Stresses, 31 (**2008**), 728–758
[18] Ceniga L.: J. Therm. Stresses, 31 (**2008**), 862–891
[19] Candela N., Plaza R., Rosso M., Velasco F., Torralba J. M.: J. Mater. Proc. Technol., 119 (**2001**), 7–13
[20] Gulsoy H. O., Bilici M. K., Bozkurt Y., Salman S.: Mater. Design, 28 (**2007**), 2255–2259

UDK 669.018:621.762.5:620.17/.18
Original scientific article/Izvirni znanstveni članek

ISSN 1580-2949
MTAEC9, 43(6)309(2009)

PREPARATION AND TESTING OF PROTOTYPE Mg_2Si-Mg-TiC AND Mg_2Si-TiC/TiB_2 COMPOSITES

PRIPRAVA IN PREIZKUŠANJE PROTOTIPNIH KOMPOZITOV Mg_2Si-Mg-TiC/TiB_2 IN Mg_2Si-TiC/TiB_2

Varužan Kevorkijan[1], Srečo Davor Škapin[2]

[1]Independent Researching plc, Betnavska cesta 6, 2000 Maribor, Slovenia
[2]Institut »Jožef Stefan«, Jamova 39, 1000 Ljubljana, Slovenia
varuzan.kevorkijan@siol.si

Prejem rokopisa – received: 2009-05-25; sprejem za objavo – accepted for publication: 2009-07-07

In this work, the preparation of various light weight Mg-Mg_2Si–TiC metal matrix composites and Mg_2Si–TiC/TiB_2 ceramic composites has been described and the influence of their structure on mechanical response was discussed.
Mg-Mg_2Si-TiC composites with continuous magnesium matrix densified to >95 % T.D. were fabricated by pressureless reactive infiltration of performs made from Mg_2Si and TiC powders. Infiltration was performed in an argon atmosphere at temperatures 700, 800 and 900 °C for 1 h. Trials made with Mg_2Si preforms reinforced with TiB_2 were unsuccessful.
Mg_2Si–TiC/TiB_2 ceramic composites densified to >97 % T.D. were prepared by pressureless reactive sintering of tablets made from Mg_2Si and TiC or TiB_2 powders. The reactive sintering was performed at 1020 °C for 0.5–1 h under a protective argon atmosphere.
The phases present in the obtained composite samples have been identified by scanning electron microscopy/energy dispersive X-ray spectroscopy. In addition, room temperature tensile tests (R_m, $R_{p0.2}$, A) and hardness measurements (*HV*) were also undertaken.
The results have shown that Mg-Mg_2Si–TiC composites are with tensile properties superior to that of conventional magnesium alloys while Mg_2Si–TiC/TiB_2 samples combined high hardness (9–10 GPa) and low density (2.2. –2.5 g/cm^3).

Key words: Mg-Mg_2Si–TiC and Mg_2Si–TiC/TiB_2 composites, reactive pressureless infiltration, reactive pressureless sintering, microstructural examination, tensile test, advanced, low-weight engineering materials

V delu opisujemo pripravo lahkih kompozitov Mg-Mg_2Si-TiC s kovinsko matrico in keramične kompozite Mg_2Si-TiC/TiB_2 ter preučevanje vpliva njihove strukture na mehanske lastnosti.
Kompozite Mg-Mg_2Si-TiC s kontinuirno matrico iz magnezija, zgoščene do >95 % T.G., smo izdelali po postopku reakcijske infiltracije pri atmosferskem tlaku predoblik, stisnjenih iz prahov Mg_2Si in TiC. Inflitracija je potekala v atmosferi argona, 1h pri temperaturah (700, 800 in 900) °C. Poskusi infiltracije predoblik Mg_2Si, ojačenih s TiB_2 niso bili uspešni.
Keramične kompozite Mg_2Si–TiC/TiB_2, zgoščene do >97 % T.G., smo izdelali z reakcijskim sintranjem pri atmosferskem tlaku tablet, stisnjenih iz prahov Mg_2Si in TiC ali TiB_2. Vzorce smo reakcijsko sintrali pri 1020 °C 1h v zaščitni atmosferi argona.
Mikrostrukturo in fazno sestavo pripravljenih vzorcev smo analizirali z vrstičnim elektronskim mikroskopom in XRD. Mehanske preiskave: natezni preizkus (R_m, $R_{p0.2}$, A) in merjenje trdot (*HV*) smo izvajali s standardnimi metodami pri sobni temperaturi.
Rezultati nateznega preizkusa so pokazali, da imajo kompoziti Mg-Mg_2Si–TiC veliko boljše mehanske lastnosti kot navadne magnezijeve zlitine, medtem ko vzorci Mg_2Si–TiC/TiB_2 združujejo visoko trdoto (9–10 GPa) in nizko specifično maso (2.2.–2.5 g/cm^3).

Ključne besede: kompoziti Mg-Mg_2Si–TiC in Mg_2Si–TiC/TiB_2, reakcijska infiltracija pri atmosferskem tlaku, reakcijsko sintranje pri atmosferskem tlaku, preiskave mikrostrukture, mehanske preiskave, lahki inženirski materiali prihodnosti

1 INTRODUCTION

Magnesium alloys and Mg-based composites are prospective candidates for light-weight structural materials [1–2]. However, most Mg alloys are of limited use in high performance applications due to their low mechanical properties [3]. Improvement of their mechanical properties could be achieved by reinforcement with different ceramic particulates, which has already been well demonstrated [4,5], or by applying new magnesium-based compounds (such as Mg_2Si) as the matrix constituent [6]. Among these, magnesium silicide (Mg_2Si) is particularly attractive because of its superior characteristics such as high melting point (1085 °C), low density (1.99 g/cm^3), high hardness (350–700 *HV*) and elastic modulus (120 GPa) [7].

On the other hand, the major disadvantage of Mg_2Si is its brittleness [8–9], limiting the usage of bulk (sintered or hot pressed) Mg_2Si as a structural material in engineering applications. A possible solution considered in this work is the formulation of ultra-light composite materials with a Mg_2Si-Mg matrix reinforced with ceramic particulates (TiC, TiB_2, B_4C) in order to achieve an improvement in mechanical properties and brittleness.

2 EXPERIMENTAL

In the first set of experiments, Mg_2Si-Mg-TiB_2 and Mg_2Si-Mg-TiC composite samples were fabricated by pressureless infiltration of porous preforms with molten magnesium. Preforms were isostatically pressed from the various mixtures of commercial Mg_2Si (99.5 %, 30 μm)

and TiC (99.5 %, 30 μm) or TiB_2 (99.5 %, 30 μm) powders, as listed in **Table 1**. Samples were cylinders 30 mm high and 20 mm in diameter. Infiltration was performed in a vacuum furnace in an argon atmosphere at temperatures of (700, 800 and 900) °C for 1 h.

Table 1: The volume fractions of various Mg_2Si-TiC and Mg_2Si-TiB_2 mixtures used for preforms in infiltration, and tablets in sintering experiments

Tabela 1: Sestava različnih zmesi Mg_2Si-TiC in Mg_2Si-TiB_2 v volumenskih deležih (*f*/%), uporabljenih za izdelavo predoblik za infiltracijo in tablet za sintranje

Mixture	Composition, *f*/%		
	Mg_2Si	TiC	TiB_2
A	90	10	–
B	80	20	–
C	90	–	10
D	80	–	20

In the second set of experiments, composite samples were prepared by pressureless sintering of isostatically pressed tablets made from the same Mg_2Si-TiC and Mg_2Si-TiB_2 mixtures listed in **Table 1**. Sintering was performed at 1020 °C, for 0.5–1 h in a protective argon atmosphere.

The as-synthesized composite samples were cut, machined and polished in accordance with standard procedures.

Microstructural characterization of fabricated composites was performed by optical and scanning electron microscopy (OM and SEM), whereas X-ray diffraction (XRD) measurements were applied to the samples to identify the phases and their crystal structure.

Quantitative determination of the volume percentage of Mg_2Si, secondary phases and ceramic particles in the matrix, as well as the retained porosity, was performed by analysing the optical and scanning electron micrographs of as polished composite bars using the point counting method and image analysis and processing software.

Composite density measurements were carried out in accordance with Archimedes' principle, applying distilled water as the immersion fluid.

The initial density of the green compacts (preforms and tablets) was calculated from the mass and geometry of the samples.

Tensile tests were conducted on cylindrical tension-test specimens 5 mm in diameter and 25 mm gauge length using an automated servo-hydraulic tensile testing machine with a crosshead speed of 0.254 mm/60 s.

Vickers hardness (*HV*) measurements were performed at room temperature on polished composite samples as an average of 15 indentations. These measurements were made on an automatic digital tester using a pyramidal diamond indenter with a facing angle of 136° a 0.025 kg indenting load, 50 μm/s load applying speed, and a 15 s load holding time.

3 RESULTS AND DISCUSSION

Composites made by pressureless infiltration

The calculated porosity of the preforms used was within the range of (30–35 ± 5) %. Based on the experimental findings, the pressureless infiltration of Mg_2Si-TiC preforms with molten magnesium did not occur below 900 °C. At 900 °C, the infiltration was complete within 1h, resulting in composite samples with less than 5 % of retained porosity. At the same time, under the applied experimental conditions, the pressureless infiltration of Mg_2Si-TiB_2 preforms was unsuccessful.

The microstructure and phase composition of the composite samples obtained is presented in **Figure 1 a, b, c**.

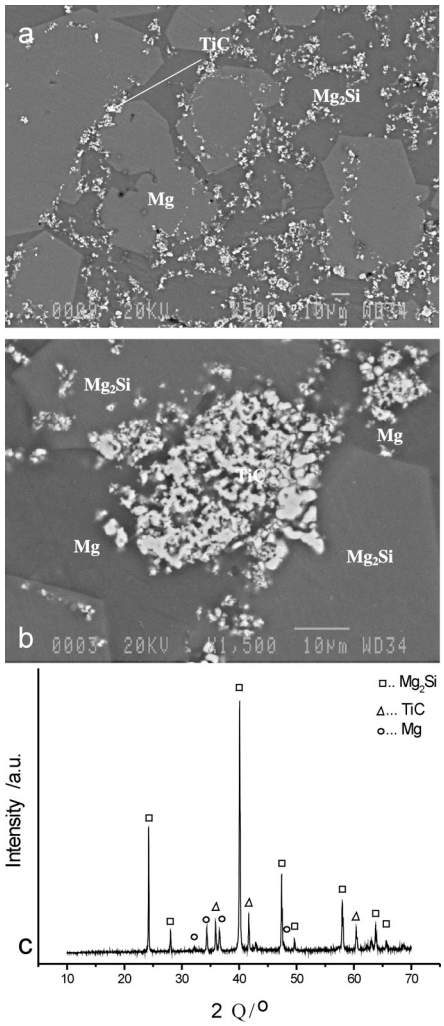

Figure 1: (a, b) SEM micrograph of a pressurelessly infiltrated preform with the initial composition of the preform skeleton of the volume fraction of 70 % Mg_2Si-20 % TiC and an initial porosity of (30 ± 5) %. The phases detected are Mg, Mg_2Si and TiC; (c) XRD of the sample shown in the **Figure 1a-c**.

Slika 1: (a, b) SEM posnetek mikrostrukture pri atmosferskem tlaku infiltrirane predoblike začetne sestave v volumenskih deležih 70 % Mg_2Si-20 % TiC ter začetne poroznosti (30 ± 5) %. Ugotovljene faze so: Mg, Mg_2Si in TiC; (c) XRD vzorcev, prikazanih na sliki 1 a–c.

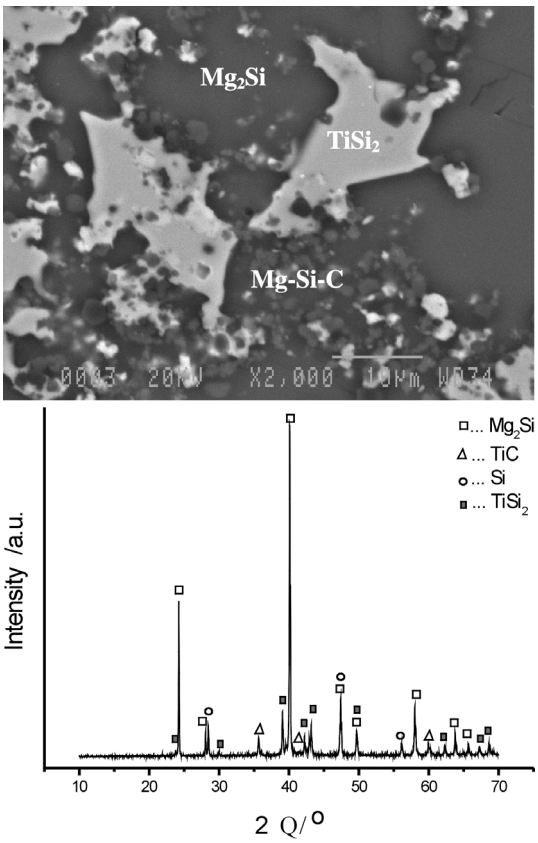

Figure 2: (a) SEM micrograph of pressurelessly sintered composite simple with the inital volume composition 90 % Mg_2Si and 10 % TiC, (b) XRD of the sample

Slika 2: (a) SEM-posnetek mikrostrukture vzorcev kompozitov začetne volumenske sestave 90 % Mg_2Si in 10 % TiC, sintranih pri atmosferskem tlaku, (b) XRD vzorca

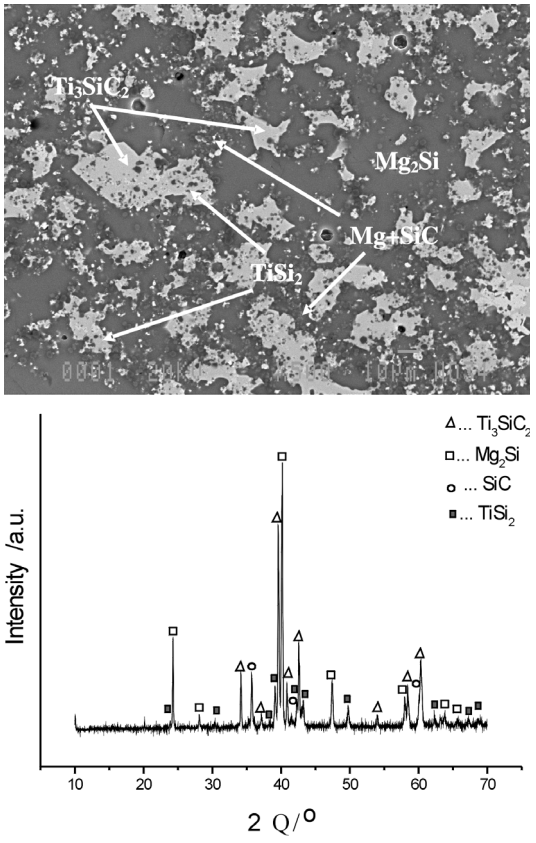

Figure 3: (a) SEM micrograph of pressureless sintered composite sample with the initial volume composition 80 % Mg_2Si and 20 % TiC, (b) XRD of the sample

Slika 3: (a) SEM-posnetek mikrostrukture vzorca kompozita začetne volumenske sestave 80 % Mg_2Si in 20 % TiC, (b) XRD vzorca

Table 2: Average room temperature tensile properties and Vickers hardness of pressurelessly infiltrated composite samples

Tabela 2: Povprečne vrednosti nateznih lastnosti in Vickersove trdote, izmerjenih pri sobni temperaturi, pri vzorcih kompozita, infiltriranih pri atmosferskem tlaku

Composite initial composition *fi*/%	Retained porosity (%)	Density ρ/(g/cm^3)	*E*/ (GPa)	Tensile strength σ/MPa	Vickers Hardness *HV*/GPa
63%Mg_2Si+30%Mg+7%TiC	3.6 ± 0.4	2.03 ± 0.1	88 ± 9	186 ± 19	4.9 ± 0.5
56%Mg_2Si+30%Mg+14%TiC	4.7 ± 0.5	2.32 ± 0.1	97 ± 10	197 ± 20	5.1 ± 0.5

Table 3: Average room temperature tensile properties and Vickers hardness of pressureless sintered composite samples

Tabela 3: Povprečne vrednosti nateznih lastnosti in Vickersove trdote, izmerjenih pri sobni temperaturi, pri vzorcih kompozita, sintranih pri atmosferskem tlaku

Iinitial composition *fi*/%	Retained porosity (%)	Density ρ/(g/cm^3)	*E*/ (GPa)	Tensile strength σ/MPa	Vickers Hardness *HV*/GPa
Mg_2Si+10%TiC	1.8 ± 0.2	2.25 ± 0.1	132 ± 13	487 ± 49	9.1 ± 1
Mg_2Si+20%TiC	2.2 ± 0.2	2.53 ± 0.1	141 ± 14	532 ± 53	9.9 ± 1
Mg_2Si+10%TiB_2	2.3 ± 0.2	2.22 ± 0.1	134 ± 13	477 ± 48	9.6 ± 1
Mg_2Si+20%TiB_2	2.9 ± 0.3	2.43 ± 0.2	146 ± 15	528 ± 53	10.3 ± 1

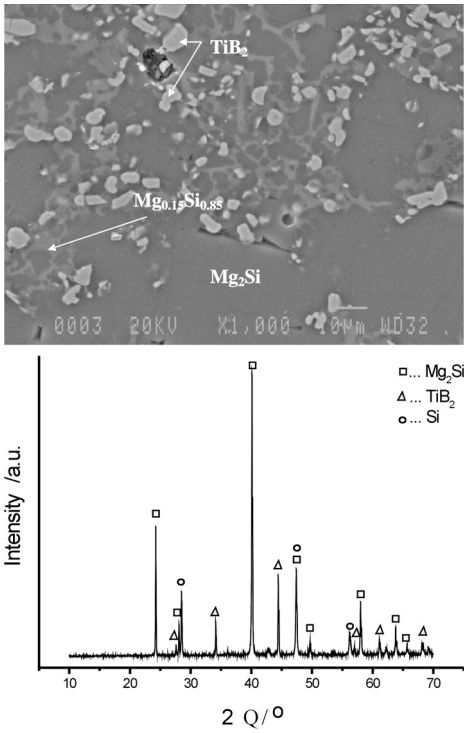

Figure 4: (a) Microstructure of pressurelessly sintered composite sample with the inital volume composition 90 % Mg_2Si and 10 % TiB_2, (b) XRD of the sample

Slika 4: (a) Mikrostruktura vzorce kompozitov začetne volumenske sestave 90 % Mg_2Si in 10 % TiB_2, sintranih pri atmosferskem tlaku, (b) XRD vzorca

Large block-shaped Mg_2Si particles of about 50 μm in size can be observed. The distribution of Mg_2Si particles is in principle homogeneous with no agglomeration. The Mg matrix is continuous with dispersed fine TiC particles.

Composites made by pressureless sintering

Pressureless sintering at 1020 °C for 1 h of Mg_2Si-TiC and Mg_2Si-TiB_2 samples made from mixtures A, B, C and D (**Table 1**) resulted in almost fully dense composite species with a retained porosity of less than 3 %.

The microstructure of the composite samples obtained is presented in **Figures 2, 3 and 4**.

As illustrated in **Figure 2**, in pressureles sintered samples with the initial volume composition 90 % Mg_2Si and 10 % TiC, the ceramic reinforcement reacted with Mg_2Si transforming completely the initial TiC aggregates to dense $TiSi_2$ secondary grains. According to the X-ray diffraction patterns (**Figure 2 b**) of pressureless sintered Mg_2Si samples with 10 % of TiC reinforcement, the main product of chemical reaction between Mg_2Si and TiC is $TiSi_2$. The presence of elemental silicon was also confirmed, while magnesium and carbon did not detected by XRD, Reaction 1:

$$3Mg_2Si + TiC = TiSi_2 + Si + 6Mg + C \quad (1)$$

The additional SEM investigation confirmed the presence of Mg-Si-C precipitates, most probably formed by further chemical reactions between elemental silicon, magnesium and carbon.

However, by increasing the amount of TiC reinforcement to 20 %, the reaction path was changed resulting in the formation of Ti_3SiC_2, $TiSi_2$ and SiC phases, **Figure 3a, b**, as well as the elemental magnesium, Reaction 2:

$$7Mg_2Si + 4TiC = Ti_3SiC_2 + TiSi_2 + 14Mg + 4SiC \quad (2)$$

In pressurelessly sintered composite samples reinforced with TiB_2 particles large chunky Mg_2Si particles were detected, **Figure 4**. During reactive pressureless sintering, these Mg_2Si particles melt incongruently, forming a peritectic. Further densification of the samples proceeds via pressureless reactive liquid sintering. On cooling the samples, the molten phase crystallizes in the form of a continuous lace network with an average composition of $Mg_{0.15}Si_{0.85}$, with dispersed, fine TiB_2, **Figure 4 a**.

4 CONCLUSION

The effect of fabrication techniques (reactive infiltration or pressureless reactive sintering) and processing conditions on the phase formation, microstructures and mechanical properties of Mg_2Si-TiC and Mg_2Si-TiB_2 composites was examined.

It was found that pressureless reactive infiltration is effective in production of Mg_2Si-Mg-TiC composites, whereas in the case of Mg_2Si-Mg-TiB_2 samples, it was unsuccessful. The composite samples obtained by pressureless reactive infiltration of molten magnesium into a porous preform of Mg_2Si with TiC ceramic reinforcement were designed to consist of a continuous magnesium matrix discontinuously reinforced with Mg_2Si and TiC. Such a design was selected in order to reduce the well known brittleness of the Mg_2Si phase, thereby creating an ultra-light structural material with excellent tensile properties.

On the other hand, pressurelessly reactive sintered Mg_2Si-TiC and Mg_2Si-TiB_2 composites were designed to provide the improved hardness (9–10 GPa).

Although further experimental work is necessary to identify the real mechanism of pressureless densification of Mg_2Si-TiC and Mg_2Si-TiB_2 samples as well as the mechanical response of reinforced samples, the results obtained clearly demonstrate that routinely performed pressureless densification resulted in samples with almost theoretical density, proving at the same time the great industrial potential of this low-cost and highly productive fabrication method.

Acknowledgement

This work was supported by funding from the Public Agency for Research and Development of the Republic

of Slovenia, as well as the Impol Aluminium Company and Bistral, d. o. o., from Slovenska Bistrica, Slovenia, under contract No. 1000-07-219308.

5 REFERENCES

[1] K. U. Kainer, F. von Buch, In: Magnesium alloys and technology, Ed. K. U. Kainer, DGM, Wiley-VCH, 2003; pp. 1

[2] F. Moll, K. U. Kainer, In: Magnesium alloys and technology, Ed. K. U. Kainer, DGM, Wiley-VCH, 2003; pp. 197

[3] W. Blum, B. Watzinger, P. Weidinger, In: Magnesium alloys and their applications, Eds. B. L. Mordike, K. U. Kainer, Werkstoff-Informationsgesellschaft mbH, 1998; pp. 49

[4] H. Muramatsu, K. Kondoh, E. Yuasa, T. Aizawa, JSME, 46 (**2003**) 3, 247

[5] L. Lu, K. K. Thong, M. Gupta, Composite science and technology, 63 (**2003**), 627–632

[6] L. Wang, X. Y. Qin, W. Xiong, X. G. Zhu, Mater. Sci and Eng. A, 459 (**2007**), 216

[7] J. M. Munoz-Palos, M. C. Cristina, P. Adeva, Mater. Trans. JIM, 37 (**1996**), 1602

[8] J. Zhang, Z. Fan, Y. Q. Wang, B. L: Zhou, Scripta Mater., 42 (**2000**), 1101–1106

[9] V. Milekhine, M. I. Onsoen, J. K. Solberg, T. Skaland, Intermetallics, 10 (**2002**), 743

UDK 669.181:669.14.018.8
Original scientific article/Izvirni znanstveni članek

ISSN 1580-2949
MTAEC9, 43(6)315(2009)

THE EFFECT OF WATER COOLING ON THE LEACHING BEHAVIOUR OF EAF SLAG FROM STAINLESS STEEL PRODUCTION

VPLIV VODNEGA HLAJENJA NA IZLUŽEVALNE KARAKTERISTIKE BELE EOP-ŽLINDRE

Mojca Loncnar[1], Marija Zupančič[2], Peter Bukovec[2], Anton Jaklič[1]

[1]Acroni, d. o. o., Cesta Borisa Kidriča 44, SI-4270 Jesenice, Slovenia
[2]Faculty of Chemistry and Chemical Technology, University of Ljubljana, Aškerčeva 5, SI-1000 Ljubljana, Slovenia
mojca.loncnar@acroni.si

Prejem rokopisa – received: 2009-06-24; sprejem za objavo – accepted for publication: 2009-07-20

The object of this study was the investigation of the influence of cooling methods of hot electric arc furnace (EAF) slag from stainless steel production on the leaching behaviour of the slag. EAF slags from four different grades of stainless steel were sampled and water or air cooled. Leaching tests were done according to the SIST EN 12457–4:2004 one-stage batch test. It was confirmed that the cooling method has a significant effect on the leaching behaviour of slags. In EAF water cooled slag samples, a decrease of Ca, Al, Ba and Se concentrations in the leachate was observed. On the other hand, water cooling caused an increase in leaching concentrations of Si and Mg.

Key words: EAF slag, leaching, metals, stainless steel, water cooling

Namen raziskave je bil ugotoviti, kako različni načini hlajenja bele EOP–žlindre, ki nastane pri proizvodnji nerjavnih jekel, vpliva na izluževalne karakteristike kovin in drugih pretežno anorganskih parametrov. Preučili smo žlindre, nastale pri izdelavi štirih različnih kvalitetah nerjavnih jekel. Izluževalne preizkuse smo izvedli po standardu SIST EN 12457–4:2004. Ugotovili smo, da različni načini hlajenja vplivajo na delež izluževanja kovin in drugih pretežno anorganskih parametrov. Izluževanje Ca, Al, Ba in Se je bilo pri vodno hlajenih belih EOP-žlindrah nižje kot pri hlajenju belih EOP–žlinder na zraku, obenem pa se je pri hlajenju z vodo koncentracija Si in Mg v izlužkih belih EOP-žlinder povečala.

Ključne besede: bela EOP-žlindra, izluževanje, kovine, nerjavna jekla, vodno hlajenje

1 INTRODUCTION

Steel slag is a by-product from the elaboration of steel. According to Proctor et al.[1], slags represent about 10–15 % by weight of the steel output. Slag is necessary in all metallurgical processing steps of liquid metal treatment. Steel slags include slags that are produced in the oxygen steel converter process, in electric arc furnace (EAF) steel elaboration and slags from secondary metallurgy[2].

Various alloy steel slags are generated in the alloy steel making processes. They usually contain high amounts of alloying elements, such as Cr, Ni, Mn, V, Ti and Mo. Since stainless steel slags contain a high amount of potentially toxic elements, it is necessary to treat them prior to their application or use as landfill[3].

Historically, slags have been used for the construction of roads and as fill material. However, more recently, the use of slags has been expanded as cement additives, landfill cover material and for a number of agricultural aplications[1]. In spite of the fact that many of the above mentioned applications are nowadays common practice, significant quantities of slag are still being dumped in landfills or stockpiled for long periods at steel plants.

The environmental impact must be taken into account when slags are disposed in a landfill. Steel slags are often enriched in toxic elements, in particular metals (Cu, Pb and Zn) and metalloids (As and Sb) which can be released into the environment through ageing processes and leaching[4]. The release of metals and toxic elements from slags can cause environmental problems such as water and soil pollution and a toxicological risk to humans through inhalation of small slag particles (<10 μm)[3].

Quick cooling of EAF slags is recommended as steel slag treatment before disposal or use in other applications[5]. Quick cooling is a common practice for carbon steel EAF slag, but it can also be used for stainless steel EAF slags. It is used to avoid or to minimise the disintegration of slag. Disintegration in slags is probably the result of conversion of unstable polymorphous Ca_2SiO_4 to the low (γ) temperature form of Ca_2SiO_4, which is accompanied by an increase of 10 % in volume and leads to disintegration of slags[5]. Disintegration also occurs in some slags investigated in this work.

It has been reported that if slags are quenched in water thereby producing an amorphous structure, the resulting metal extraction is substantially lower[6]. The glassy amorphous structure possesses better chemical resistance to decomposition by acid than the crystalline structure[6]. In some reported studies, the effect of the cooling mode of the molten slag on its leaching charac-

teristics was investigated through re–melting slag and cooling tests[6,7,8].

In our study the leaching characteristics of steel slags in relation to different modes of cooling of hot EAF slag were investigated in order to estimate the effect of water interactions on possible waste disposal.

2 EXPERIMENTAL PROCEDURES

The materials used in our study were slags from stainless steel production. Four electric arc furnace slags from four different stainless steel grades were selected in order to represent different types of EAF slag:

A. Electric arc furnace slag from stainless steel X2 CrNi 18–9; symbol: EX
B. Electric arc furnace slag from stainless steel AISI 304 H; symbol: E304
C. Electric arc furnace slag from stainless steel AISI 316 L, symbol: E3
D. Electric arc furnace slag from stainless steel MKM CrAl 4; symbol: EM

The chemical composition of stainless steel after the EAF procedure was determined during the process of production of stainless steel by optical emission spectrometry (OES ARL MA-310) and by IR adsorption spectroscopy (CS 344, LECO, Michigan, USA) for C and S determination.

Each type of EAF slag was emptied below the furnace, excavated and sampled while still hot. One part of a representative sample of EAF slag was left to cool down in air (1 stands for air cooled samples), whereas another part of the representative hot sample was jetted with water (2 stands for water cooled samples). Sampling of representative EAF slag samples (10–20 kg) was made according to SIST EN 15002:2006. In the case of E304 a different mode of water cooling was used, in which the slag was immersed in a bucket of cold water. A few pieces of hot E304 slag were dropped into a beaker with 500 mL deionised water to evaluate the leaching of slag components during cooling. The solution was filtered and analysed by ICP–AES (OPTIMA 2000 DV, Perkin Elmer) to determine metal concentrations (Al, Mn, Cr, Zn, Cd, Cu, Pb, Sn), by IC (761 COMPACT IC, Metrohm) for Cl^-, F^- and SO_4^{2-}, by FAAS for Mg and Ca and by UV–VIS spectrophotometry (Cary 1E (UV VIS), Varian) to determine Si and Cr(VI).

To determine the total composition of slag, XRF spectroscopy (MAGI´X FAST, PANALYTICAL) was used for major components, IR adsorption spectroscopy for C and S (CS 244 W, LECO, Michigan, USA), thermal decomposition in tube furnace and measuring F^- with electrochemical method, ICP–AES (OPTIMA 2000 DV, Perkin Elmer) and ICP-MS (4500, Agilent) for trace elements in acid digested slag samples.

To determine their leaching characteristics, slag samples were crushed to a particle size of <10 mm and leached according to the SIST EN 12457–4 one-stage batch test (24 h water extraction of slag samples at an L/S ratio of 10). The leaching tests were done in triplicate. The leachate samples were centrifuged and filtered through a 0.45 μm filter. pH, EC, redox potential and the concentration of elements were determined in the leachates. ICP–MS (Agilent 4500) was used for determination of Be, Mg, Ti, V, Cr_{tot}, Fe, Mn, Co, Ni, Cu, Zn, As, Se, Mo, Cd, Sb, Tl, Ba and Pb concentrations, ICP–AES (OPTIMA 2000 DV, Perkin Elmer) for Al and Ca, spectrophotometry (Cary 1E (UV VIS), Varian) for Si and Cr(VI), IC (761 COMPACT IC, Metrohm) for Cl^-, SO_4^{2-} and F^- and TOC analyzer (Multi N/C 2100S, Analytik Jena) for DOC.

3 RESULTS AND DISCUSSION

The chemical composition of EAF slag depends on the metallurgical process used during steel production and also depends on the steel grade. The elemental composition of the steel types from which the slag samples used in our study originated is presented in **Table 1**. As can be seen from **Table 1**, steel M showed the most different composition values comparing to other steel types resulting in different EM slag composition (see **Table 2**) and furthermore different composition of EM slag leachate (see **Figures 1–3**).

According to Shen et al.[3] the mineral phases of stainless steel slag are dicalcium and tricalcium silicate, calcium-aluminium silicate, periclase and chromites. The

Table 1: Elemental composition of stainless steel after EAF process in mass fractions *w*/%.
Preglednica 1: Elementna sestava nerjavnih kvalitet jekel po EOP-postopku v masnih deležih *w*/%.

	quality of steel, *w*/%			
element	X	304	3	M
C	1,037	0,593	0,816	0,067
Si	0,38	0,01	0,17	0,01
Mn	0,97	0,89	0,98	0,04
P	0,033	0,039	0,043	0,003
S	0,011	0,013	0,011	0,005
Cr	19,67	18,89	17,15	0,02
Cu	0,42	0,38	0,32	0,03
Ni	6,38	7,38	7,27	0,04
Al	0,01	0,004	0,008	0,275
Sn	0,015	0,013	0,011	0,005
Mo	0,36	0,38	1,54	0,01
V	0,097	0,053	0,064	0,005
Ti	0,016	0,005	0,006	0,005
Nb	0,014	0,006	0,005	0,005
W	0,031	0,054	0,05	/
Co	0,107	0,117	0,154	0,01
Zr	/	/	/	0,003
B	0,001	0,001	0,001	0,001
Pb	0,001	0,002	0,002	0,004
Sb	/	/	/	0,005
Ca	0,0005	0,0008	0,0009	0,0013

mineral composition and mineral grain size are variable with chemical composition, mode of cooling and so on. Chemical phase analysis of steel slag indicated that Fe and Cr are mainly (about 70 %) in the form of oxides while Ni and Mo are in the form of metal[9]. The chemical composition of the EAF slag samples used in our study is reported in **Table 2**. The mass fractions of main components of EAF slag were CaO (35.40–43.62 %), SiO_2 (10.78–22.95 %), Al_2O_3 (6.59–15.55 %), MgO (8.69–13.81 %), Fe_{tot} (4.40–10.60 %), MnO (1.45–3.63 wt %) and Cr_2O_3 (1.54–12.70 wt %). The amount of Cr_2O_3 was higher than that reported [1,8,9,10]. The slag samples were also enriched in metals: Mo (158–2100 mg kg^{-1}), Ba (248–560 mg kg^{-1}), Cu (112–450 mg kg^{-1}) and Zn (30–270 mg kg^{-1}).

It is well known that the leaching characteristic of metals is strongly related to the structure and chemical composition of the slag. During smelting, reduction conditions are needed to produce metals and metalloids from scrap. The absence of O_2 prevents any oxidation reactions. In the slags themselves, the elements are zerovalent or occur in more reduced valence states, often incorporated in the spinel structure, if the trivalent oxidation state is stable, as in the case of Cr^{III}, Sb^{III} and V^{III}. Spinels are oxides of the form $(M^{2+})(Fe^{3+})_2O_4$ where M^{2+} and Fe^{3+} are the divalent and trivalent cations, respectively, occupying tetrahedral and octahedral interstitial positions in the lattice formed by O^{2-}. The elements are thus also leached as more reduced species compared to other waste[11].

The leaching tests showed high and comparable pH values of leachate in the range from 11.67 to 12.75 (see **Table 3**). Shen et al.[9] reported high and similar pH values in leachate in the range from 10.28 to 10.81. It has been suggested that the release of Ca from slag may be the main reason for the increase in pH according to the chemical composition of the water[9]. Cornelis et al.[11] reported that freshly produced alkaline wastes have a

Table 2: Total chemical composition of EAF slags. Results are presented as the mean value of duplicate analysis with the standard deviation.
Preglednica 2: Kemijska sestava EOP–žlinder. Rezultati so podani kot povprečje dveh paralelk ± standardni odmik.

Sample	*w*/%						
	CaO	SiO_2	Al_2O_3	MgO	Cr_2O_3	MnO	Fe
EX1	37,46 ± 0,07	20,24 ± 0,06	6,59 ± 0,06	8,690 ± 0,002	12,0 ± 0,1	3,54 ± 0,038	6,7 ± 0,2
EX2	35,4 ± 0,4	19,5 ± 0,2	6,65 ± 0,04	9,10 ± 0,04	12,7 ± 0,3	3,63 ± 0,018	7,3 ± 0,5
E3041	41,425 ± 0,002	18,82 ± 0,04	8,856 ± 0,001	9,55 ± 0,04	9,18 ± 0,04	3,03 ± 0,01	4,4 ± 0,1
E3042	38,2 ± 0,2	18,52 ± 0,05	8,08 ± 0,03	9,59 ± 0,02	10,61 ± 0,01	3,579 ± 0,004	5,2 ± 0,1
E31	36,4 ± 0,1	22,4 ± 0,2	7,47 ± 0,09	13,8 ± 0,1	5,91 ± 0,06	3,29 ± 0,014	8,0 ± 0,2
E32	37,34 ± 0,01	22,95 ± 0,02	7,845 ± 0,004	13,6 ± 0,1	5,24 ± 0,06	3,23 ± 0,006	6,0 ± 0,2
EM1	43,6 ± 0,1	10,78 ± 0,03	15,55 ± 0,07	10,73 ± 0,04	1,540 ± 0,002	1,45 ± 0,032	10,6 ± 0,2
EM2	35,4 ± 0,2	18,83 ± 0,04	11,13 ± 0,08	8,70 ± 0,03	3,04 ± 0,03	1,76 ± 0,002	10,5 ± 0,1
Sample	*w*/%						
	F^-	TiO_2	Ni	V_2O_5	S	C	
EX1	0,64 ± 0,01	0,99 ± 0,01	0,71 ± 0,06	0,283 ± 0,001	0,166 ± 0,003	0,16	
EX2	0,50	1,03 ± 0,02	0,65 ± 0,09	0,285 ± 0,003	0,150 ± 0,001	0,23	
E3041	1,19 ± 0,02	1,01 ± 0,01	0,30 ± 0,03	0,243 ± 0,005	0,296 ± 0,003	0,17 ± 0,01	
E3042	0,81 ± 0,01	0,842 ± 0,001	0,43 ± 0,04	0,266 ± 0,006	0,256 ± 0,004	0,18	
E31	0,122 ± 0,005	0,78 ± 0,01	0,76 ± 0,09	0,139 ± 0,001	0,095 ± 0,001	0,15	
E32	0,129 ± 0,002	0,755 ± 0,003	0,76 ± 0,06	0,137 ± 0,002	0,112 ± 0,003	0,21 ± 0,005	
EM1	0,83 ± 0,01	0,327 ± 0,003	0,11 ± 0,01	0,042 ± 0,001	0,593 ± 0,005	0,13	
EM2	0,84 ± 0,02	0,473 ± 0,004	0,18 ± 0,03	0,074 ± 0,001	0,417 ± 0,003	0,37 ± 0,01	
Sample	*c*/(mg kg^{-1})						
	P	Co	Cu	Zn	As		
EX1	137 ± 2	114 ± 8	412 ± 30	226 ± 5	7,6 ± 0,5		
EX2	164 ± 2	120 ± 10	450 ± 40	87 ± 4	7,6 ± 0,7		
E3041	137 ± 2	43 ± 2	145 ± 8	150 ± 20	6,2 ± 0,4		
E3042	120 ± 7	60 ± 4	200 ± 1	58 ± 4	6,0 ± 0,1		
E31	161	140 ± 20	290 ± 40	30 ± 1	9 ± 1		
E32	127 ± 4	150 ± 20	310 ± 60	38 ± 6	9 ± 2		
EM1	648 ± 7	23,2 ± 0,2	112,3 ± 0,7	270 ± 40	6,9 ± 0,2		
EM2	630 ± 20	35 ± 2	150 ± 10	246 ± 5	7,0 ± 0,6		
Sample	*c*/(mg kg^{-1})						
	Se	Mo	Cd	Ba	Pb		
EX1	6,4 ± 0,9	470 ± 20	1,27 ± 0,03	251 ± 5	42 ± 1		
EX2	10,9 ± 0,6	440 ± 40	0,93 ± 0,08	270 ± 2	8,1 ± 0,1		
E3041	11,5 ± 0,4	250 ± 30	0,42 ± 0,03	259 ± 1	5,5 ± 0,1		
E3042	6,800 ± 0,003	320 ± 10	0,50 ± 0,01	248 ± 1	6,4 ± 0,2		
E31	<4	2100 ± 200	0,83 ± 0,07	560 ± 10	<1		
E32	<4	2100 ± 100	0,7 ± 0,2	548 ± 1	2,11 ± 0,04		
EM1	7 ± 2	158 ± 7	0,41 ± 0,02	309 ± 1	17 ± 3		
EM2	<4	290 ± 60	0,69 ± 0,01	314 ± 6	30,2 ± 0,7		

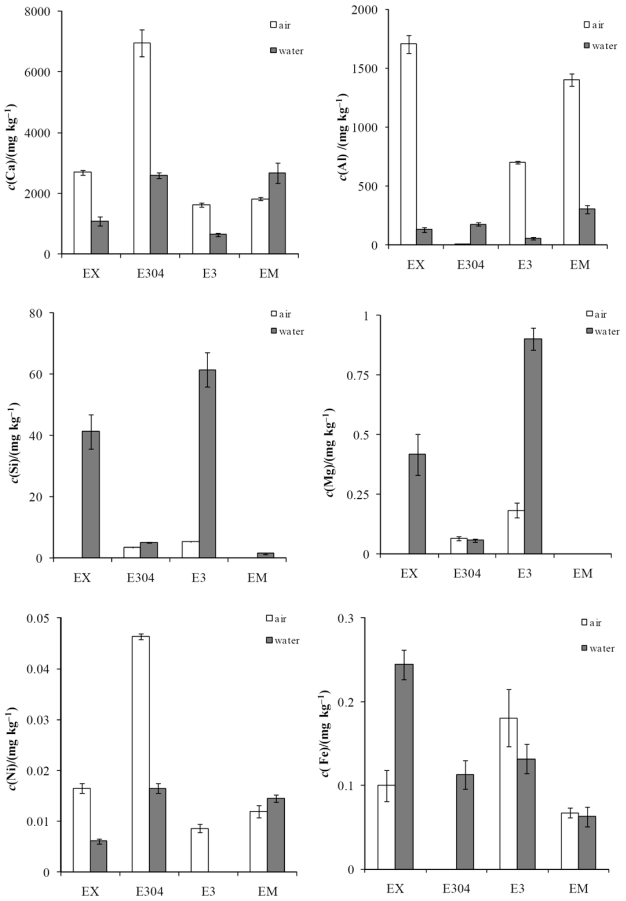

Figure 1: Results of the leaching test of major elements in air and water cooled EAF slags in mg kg^{-1} (Ca, Al, Si, Mg, Ni, Fe). Results are presented as the mean value of triplicate analysis with the standard deviation as error bars. Values that are not presented in the Figure are under the limit of detection; for Mg (0.05 mg kg^{-1}); for Si (0.1 mg kg^{-1}); for Ni (0.005 mg kg^{-1}); for Fe (0.025 mg kg^{-1}).

Slika 1: Primerjalno izluževanje glavnih elementov (Ca, Al, Si, Mg, Ni, Fe) v EOP–žlindrah, hlajenih na zraku in z vodo v mg kg^{-1}. Rezultati so podani kot povprečje treh paralelk in standardni odmik. Rezultati, ki v grafih niso podani so pod mejo detekcije, ki je za Mg (0.05 mg kg^{-1}); za Si (0.1 mg kg^{-1}); za Ni (0.005 mg kg^{-1}); za Fe (0.025 mg kg^{-1}).

narrow pH distribution (between 10 and 13), because the leachate pH is mainly controlled by dissolution of a limited set of minerals containing Ca, such as portlandite ($Ca(OH)_2$), calcium monosulfoaluminate ($Ca_4[Al(OH)_6]_2SO_4{\cdot}13H_2O$), hydrocalumite ($Ca_4[Al(OH)_6]_2{\cdot}6H_2O$), ettringite ($Ca_6[Al(OH)_6](SO_4)_3{\cdot}32H_2O$), calcium silicate hydrate (CSH) and calcite ($CaCO_3$). The quantities of these minerals, however, may vary, as reflected in the acid neutralization capacity (ANC). According to Cornelis et al.[11] the minerals containing Ca mentioned above, exert control over leaching. In our study a narrow pH distribution and high pH values were also found. The high pH values in leachates are a consequence of the high content of Ca in the leachate (see **Figure 1**), probably due to Ca minerals in slags such as portlandite and calcite.

The main elements in slags were Ca, Mg, Si, Al, Mn and Fe. Although they are not mentioned in Slovenian

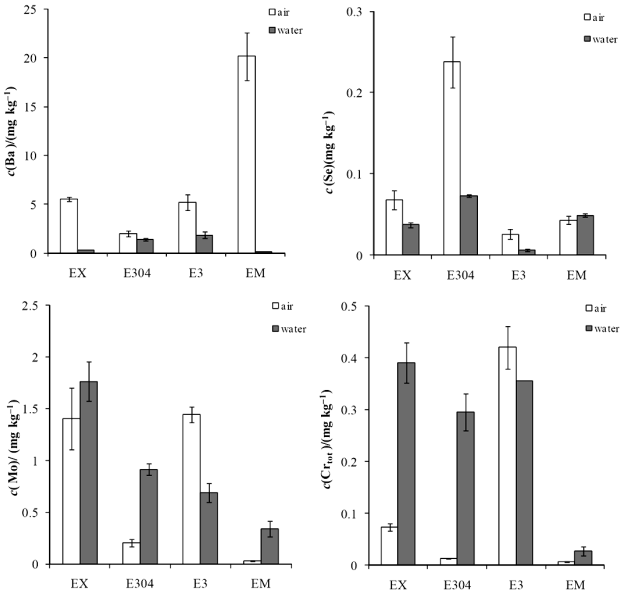

Figure 2: Results of the leaching test of minor elements (Ba, Se, Mo, Cr) in air and water cooled EAF slags in mg kg^{-1}. Results are presented as the mean value of triplicate analysis with the standard deviation as error bars.

Slika 2: Primerjalno izluževanje elementov v sledovih (Ba, Se, Mo, Cr) v EOP–žlindrah, hlajenih na zraku in z vodo v mg kg^{-1}. Rezultati so podani kot povprečje treh paralelk in standardni odmik.

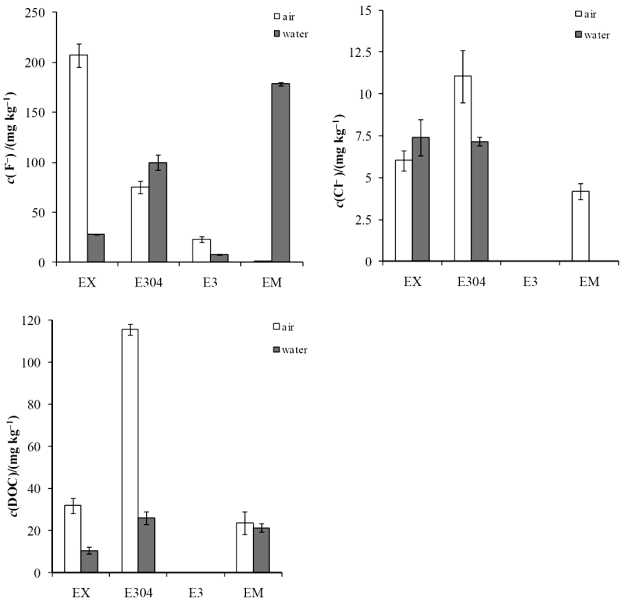

Figure 3: Leaching of F^-, Cl^- and DOC according to the one–stage batch leaching test. Results are presented as the mean value of triplicate analysis with the standard deviation as error bars. Values that are not presented in the Figure are under the limit of detection; for Cl^- (2.5 mg kg^{-1}); for DOC (10 mg kg^{-1}).

Slika 3: Izluževanje F^-, Cl^- in DOC z enostopenjskim šaržnim preskusom. Rezultati so podani kot povprečje treh paralelk in standardni odmik. Rezultati, ki v grafih niso podani, so pod mejo detekcije, ki je za Cl^- (2.5 mg kg^{-1}); za DOC (10 mg kg^{-1}).

Table 3: Results of standard leaching test SIST EN 12457–4 presented as the mean value of triplicate analysis with the standard deviation.
Preglednica 3: Rezultati nekaterih parametrov izluževalnega preizkusa SIST EN 12457–4. Rezultati so podani kot povprečje treh paralelk ± standardni odmik.

Parameter	Unit	EX1	EX2	E3041	E3042
pH		11,85 ± 0,09	11,85 ± 0,10	12,75 ± 0,07	12,43 ± 0,03
EC	mS cm^{-1}	1,80 ± 0,10	1,02 ± 0,09	6,40 ± 0,30	2,77 ± 0,08
Redox potential	mV	217,0 ± 0,6	223 ± 7	142 ± 8	186 ± 4
Parameter	Unit	E31	E32	EM1	EM2
pH		12,03 ± 0,03	11,67 ± 0,01	11,89 ± 0,05	12,37 ± 0,01
EC	mS cm^{-1}	1,41 ± 0,07	0,65 ± 0,07	1,5 ± 0,1	2,6 ± 0,1
Redox potential	mV	148 ± 3	56	101	115 ± 8

waste legislation[12], they were also investigated in leaching tests because of the strong dependence between major element concentrations present in slag and the leaching characteristics of trace elements.[13]

The most leachable element from air cooled slag is Ca, in the range from (1620 ± 80) mg kg^{-1} (E31) to (7000 ± 400) mg kg^{-1} (E3041) which represents 0.62 % and 2.36 % of the total Ca concentration, respectively. The amount of Al leached compared to the total Al concentration is in most cases even higher than for Ca, namely from 1.77 % (E31) to 4.88 % (EX1) of the total concentration, respectively, but in the case slag E3041 leaching of Al is negligible. The leaching of Si, Mg, Ni and Fe from air cooled slags was small (see **Figure 1**). Mn concentrations in the leachate were under the detection limit of method (0.025 mg kg^{-1}) and are not presented in **Figure 1**.

The leaching of Ca decreased in rapidly water cooled slag samples, with the exception of slag EM. The leaching of Al also decreased in all samples except E304, when cooled by water. The leaching of Al after rapid water cooling decreased significantly, especially in slag EX by 92.35 % and in slag EM by 78.57 % in comparison with air cooled samples. As can be seen from **Table 4** the concentration of Ca and Al in water after several pieces of hot E304 slag were dropped into a beaker containing 500 mL deionised water was quite high (252 mg L^{-1} and 72.1 mg L^{-1}, respectively). However those values could not be directly compared to leaching values due to the different amount of slag samples in both cases. It is impossible to weigh hot slag to determine the S/L ratio. Nevertheless, it can be concluded that leaching of Al and Ca decreased when rapid water cooling was used due to ability of Ca and Al to solubilize in water after jetting hot slag samples. In the case of Si and Mg, water cooling caused an increase in leaching of elements from slags. The leaching of Si increased in all samples cooled with water. Leaching of Mg increased at all samples, too, except for slag E304 and slag EM, compared to air cooled samples. As can be seen from **Table 4,** the concentration of Si and Mg in water after a several E304 slag were dropped into water were negligible compared to the concentration of Ca and Al. The opposite effect was observed in leaching of Mg and Si in comparison to the concentration of Mg and Si in water after dropping several of hot slag into water.

Tossavainen el at.[8] reported that leaching of Si increased in many cases, while Al leaching decreased when cooled rapidly. Different methods of cooling

Table 4: Chemical composition of water after dropping several pieces of hot slag E304 into 500 mL of deionized water.
Preglednica 4: Rezultati analize vode, potem ko smo v 500 mL deionizirane vode potopili par kosov vroče žlindre E304.

Parameter	c/(mg L^{-1})
Ca	252
Al	72,1
Si	0,26
Mg	0,005
Mn	<0.01
Fe	<0.025
Cr	0,240
Cr(VI)	0,233
Zn	<0.01
Cd	<0.01
Cu	<0.01
Pb	<0.03
Sn	<0.1
Cl^-	4,00
F^-	5,65
SO_{42-}	1,12

< LOD = less then LOD

Table 5: Results of leaching test for Cr and Cr(VI) in mg kg^{-1}. Results are presented as the mean value of triplicate analysis with the standard deviation.
Preglednica 5: Rezultati izlužilnega testa za parameter Cr in Cr(VI). Rezultati so podani kot povprečje treh paralelk ± standardni odmik.

	c/(mg kg^{-1})	
Sample	Cr_{tot}	Cr(VI)
EX1	0,074 ± 0,007	<0.1
EX2	0,39 ± 0,04	0,44 ± 0,02
E3041	0,012 ± 0,002	<0.1
E3042	0,30 ± 0,04	0,28 ± 0,08
E31	0,42 ± 0,04	0,36 ± 0,04
E32	0,3552 ± 0,0004	0,35 ± 0,02
EM1	0,0064 ± 0,0008	<0.1
EM2	0,028 ± 0,008	<0.1

< LOD = less then LOD

(re-melting and water granulation or re-melting and cooling in a crucible) were used by Tossavainen el at.[8], but the results obtained were similar to those in our study.

Due to the considerable amount of data obtained for leaching of minor elements, only the most significant ones are presented in **Figure 2**. The leaching from EAF stainless steel slag was generally very low. However some elements in air cooled slags exceeded the legal limit for inert waste material[12]: the leaching concentration of Se from slag E3041 was (0.24 ± 0.03) mg kg^{-1} (limit value: 0.1 mg kg^{-1}) and of Mo from slag EX1 was (1.4 ± 0.3) mg kg^{-1} and from slag E31 was (1.44 ± 0.07) mg kg^{-1} (limit value: 0.5 mg kg^{-1}). Leaching concentrations of Ba from EM1 slag was (20 ± 2) mg kg^{-1} and is at the limit value (limit value: 20 mg kg^{-1}).

As is shown in **Figure 2**, in comparison to air cooled slag, water cooling decreased the leaching of Ba and Se, with the exception of slag EM. Water cooling decreased the leaching of Ba in the range from 1.44 to more than 150– fold in comparison to air cooling. The leachable concentration of Ba from air cooled slag was in the range from (2.0 ± 0.3) mg kg^{-1} (E3041) to (20 ± 2) mg kg^{-1} (EM1) representing 0.77 % and 6.47 % of the total Ba concentration, respectively. A similar trend was observed in leaching of Mo and Cr on water cooling. Leaching of Mo in the water cooling mode decreased for slag E3, while it increased for slag E304 and slag EM, but in the case of EX it was similar to air cooled samples. A similar result was obtained in the case of Cr leaching where in all three slags (EX, E304 and EM) it increased, while, a decrease of leaching in slag E31 was observed in comparison to air cooled slags. Cr(VI) was also analysed in all leachate samples and the results (see **Table 5**) showed that almost all of the total Cr in leachate was present in form of Cr(VI). Soluble Cr is almost always hexavalent because equilibrium with insoluble Ca–Cr^{III} minerals causes the $Cr(OH)_4^-$ concentration to be very low[9].

The leaching characteristics of F^-, Cl^-, DOC are presented in **Figure 3**. The leaching of SO_4^{2-} was negligible and is not shown in **Figure 3**. The leaching of F^- is the highest in slag EX1, (210 ± 10) mg kg^{-1}.

In the cases of slag EX and slag E3 a decrease in leachate F^- concentrations was observed when cooled with water. On the other hand, an increase of F^- concentrations was observed in water cooled slag E304 and slag EM samples. Water cooling in most cases caused a decrease of Cl^- concentrations (an exception was slag EX) and also a decrease of DOC concentrations.

The results of our investigation showed that different modes of cooling affected the leaching behaviour of slags. Mainly it affects the leaching characteristics of major elements such as Ca, Al, Si, Mg and significantly the leaching of Ba and Se. Some similarities in leaching of Mo and Cr were also observed.

The results from the single batch leaching test were compared to limits set by Slovenian legislation for the acceptance of inert waste for landfilling[12]. From the comparison it can be concluded that most potentially hazardous elements did not exceed the established criteria, except for air cooled slag, where Mo (in slag E31 and slag EX1), F^- (in slag EX1, slag E3041 and slag E31), Se (in slag E3041) where concentrations in leachate exceeded the limit values. Leaching concentrations of Ba from EM1 slag was at the limit value. Although F^- concentrations in leachate from air cooled slag in most cases exceeded the legal regulation (10 mg kg^{-1}), it represents only from 0.63 % (E31) to 3.23 % (EX1) of the total fluoride concentration in slag.

Procter et al.[1] reported that the Sb, As, Ba, Be, Cd, Cr_{tot}, Cr(VI), Pb, Mn, Hg, Ni, Se, Ag, Tl and Zn concentrations in leachates of steel slag, using the TCLP test for leaching evaluation, were very low. The only metals that were detected at concentrations higher than 1 mg L^{-1}, were Ba and Mn. These metals were also found at much higher concentrations in the slag samples. Also in our study, although using different standard procedure, high values for Ba in leachtate were observed (see **Figure 2**).

4 CONCLUSION

The results of our study showed that leaching of metals from EAF slag is generally very low. These results indicate that metals are very tightly bound and are not released from the matrix. Nevertheless, some exceptions exist. Relatively high leachate concentrations were observed for Ba and Mo. F^- is the most problematic anion in leachate. The solubility of metals in slag depends on the solubility of the major phase. Leaching of major elements (for example Ca) is more extensive. Due to the high content of Ca in slags, EAF slags are alkaline solid waste.

Water cooling had an effect on the leaching behaviour of the investigated slags. Water cooling caused a decrease in leaching of Ca, Al, Ba and Se, and on the other hand, increased leaching of Si and Mg. Some similarities in leaching of Mo and Cr after water cooling were observed. Mo and Cr leaching in all three slags (EX2, E3042 and EM2) increased, while for slag E32 a decrease in leachable metal concentrations comparable to air cooled slags were observed.

According to Sloot[14], the single step extraction test is very limited in its capability to provide answers to complex questions such as: whether a material can be disposed in a particular type of landfill or it the material been sufficiently treated to meet requirements for disposal or beneficial applications. Future research will be focused on more sophisticated testing that will provide insight into the mechanistic aspects of leaching of EAF slag and on the effect of the rate of cooling on slag leaching behaviour.

To investigate the cooling effect on the leachability of slag in detail the mineralogical characteristics of water and air cooled slags will be included in further studies.

ACKNOWLEDGEMENTS

The operational part of this study was financed by the European Union, European Social Fund. Operation implemented in the framework of the Operational Programme for Human Resources Development for the Period 2007–2013, Priority axis 1: Promoting entrepreneurship and adaptability, Main type of activity 1.1.: Experts and researchers for competitive enterprises.

5 REFERENCES

[1] D. M. Proctor, K. A. Fehling, E. C. Shay, J. L. Wittenborn, J. J. Green, C. Avent, R. D. Bigham, M. Connolly, B. Lee, T. O. Shepker, M. A. Zak, Physical and chemical characteristics of blast furnace, basic oxygen furnace and electric arc furnace steel industry slags, Environ.Sci.Technol., 34 (**2000**), 1576–1582

[2] D. Janke, L. Savov, M. E. Vogel, Sustainable metals management, Secondary materials in steel production and recycling, Springer, Netherlands, **2006**, 313–334

[3] H. Shen, E. Forssberg, An overview of recovery of metals from slags, Waste manage., 23 (**2003**), 933–949

[4] V. Ettler, Z. Johan, B. Kříbek, O. Šebek, M. Mihaljevič, Mineralogy and environmental stability of slags from the Tsumeb smelter, Namibia, Appl. geochem. 24 (**2009**), 1–15

[5] M. P. Luxán, R. Sotolongo, F. Dorrego, E. Herrero, Characteristics of the slags produced in the fusion of scrap steel by electric arc furnace, Cem. concr. res., 30 (**2000**), 517–519

[6] M. Baghalha, V. G. Papangelakis, W. Curlook, Factors affecting the leachability of Ni/Co/Cu slags at high temperature, Hydrometallurgy, 85 (**2007**), 42–52

[7] Y.–M. Kuo, J.–W. Wang, H.–R. Chao, C.–T. Wang, G.–P. Chang–Chien, Effect of cooling rate and basicity during vitrification of fly ash Part 2. On the chemical stability and acid resistance of slags, J. hazard. mater., 152 (**2008**), 554–562

[8] M. Tossavainen, F. Engstrom, Q. Yang, N., Menad, M. Lidstrom Larsson, B. Bjorkman, Characteristics of steel slag under different cooling conditions, Waste manage., 27 (**2007**), 1335–1344

[9] H. Shen, E. Forssberg, U. Nordström, Physicochemical and mineralogical properties of stainless steel slags oriented to metal recovery, Resour. conserv. recycl., 40 (**2004**), 245–271

[10] A. M. Fällman, Leaching of chromium and barium from steel slag in laboratory and field tests – a solubility controlled process? Waste manage., 20 (**2000**), 149–154

[11] G. Cornelis, C. Annette Johnson, T. Van Gerven, C. Vandecasteele, Leaching mechanisms of oxyanionic metalloid and metal species in alkaline solid wastes: A review, Appl. geochem., 23 (**2008**), 955–976

[12] Decree on the landfill of waste, Official Gazette of Republic of Slovenia, 32/2006, amendment 98/2007, 62/2008

[13] M. Tossavainen, E. Forssberg, Leaching behavior of rock material and slag used in road construction – a mineralogical interpretation, Process metallurgy, Steel res. 71, 11 (**2000**), 442–448

[14] H. A. van der Sloot, Developments in testing for environmental impact assessment–editorial, Waste manage., 22 (**2002**), 693–694

UDK 678.742:620.179.11
Original scientific article/Izvirni znanstveni članek

ISSN 1580-2949
MTAEC9, 43(6)323(2009)

MODIFIKACIJA POLIMERA POLIETILEN NAFTALAT Z OBDELAVO V KISIKOVI PLAZMI

MODIFICATION OF A POLYETHYLENE NAPHTHALATE POLYMER USING AN OXYGEN PLASMA TREATMENT

Alenka Vesel, Kristina Eleršič, Ita Junkar, Barbara Malič

Institut "Jožef Stefan", Jamova 39, 1000 Ljubljana, Slovenija
alenka.vesel@ijs.si

Prejem rokopisa – received: 2009-03-09; sprejem za objavo – accepted for publication: 2009-08-25

We have studied the surface modification of a polyethylene naphthalate (PEN) foil with an oxygen plasma. The samples of PEN were treated in an inductively coupled RF plasma with a frequency of 27.12 MHz and at an output power of about 200 W. The gas pressure was 75 Pa. The samples were exposed directly to the glow region of the plasma. The samples were treated for different periods, ranging from 3 s to 60 s. Chemical changes in the surface composition after the plasma treatments were studied using high-resolution XPS (X-ray Photoelectron Spectroscopy), while the wettability was determined by water-contact-angle measurements (WCA). The untreated surface was hydrophobic with a water contact angle of about 90°. After 10 s of treatment the surface became very hydrophilic, with a contact angle of only about 3°. The oxygen concentration was increased from an initial mole fraction 21 % to about 35–38 %, depending on the treatment time. The surface oxidation resulted in the formation of different chemical bonds between the carbon and the oxygen, e.g., C=O, O–C–O, O–C=O and –C(=O)–O–C(=O)–.

Key words: XPS, PEN, PET, polymer, plasma, oxygen, modification, surface, functionalization, hydrophilic

V članku opisujemo modifikacijo površine polimera PEN (polyethylene naphthalate) s kisikovo plazmo. Plazmo smo generirali z induktivno sklopljenim radiofrekvenčnim generatorjem s frekvenco 27,12 MHz in izhodno močjo okoli 200 W. Tlak kisika je bil 75 Pa. Vzorci polimera PEN so bili izpostavljeni plazmi različno dolgo časa: od 3 s do 60 s. Spremembe v kemijski sestavi površine smo ugotavljali z metodo XPS (rentgenska fotoelektronska spektroskopija), spremembe v omočjivosti površine pa z meritvijo kontaktnega kota vodne kapljice. Ta je bil na neobdelani površini 90°. Po 10-sekundni obdelavi v kisikovi plazmi je površina polimera postala močno hidrofilna s kontaktnim kotom le okoli 3°. Pri še daljših izpostavah plazmi je bil kontaktni kot še manjši, tako da je bil že pod mejo merljivosti. Iz XPS-meritev izhaja, da je koncentracija kisika na površini narasla od začetnih molskih deležih 21 % na 35–38 %, odvisno od časa obdelave. Posledica vezave kisika na površino polimera je nastanek novih funkcionalnih skupin, kot npr. C=O, O–C–O, O–C=O in –C(=O)–O–C(=O)–.

Ključne besede: XPS, PEN, PET, polimer, plazma, kisik, modifikacija, površina, funkcionalizacija, hidrofiličen

1 INTRODUCTION

Polymer materials are known to be hydrophobic. They have very poor adhesion properties and wettability. Therefore, they must be modified before applications like printing, painting, coating, to improve the biocompatibility, etc. One of the most promising methods for modifying the surface properties of polymer materials is plasma treatment.[1–9] Plasma treatment is an ecologically suitable method and it is replacing the traditional wet chemical techniques, which can involve harmful chemicals. Plasma treatment affects only the first few nanometers of a material without changing the bulk properties.[1] It is a very quick method, because usually for surface functionalization only a few seconds of treatment are necessary. Using a treatment in a plasma of different gases we can achieve a wide range of surface wettability, from moderate hydrophilicity to significant hydrophobicity. This hydrophobicity can be achieved by a treatment in plasma created in halogens, while for achieving the hydrophilicity of the surface it is best to use an oxygen plasma. In some applications, especially biological, when we want to coat the substrate with proteins or DNA, for example, a nitrogen or ammonia plasma is more desirable than an oxygen plasma.[2] It should be noted that plasma treatment does not produce a unique functionality on a polymer surface. Typically, a distribution of several different functional groups is produced. Some of the functional groups may be important and some may actually be detrimental. Thus, it is desirable to determine which of the functional groups is important for a given application and to attempt to shift the distribution in favour of a specific functionality by changing the plasma gas or other plasma parameters.[3] In an oxygen plasma different functional groups, like C–O, O–C–O, C=O, O=C–O, or even more exotic groups, can be produced on the surface.[3–6] When the polymer is exposed to plasma the first effect that appears at the polymer surface is actually just removing of contaminants, which may also lead to improved wettability. With a further treatment time the insertion of oxygen atoms from the plasma into the polymer surface appears to lead to the formation of various functional groups that change the surface wettability. With a prolonged treatment time, etching of the surface occurs, which leads to an increased surface roughness and changes in the surface morphology.

In the present paper we present a study on the functionalization of polymer PEN (Polyethylene Naphthalate (Teonex®)) by low-pressure radio-frequency (RF) oxygen plasma. The surface of the treated polymer was characterized by applying XPS (X-ray Photoelectron Spectroscopy) and WCA (Water Contact Angle) measurements. According to a literature review, a modification of the polymer PEN has already been studied by using RF nitrogen plasma[10] and atmospheric-pressure microwave[8] and RF[9] plasma. The authors found that the polarity of the PEN surface increased 10 times, but the contact angle on the treated surface was still relatively large (21.7°).[9]

2 EXPERIMENTAL

2.1 Plasma modification

The samples of polymer Teonex® Polyethylene Naphthalate (PEN) were treated in the experimental system shown in **Figure 1**. The chemical structure of the PEN is shown in **Figure 2**. The system is pumped with a two-stage oil rotary pump with a pumping speed of 16 m^3/h. The discharge chamber is a Pyrex glass cylinder with a length of 50 cm and an inner diameter of 3.6 cm. The plasma is created inside the discharge chamber with an inductively coupled RF generator, operating at a frequency of 27.12 MHz and an output power of about 200 W. The plasma's parameters are measured with a double Langmuir probe and a catalytic probe. The Langmuir probe is placed into the discharge chamber, while the catalytic probe is mounted in the afterglow chamber. Commercially available oxygen is leaked into the discharge chamber. The pressure is measured with an absolute vacuum gauge and is adjusted during continuous pumping using a precise leak valve. During our experiments the pressure was fixed at 75 Pa, where the density of the oxygen atoms was the highest. Using these discharge parameters an oxygen plasma with an ion density of 8×10^{15} m^{-3}, an electron temperature of 5 eV, and a density of neutral oxygen atoms of 4×10^{21} m^{-3} was obtained.

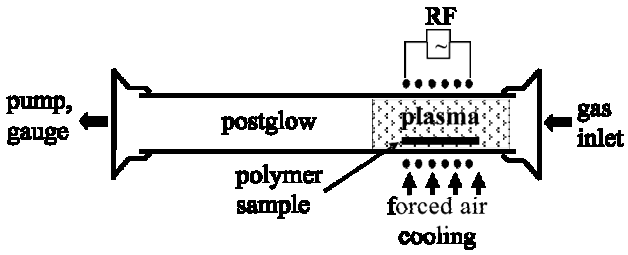

Figure 1: The plasma chamber for treating the samples
Slika 1: Plazemski sistem za obdelavo vzorcev

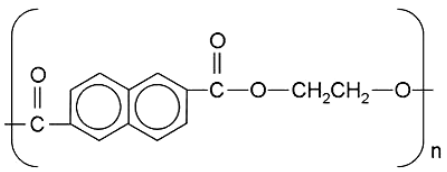

Figure 2: Chemical structure of PEN
Slika 2: Kemijska struktura PEN

2.2 XPS characterization

The samples were exposed to air for a few minutes after the plasma treatment and then mounted in the XPS instrument (TFA XPS Physical Electronics). The base pressure in the XPS analysis chamber was about 6×10^{-10} mbar. The samples were excited with X-rays over a 400-µm spot area with monochromatic Al $K_{\alpha 1,2}$ radiation at 1486.6 eV. The photoelectrons were detected with a hemispherical analyzer positioned at an angle of 45° with respect to the normal to the sample surface. The energy resolution was about 0.6 eV. Survey-scan spectra were made at a pass energy of 187.85 eV, while for C1s and O1s individual high-resolution spectra were taken at a pass energy of 23.5 eV and a 0.1-eV step. Since the samples are insulators, we used an additional electron gun to allow for surface neutralization during the measurements. The spectra were fitted using MultiPak v7.3.1 software from Physical Electronics, which was supplied with the spectrometer. The curves were fitted with symmetrical Gauss-Lorentz functions. The peak width (FWHM) was fixed during the fitting process. The main C 1s peak was shifted to 284.8 eV.[11] A Shirley-type background subtraction was used.

2.3 Contact angle measurements

The wettability was examined immediately after the plasma treatment by measuring the water contact angle with a demineralised water droplet of volume 3 µL. Homemade apparatus equipped with a CCD camera and a PC computer was used to take high-resolution pictures of the water drop on the sample surface. Each determination was obtained by averaging the results of five measurements. The relative humidity (45 %) and temperature (25 °C) were monitored continuously and were found not to vary significantly during the contact-angle measurements. The contact angles were measured by our own software, which enables the fitting of the water drop on the surface in order to allow a relatively precise determination of the contact angle. The results of the water-contact measurements are shown in **Table 1**.

Table 1: Contact angles of a water drop (WCA) on the surface of the PEN foil
Tabela 1: Kontaktni kot vodne kapljice na površini folije PEN

Sample	WCA (°)
untreated	88° – 95°
treated for 3 s	11° – 14°
treated for 10 s	≈ 3°
treated for 30 s	Not measurable
treated for 60 s	Not measurable

3 RESULTS

Figure 3 shows a comparison of the carbon C 1s peaks for samples of PEN polymer that were exposed to plasma for different times. We can see a large difference in the intensity of the high-energy peaks between the untreated polymer and the one treated for 3 s. With treatment times longer than 3 s the difference is less pronounced, indicating surface saturation with oxygen.

The surface composition of the untreated and treated samples is shown in **Table 2**. We can see that after plasma treatment the oxygen concentration increased from the mole fraction 21 % to 35 % or to 38 % for 3 s or 60 s of treatment, respectively. The other elements N, Na, S and Si that were also found on the surface are impurities.

Figure 4 shows the detailed structure of the carbon C 1s peak for the untreated sample. The peak consists of three sub-peaks belonging to the –C=C bond (C1), to the C–O bond (C2) and to the O=C–O bond from the ester group (C3). **Figure 5** shows an example of a carbon peak for a sample treated for 3 s. This peak consists of five sub-peaks. In comparison with the untreated sample two new sub-peaks are observed: C23, corresponding to the C=O or O–C–O bond; and C4, which according to its very high binding energy, corresponds the

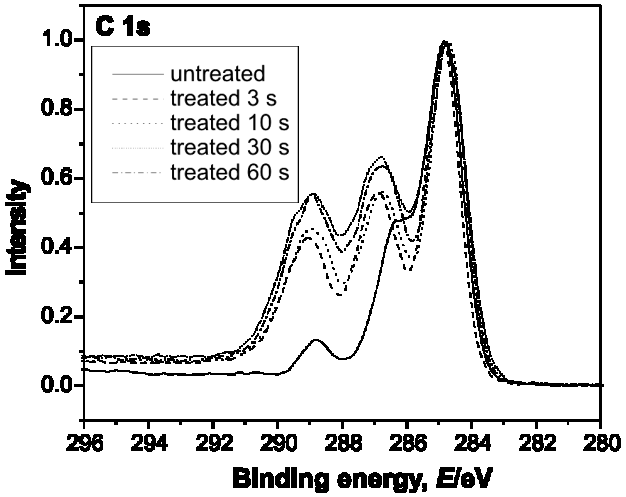

Figure 3: Comparison of high-resolution XPS peaks of carbon C1s peaks for different treatment times.

Slika 3: Primerjava visokoločljivih XPS-spektrov ogljika za različne čase obdelave

Table 2: Surface composition of PEN samples at different treatment times (in moll fractions, *x*/%)

Tabela 2: Sestava površine vzorcev polimera PEN v odvisnosti od časa obdelave v plazmi (v molskih deležih, *x*/%)

Sample	C	O	N	Na	S	Si
untreated	74.9	21.0	1.9	1.1	0.8	0.4
treated for 3 s	63.8	35.0	0.8	/	/	0.4
treated for 10 s	62.6	36.5	/	/	0.1	0.9
treated for 30 s	61.7	37.2	0.6	/	/	0.5
treated for 60 s	58.1	38.3	/	2.1	0.4	1.0

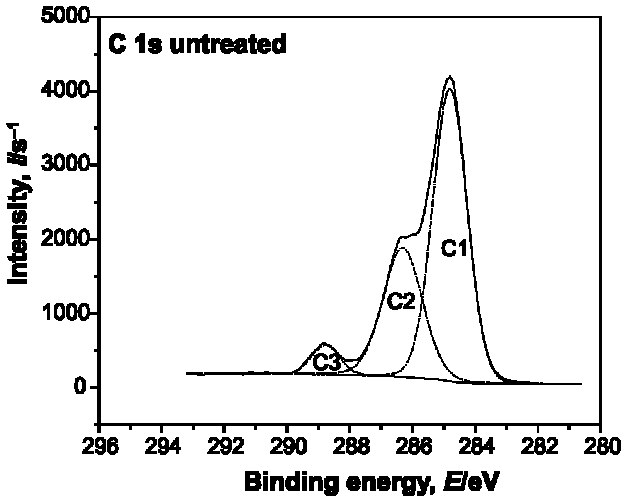

Figure 4: Carbon C 1s peak of untreated PEN sample with three sub-peaks

Slika 4: Ogljikov vrh C 1s neobdelane folije PEN s tremi podvrhovi

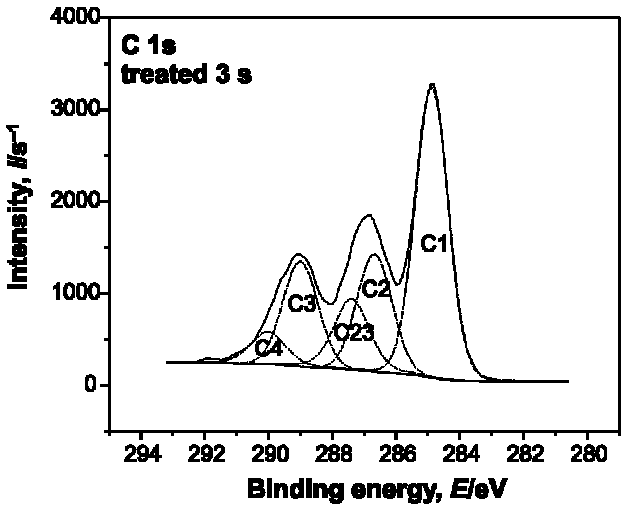

Figure 5: Carbon C 1s peak of PEN sample treated in plasma for 3 s with five sub-peaks

Slika 5: Ogljikov vrh C 1s plazemsko obdelane (3 s) folije PEN s petimi podvrhovi

–C(=O)–O–C(=O)– group. Similar functional groups were also observed on other PEN samples treated for longer times. **Table 3** summarizes the concentrations of the different types of functional groups that were obtained for the PEN samples for different treatment times.

4 DISCUSSION

From the XPS results shown in **Table 3** we can see that the concentration of the sub-peak C1 belonging to the –C=C bonds from the aromatic rings decreased after the plasma treatment. We can conclude that the oxygen atoms probably destroy the aromatic rings by scission of the –C=C bonds, which leads to opening of the aromatic rings. Furthermore, the concentration of the sub-peak C2

Table 3: Concentration of functional groups at the PEN surface versus treatment time
Tabela 3: Koncentracija funkcionalnih skupin na površini folije PEN v odvisnosti od časa obdelave v plazmi

	Peak designation	C1	C2	C23	C3	C4
	Binding energy (eV)	≈284.8	≈286.4	≈287.3	≈288.9	≈290.0
	Assigned functional group	C-C, C=C	C-O	C=O O-C-O	O=C-O	
Sample	untreated	64.4 %	30.1 %	/	5.5 %	/
	treated 3 s	45.9 %	22.1 %	9.1 %	18.0 %	5.0 %
	treated 10 s	44.3 %	18.2 %	12.3 %	20.3 %	4.9 %
	treated 30 s	40.4 %	14.0 %	19.1 %	17.7 %	8.9 %
	treated 60 s	40.4 %	10.6 %	21.5 %	19.3 %	8.3 %

belonging to the C–O ether bond decreased as well. Therefore, not only the carbon atoms from the aromatic rings, but also carbons from the ether part of the PEN are attacked by oxygen atoms from the plasma. The oxidation of these carbon atoms resulted in the formation of C=O, O–C–O, O=C–O and –C(O)–O–C(O)– bonds. We can see that the concentration of these groups increases with the increasing treatment time, especially for the C=O, O–C–O and –C(O)–O–C(O)– groups, while for O=C–O an increase in the concentration is less pronounced, except in first 3 s of the treatment.

The incorporation of new, oxygen functional groups to the PEN surface resulted in an increased surface wettability. As shown in **Table 1**, the water contact angle on the untreated PEN surface was about 90°. Such a surface is hydrophobic with poor wettability. After 10 s of treatment the surface became very hydrophilic with a contact angle of only about 3°. At longer treatment times, the contact angle was so small that it was below the detection limit. In this case, the water drop completely wetted the polymer surface.

Here it is also worth mentioning the plasma treatment of the polymer PET (Polyethylene Terephthalate).[6] This polymer is similar to PEN, but it has only one aromatic ring. In the case of the PET polymer, the wettability of surface after the treatment was lower (less hydrophilic) than for the PEN. Namely, after 10 s of treatment of the PET, the water contact angle decreased from an initial 74° to 15°, while perfect wettability was achieved for treatment times longer than 60 s. The same was also found by Gonzales et al.[9] The concentration of oxygen at the PET surface was a little higher: 39 % and 42 % for 3 s and 60 s of treatment, respectively. The surface oxidation of the polymer PET resulted mostly in the formation of only C=O, O–C–O and O=C–O bonds.[9]

5 CONCLUSIONS

We have shown that by an appropriate treatment of the polymers PEN and PET in plasma it is possible to change the hydrophobic surface to a very hydrophilic one, which was proved by water-contact-angle measurements. For such a modification, usually a few seconds of treatment in a low-pressure oxygen plasma are adequate. Treatment in an oxygen plasma resulted in the incorporation of oxygen atoms from the plasma into the polymer surface, leading to the formation of different chemical bonds between the carbon and oxygen atoms, e.g., C=O, O–C–O, O–C=O and –C(=O)–O–C(=O)–, which are responsible for the observed changes in the surface wettability.

6 REFERENCES

[1] Chan C-M, Ko T-M, Hiraoka H, Surf. Sci. Rep., 24 (**1996**), 1

[2] Meyer-Plath A, Schröder K, Finke B, Ohl A, Vacuum, 71 (**2003**), 391

[3] Gerenser LJ, Surface Chemistry of Plasma-Treated Polymers, in Handbook of Thin Film Process Technology, Ed. D. A Glocker, S. I. Shah, IOP, Bristol, 1996

[4] Strobel M, Lyons CS, Mittal KL, Plasma Surface Modification of Polymers: Relevance to Adhesion, VSP, Utrecht, 1994

[5] U. Cvelbar, M. Mozetič, I. Junkar, A. Vesel, J. Kovač, A. Drenik, T. Vrlinič, N. Hauptman, M. Klanjšek-Gunde, B. Markoli, N. Krstulović, S. Milošević, F. Gaboriau, T. Belmonte. Appl. Surf. Sci., 253 (**2007**), 8669.

[6] Vesel A, Junkar I, Cvelbar U, Mozetič M, Kovač J, Surf. Interface Anal., 40 (**2008**), 1444

[7] Kim MS, Khang G, Lee HB, Prog. Polym. Sci., 33 (**2008**), 138

[8] Grace JM, Zhuang HK, Gerenser LJ, Freeman DR, J. Vac. Sci. Technol., 21 (**2003**), 37

[9] Gonzales II E, Barankin MD, Guschl PC, Hicks RF, Langmuir, 24 (**2008**), 12636

[10] Yuji T, Urayana T, Fujii S, Mangkung N, Akatsuka H, Surf. Coat. Technol., 202 (**2008**), 5289

[11] Beamson G, Briggs D, High Resolution XPS of Organic Polymers – The Scienta ESCA300 Database, Wiley, Chichester, 1992

UDK 666.3:621.762.5:662.613
Professional article/Strokovni članek

ISSN 1580-2949
MTAEC9, 43(6)327(2009)

THE PROPERTIES OF A SINTERED PRODUCT BASED ON ELECTROFILTER ASH

LASTNOSTI SINTRANEGA PRODUKTA IZ ELEKTROFILTRSKEGA PEPELA

Milun Krgović[1], Miloš Knežević[2], Mileta Ivanović[1], Ivana Bošković[1], Mira Vukčević[1], Radomir Zejak[2], Biljana Zlatičanin[1], Snežana Đurković[1]

[1]University of Montenegro, Faculty of Metallurgy and Technology, 20000Podgorica, Montenegro
[2]University of Montenegro, Faculty of Civil Engineering, Džordža Vašingtona bb, 20000 Podgorica, Montenegro
milun@cg.ac.yu

Prejem rokopisa – received: 2009-03-30; sprejem za objavo – accepted for publication: 2009-06-24

The aim of this investigation was to obtain a sintered product based on electrofilter ash as a component of the raw-material mixture with satisfactory characteristics with regard to linear and volume shrinkage, total porosity and compression strength. The second component of the raw-material mixture is illite-kaolinite clay. The product obtained by sintering this raw-material mixture, based on its mechanical properties and total porosity, can be employed as a useful building material. On the basis of the obtained results the optimum sintering regime will be defined, taking into account the economic character of the process.

Keywords: electrofilter ash, clay, linear shrinkage, total shrinkage, sintering, porosity

Cilj raziskave je bil pridobiti sintran produkt z elektrofiltrskim pepelom kot komponento zmesi surovin in z zadovoljivimi linearnimi ter volumenskim skrčkom, skupno poroznostjo in tlačno trdnostjo. Druga komponenta surove zmesi je bila illitno-kaolinitna glina. Produkt sintranja te zmesi je zaradi mehanskih lastnosti in skupne poroznosti primeren za uporabo kot gradbeni material. Na podlagi rezultatov te raziskave bo opredeljen optimalen režim sintranja z upoštevanjem ekonomike procesa.

Ključne besede: elektrofiltrski pepel, glina, linearni skrček, skupni skrček

1 INTRODUCTION

Electrofilter ash contains silicates, carbonates and phosphates of calcium, magnesium, iron, aluminium and other elements[1]. Illite-kaolinite clays, apart from illite and kaolinite minerals, also contain a-quartz, Fe_2O_3 and $CaCO_3$[2]. This composition of the components from the raw-material mixture qualifies, depending on the sintering temperature, the reactions in the solid state, the polymorphic transformations of quartz and the liquid-phase formation[3]. Apart from the ceramic mass-sintering rate, i.e., the firing regime, the mineral content of the raw materials has an important role in the relations between particular microstructural elements[4]. The liquid phase accelerates the solid-state reactions (the diffusion coefficient in such systems increases by 1000 times)[5]. The new crystal phases, i.e., the compounds formed as a crystal phase during the sintering process, apart from the above-mentioned factors, were determined by the mineral and chemical content of the clay[6,7]. During the sintering of the samples with electrofilter ash, as a component of the raw-material mixture, the process is based on the heating of the samples at a temperature sufficient for the oxidation of the free carbon present in the ash, which could cause surface defects and a decrease of the sintered product's strength. In the following phase the samples are heated to the sintering temperature to obtain products with satisfactory characteristics with regard to the porosity and strength[8]. The content of electrofilter ash in the raw-material mixture can be 20–70 %[9], depending on the shaping method, the sintering temperature and the flux addition.

2 EXPERIMENTAL

The raw-material mixture for the production of samples was formed on the basis of "Pljevlja" clay as a binder, with five different mass fractions of electrofilter ash (10, 20, 30, 40 and 50 %). The samples were formed by plastic shaping in a mould corresponding to a parallelepiped with the dimensions 7.7 cm × 3.9 cm × 1.6 cm. For the components of the raw-material mixture the mineral and chemical composition, and the grain size distribution with granulometric analysis, were determined. The density and humidity of the components of the raw-material mixture were also determined. For the raw, unfired products, the linear and volume shrinkage during drying in air to a constant mass and drying in a dryer at a temperature of 110 °C were determined. The sintering of the samples with different amounts of electrofilter ash (Thermal plant "Pljevlja") was performed at a temperature of 1100 °C. This temperature was chosen on the basis of previous investigations of the temperature's influence on the properties of the sintered products on the basis of the composition of the raw-material mixture.

For the sintered products with different amounts of electrofilter ash we determined:
- the total porosity,
- the linear and volume shrinkage during sintering,
- the compression strength,
- the microscopic and X-ray analysis of the sintered products.

3 RESULTS AND DISCUSSION

The mineral content of "Pljevlja" clay (**Figure 1**) determined by X-ray analyses shows that the clay is an illite-kaolinite type, with the presence of quartz, muscovite, calcite and clinochlor. The X-ray analysis of electrofilter ash (**Figure 2**) shows the presence of quartz, rankinite and albite. The DTA analysis of the "Pljevlja" clay does not indicate any particularly endothermic and exothermic "peaks"; therefore, TG analyses (**Figure 3**) and DTG (**Figure 4**) analyses were performed. On the curved line of the DTG (the rate of mass change during sample heating) some changes, i.e., peaks, at a temperature of 529 °C were noticed, which probably correspond to the dissolution of the illite and kaolinite, as well as peaks at a temperature of 731 °C (carbonate dissolution). The DTA analysis of the electrofilter ash (**Figure 5**) does not show any precisely defined peaks that correspond to endothermic and exothermic reactions. The changes in the heating were registered in the form of slight inflections, where the first one was registered in the temperature range (305–520) °C ($MgCO_3$), and the second with an endothermic effect at a temperature of 728 °C, as a consequence of CO_2 formation with the thermal dissociation of $CaCO_3$. The most significant mass change, according to the results of the TG analysis (**Figure 5**), was registered in the interval from 654.9 °C to 827.3 °C, which corresponds to the thermal dissociation of $CaCO_3$, according to the results of the X-ray analysis. The mass loss for this temperature interval was 3.78 %.

The granulometric analysis (**Table 1**, **Table 2**,) shows that the electrofilter ash has a greater average grain size (109 μm) than clay (21.90 μm). For the electrofilter ash the most common fractions are: from 99 μm to 114 μm (13.7 %); from 114 μm to 131 μm (14.3 %); and from 131 μm to 150 μm (12.4 %). For the "Pljevlja" clay the most common fractions are: from 57.2 μm to 65.7 μm (4.6 %); from 65.7 μm to 75.4 μm (4.7 %); and from 75.4 μm to 150 μm (4.4 %).

The results of the chemical analysis of the "Pljevlja" clay and the electrofilter ash (**Table 3** and **Table 4**) show a larger mass fractions of Al_2O_3 in the electrofilter ash (21.77 %) than in the clay (10.55 %). The amount of SiO_2 is lower in the electrofilter ash (49.45 %) than in the clay (71 %). The "Pljevlja" clay does not contain the

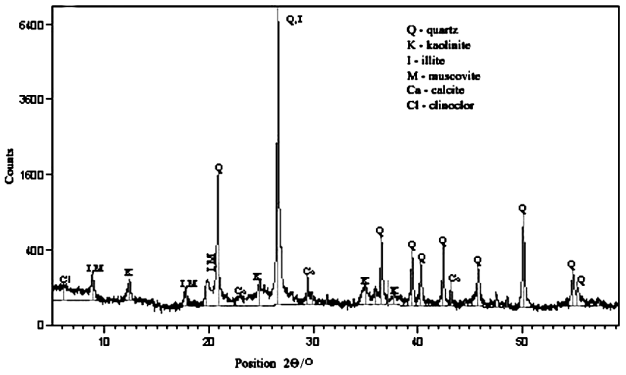

Figure 1: X-ray diffractogram of "Pljevlja" clay
Slika 1: X-difraktogram gline Pljevlja

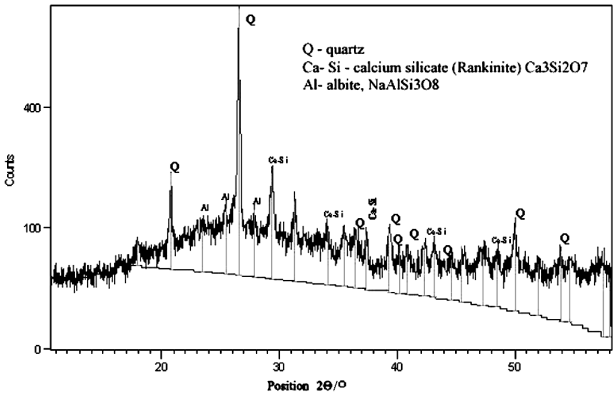

Figure 2: X-ray diffractogram of electrofilter ash from TE "Pljevlja"
Slika 2: X-difraktogram elektrofiltrskega pepela iz TE Pljevlja

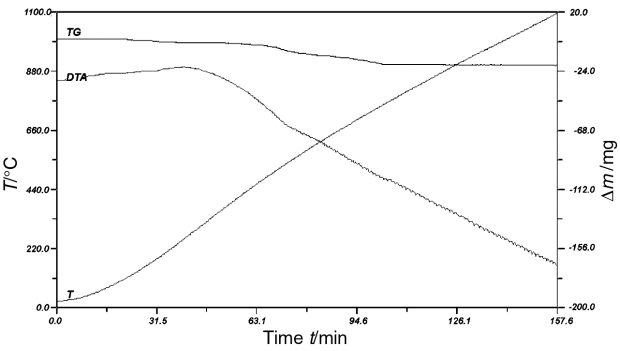

Figure 3: DTA and TG analysis of clay sample
Slika 3: DTA- in TG-analiza vzorca gline

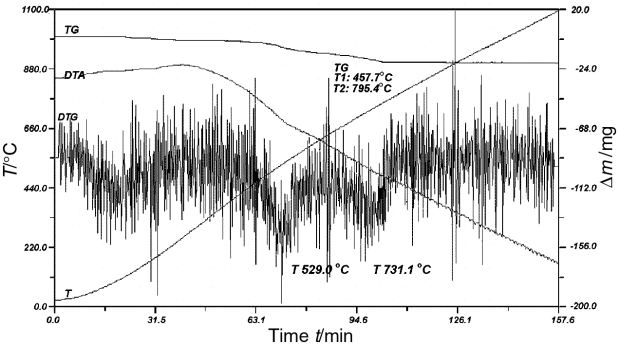

Figure 4: DTA, TG and DTG analysis of clay sample
Slika 4: DTA-, TG- in DTG-analiza vzorca gline

Table 1: Particle size distribution of clay
Tabela 1: Velikostna porazdelitev zrn gline

Particle size (μm)	<2	<5	<20	<30	>45	>60	<80	<100	<150
Percentage (%)	9.80	25.90	48.10	56.70	33.00	24.20	14.60	8.20	1.90

Table 2: Particle size distribution of electrofilter ash
Tabela 2: Velikostna porazdelitev zrn elektrofiltrskega pepela

Particle size (μm)	<2	<5	<20	<30	>45	>60	<80	<100	<150
Percentage (%)	1.50	1.90	5.00	7.60	88.30	80.90	73.40	58.10	18.50

Table 3: Chemical composition of clay
Tabela 3: Kemična sestava gline

Oxides	SiO_2	Fe_2O_3	Al_2O_3	CaO	MgO	Na_2O	K_2O	SO_3	lg.loss
w/%	71	5.51	10.55	1.42	0.62	0.45	1.86	0.25	8.34

Table 4: Chemical composition of electrofilter ash
Tabela 4: Kemična sestava elektrofiltrskega pepela

Oxides	SiO_2	Fe_2O_3	Al_2O_3	TiO_2	CaO	Na_2O	ZnO	MgO	MnO	P_2O_5	K_2O	lg.loss
w/%	49.45	5.23	21.77	0.66	13.34	0.46	0.004	1.29	0.02	0.24	1.40	4.35

following oxides, present in electrofilter ash: MnO, TiO_2, ZnO and P_2O_5.

The granulometric content of the components of the raw-material mixture has an important influence on the volume and linear shrinkage of the product during sintering. The values of the volume shrinkage during sintering decrease with the increase in the amount of ash in the raw-material mixture (**Figure 6**). With the increase in the amount of electrofilter ash the linear and volume shrinkage decreases. In the components of the raw-material mixture there is no significant difference in the amount of Fe_2O_3, but the amount of MgO in the ash is twice as high, and therefore the increase in the amount of ash in the raw-material mixture can cause a reaction between Mg (II) oxide and Fe (III) oxide, and an increase of the influence on the porosity as well as the extension of the system. The particles of soot present in electrofilter ash have an important influence on the linear and volume shrinkage. During sintering the carbon present is oxidized, defects are formed and the strength of the samples is reduced. Electrofilter ash contains TiO_2 and MnO, which have the role of mineralizers and affect the polymorphic transformations of the quartz. The activity of the TiO_2 is influenced by its content (0.66 %) and the sintering temperature.

The total porosity during sintering increases with the increase of ash content in the raw-material mixture (**Figure 7**). The mineral and granulometric content of the components of the raw-material mixture, as well as the shaping method, have an important influence on the porosity. A higher mean value of the grain of electrofilter ash with relation to the clay causes an increase in the porosity of the raw, unfired product, and therefore an increase in the porosity of the sintered product. During the formation of the raw-material mixture the flux was not added, but the content of alkalis in the clay is higher than in the electrofilter ash (chemical analysis), which causes a reduction in the amount of liquid phase with the in-

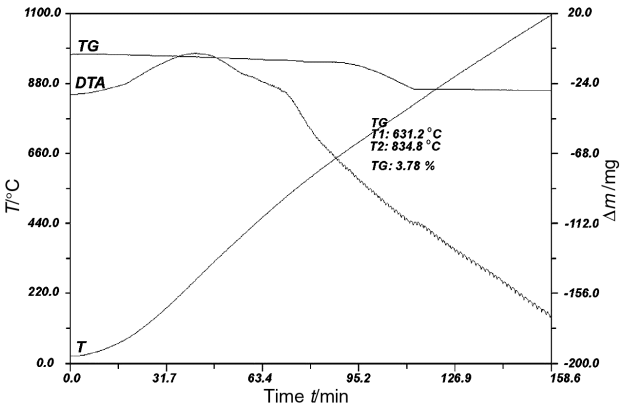

Figure 5: DTA and TG analysis of electrofilter ash sample
Slika 5: DTA in TG analiza vzorca elektrofiltrskega pepela

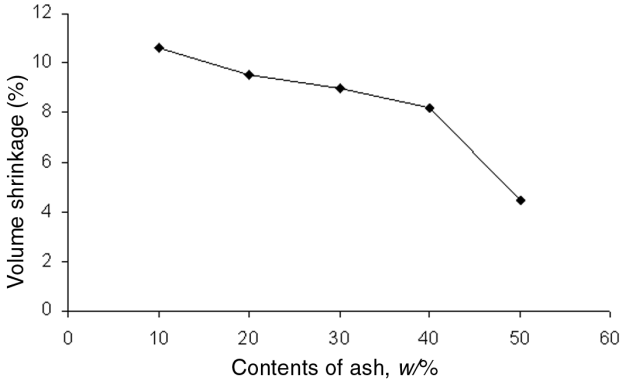

Figure 6: Volume shrinkage of product during sintering on T = 1100 °C, (ash content in mass fractions *w*/% = (10, 20, 30, 40 and 50)
Slika 6: Volumenski skrček zmesi pri sintranju pri T = 1100 °C (vsebnost pepela v masnih deležih *w*/% = (10, 20, 30, 40 in 50)

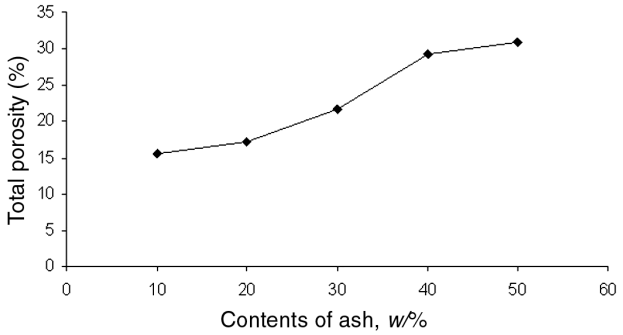

Figure 7: Total porosity of products during sintering at T = 1100 °C, (ash content in mass fractions w/% = (10, 20, 30, 40 and 50)
Slika 7: Skupna poroznost zmesi pri sintranju pri T = 1100 °C (vsebnost pepela v masnih deležih w/% = (10, 20, 30, 40 in 50)

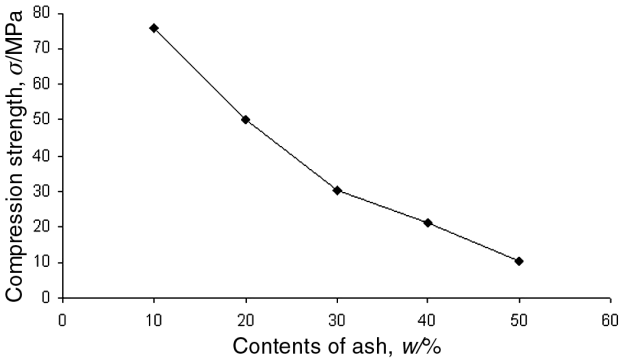

Figure 8: Compression strength of product during sintering at T = 1100 °C, (ash content in mass fractions w/% = (10, 20, 30, 40 and 50)
Slika 8: Tlačna trdnost po sintranju pri T = 1100 °C (vsebnost pepela v masnih deležih w/% = (10, 20, 30, 40 in 50)

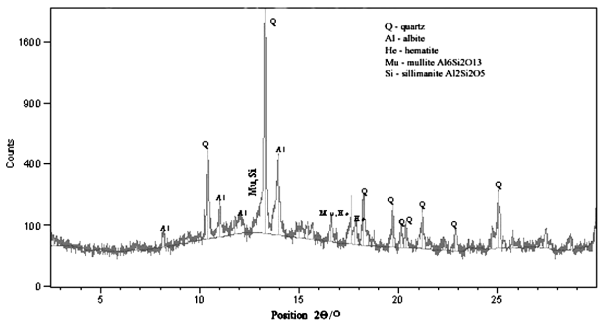

Figure 9: X-ray diffractogram of sintered product (ash 40 %, clay 60 %, T = 1100 °C)
Slika 9: X-difraktogram sintranega proizvoda (T = 1100 °C, masni delež pepela 40 %, gline 60 %)

crease in the amount of ash. The liquid phase accelerates the reactions in the solid state as a result of the increase in the diffusion coefficient.

The compression-strength value decreases with the increase in the amount of ash in the raw-material mixture (**Figure 8**). With the increase in the amount of ash the total porosity is increased, which decreases the compression-strength values. The amount of mullite and sillimanite in the sintered product decreases with the increase in the content of ash (X-ray analysis of the sintered product), which has an important influence on the mechanical characteristics of the sintered product. The X-ray diffractogram of the sintered product (40 % of ash; 60 % of clay) shows the presence of quartz, albite, hematite, mullite and sillimanite (**Figure 9**). Mullite is formed at temperatures from 900 °C to 1100 °C. The presence of TiO_2 in the electrofilter ash (0.66 %) can partly enhance the mullitization, while the presence of a small amount of MnO (0.022 %) probably has a minor effect as a mineralizer in the polymorphic transformations of quartz. The microstructure of the sintered products (**Figure 10** and **Figure 11**) shows that it is a very complex structure: crystal phase (mullite, sillimanite, quartz) with the presence of the glass phase and pores.

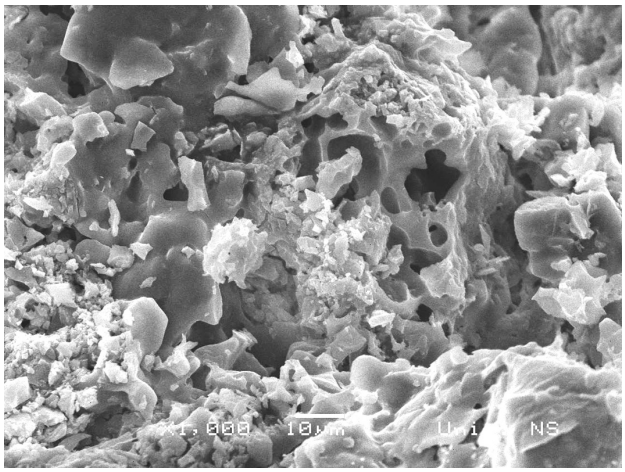

Figure 10: Microstructure of sintered product (T = 1100 °C, ash 40 %, clay 60 %, enlarged 1000-times)
Slika 10: Mikrostruktura sintranega produkta (T = 1100 °C, masni delež pepela 40 %, gline 60 %) pov. 1000-kratna

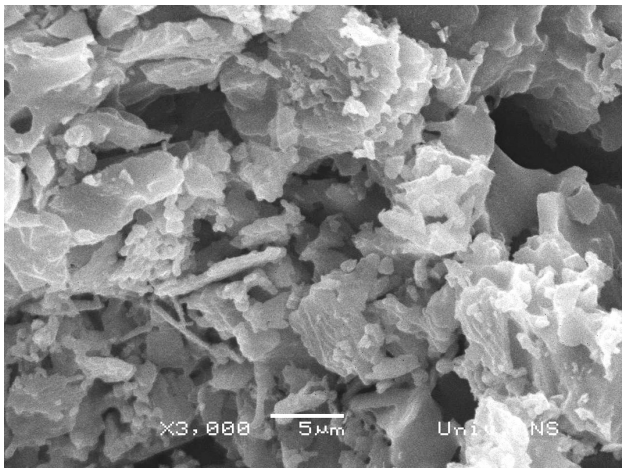

Figure 11: Microstructure of sintered product (T = 1100 °C, ash 40 %, clay 60 %, enlarged 3000-times)
Slika 11: Mikrostruktura sintranega produkta (T = 1100 °C, masni delež pepela 40 %, gline 60 %), pov. 3000-kratna

4 CONCLUSION

The investigations of the properties on the basis of the raw-material mixture of electrofilter ash and clay show that:

- on the basis of this raw-material mixture satisfactory characteristics of the sintered product with regard to volume shrinkage, total porosity and compression strength are obtained;
- without the presence of flux, a component for the reduction of shrinkage and electrolytes in the raw-material mixture, the mass fraction of electrofilter ash should not be higher than 30 %;
- investigations were performed without the pulverization of electrofilter ash, which would definitely have an influence on the properties of the sintered product.

5 REFERENCES

[1] Lj. Kostić-Gvozdenović, R. Ninković, *Inorganic technology*, Faculty of Technology and Metallurgy, University of Belgrade, Belgrade (1997)

[2] M. Krgović, M. Ivanović, N. Z. Blagojević, Ž. Jaćimović, R. Zejak, M. Knežević, *Interceram,* 55 (**2006**) 2, 104–106

[3] M. Tecilazić-Stevanović, *Principles of ceramic technology*, Faculty of Technology and Metallurgy, University of Belgrade, Belgrade (1990)

[4] J. Griffiths, *Ind. Min*., 272 (**1990**), 35–40

[5] M. M. Krgović, Z. K. Jaćimović, R. Zejak, *Tile & Brick Int*., 17 (**2001**) 3, 178–181

[6] B. Živanović, R. Vasić, O. Janjić, *Ceramic tiles,* Monograph in the Institute of Materials in Serbia, Belgrade, (1985)

[7] A. Mishulovich, J. L. Evanko, Ceramic tiles from high-carbon fly ash, International Ash Symposium, Center for Applied Energy Research, University of Kentucky, (2003)

[8] Tütünlü Ftih, Atalay Ümit, Utilization of fly ash in manufacturing of building bricks, International Ash Symposium, Center for Applied Energy Research, University of Kentucky, (2001)

[9] R. H. Carty, Utilization of Illinois fly ash in manufacturing of ceramic tiles, Final technical report, ICCI, November, (1999)

MATERIALI IN TEHNOLOGIJE

MATERIALS AND TECHNOLOGY

Letnik / Volume 43 2009

ISSN 1580-2949

IMT Ljubljana, Lepi pot 11, 1000 Ljubljana, Slovenija

MATERIALI IN TEHNOLOGIJE / MATERIALS AND TECHNOLOGY

VSEBINA / CONTENTS
LETNIK / VOLUME 43, 2009/1, 2, 3, 4, 5, 6

MATERIALI IN TEHNOLOGIJE / MATERIALS AND TECHNOLOGY

AVTORSKO KAZALO / AUTHOR INDEX

LETNIK / VOLUME 43, 2009, 1–6, A–Ž

MATERIALI IN TEHNOLOGIJE / MATERIALS AND TECHNOLOGY

VSEBINSKO KAZALO / SUBJECT INDEX

LETNIK / VOLUME 43, 2009, 1–6

Kovinski materiali – Metallic materials

Varovanje okolja – Environmental protection